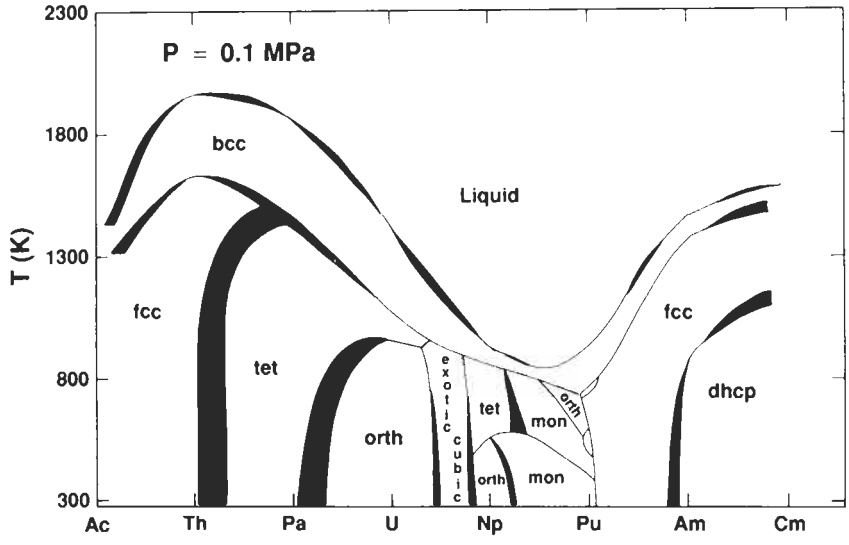

Fig. 37. Combined binary alloy phase diagrams for the light actinides (from YOUNG [1991]).

Acknowledgements

The author would like to express his sincere gratitude to Mss. M. Krichel for the preparation of the structure plots.

References

AHUJA, R., J.M. WILLS, B. JOHANSSON and O. ERIKSSON, 1993, Phys. Rev. **B48**, 16269–79.

BORCHARDT-OTT, W., 1993, Kristallographie (Springer Verlag, Berlin).

BRUNNER, G.O., and D. SCHWARZENBACH, 1971, Z. Kristallogr. **133**, 127–133.

DAAMS, J.L.C., P. VILLARS and J.H.N. VAN VUCHT, 1991, Atlas of Crystal Structure Types for Intermetallic Phases (American Society for Metals, USA), Vols. 1 to 4.

DAAMS, J.L.C., J.H.N. VAN VUCHT and P. VILLARS, 1992, J. Alloys and Compounds **182**, 1–33.

DABOS-SEIGNON, S., J.P. DANCAUSSE, E. GERING, S. HEATHMAN and U. BENEDICT, 1993, J.Alloys and Compounds **190**, 237–242.

DONOHUE, J., 1974, The structures of the elements (John Wiley & Sons, New York).

EK, J. VAN, P.A. STERNE and A. GONIS, 1993, Phys. Rev. **B48**, 16280–9.

HAHN, T. (ed.), 1992, International Tables for Crystallography, Vol. A (Kluwer Academic Publishers, Dordrecht).

KOCH, E. and W. FISCHER, 1992, Sphere packings and packings of ellipsoids. In: International Tables for Crystallography, ed. by A.J.C.Wilson (Kluwer Academic Publishers, Dordrecht).

LEIGH, G.J. (ed.), 1990, Nomenclature of Inorganic Chemistry. Recommendations 1990 (Blackwell Scientific Publications, Oxford).

MASSALSKI, T.B., 1990, Binary Alloy Phase Diagrams, Vols. 1–3, (ASM International, USA).

PEARSON, W. B., 1972, The Crystal Chemistry and Physics of Metals and Alloys (Wiley-Interscience, New-York).
SCHULTE, O., and W. B. HOLZAPFEL, 1993, Phys.Rev. **B48,** 14009–12.
SKRIVER, H. L., 1985, Phys.Rev. **B31,** 1909–23.
VAINSHTEIN, B. K., V. M. FRIDKIN and V. L. INDENBOM, 1982, Modern Crystallography II: Structure of Crystals (Springer-Verlag, Berlin).
VILLARS, P. and L. D. CALVERT, 1991, Pearson's Handbook of Crystallographic Data for Intermetallic Phases (American Society for Metals, USA), Vols. 1 to 4.
YOUNG, D. A., 1991, Phase Diagrams of the Elements (University of California Press, Berkeley).

Further reading

BARRETT, C. S., and T. B. MASSALSKI, 1980, Structure of Metals, 3rd edition (Pergamon Press, Oxford).
BOER, F. R. DE, R. BOOM, W. C. M. MATTENS, A. R. MIEDEMA and A. K. NIESSEN, 1988, Cohesion in Metals (North-Holland, Amsterdam).
HAFNER, J., F. HULLIGER, W. B. JENSEN, J. A. MAJEWSKI, K. MATHIS, P. VILLARS and P. VOGL, 1989, The Structure of Binary Compounds. (North-Holland, Amsterdam).
PETTIFOR, D. G., 1993, Electron Theory of Crystal Structure, in: Structure of Solids, ed. V. Gerold, Volume 1 of *Materials Science and Technology* (VCH, Weinheim).
VAINSHTEIN, B. K., 1994, Modern Crystallography I: Fundamentals of Crystals (Springer-Verlag, Berlin).

CHAPTER 2

ELECTRON THEORY OF METALS

D. G. PETTIFOR

Department of Materials
University of Oxford
Oxford, UK

R. W. Cahn and P. Haasen†, eds.
Physical Metallurgy; fourth, revised and enhanced edition

1. Introduction

The bulk properties of a metal depend directly on the bonding between the constituent atoms at the *microscopic* level. Thus, in order to provide a fundamental description of metals and alloys, it is necessary to understand the behaviour of the valence electrons which bind the atoms together. The theory which describes the electrons in metals is couched, however, in a conceptual framework that is very different from our everyday experience, since the microscopic world of electrons is governed by *quantum* mechanics rather than the more familiar *classical* mechanics of Newton. Rather than solving Newton's laws of motion the solid state theorist solves the Schrödinger equation,

$$\left(-\frac{\hbar^2}{2m}\nabla^2 + v(\boldsymbol{r})\right)\psi(\boldsymbol{r}) = E\psi(\boldsymbol{r}), \tag{1}$$

where $\nabla^2 = \partial^2/\partial x^2 + \partial^2/\partial y^2 + \partial^2/\partial z^2$, m is the electronic mass and $\hbar$ is the ubiquitous Planck constant (divided by 2π). $-(\hbar^2/2m)\,\nabla^2$ represents the *kinetic* energy and $v(\boldsymbol{r})$ the *potential* felt by the electron which has *total* energy E. $\psi(\boldsymbol{r})$ is the wave function of the electron where $|\psi(\boldsymbol{r})|^2$ is the probability density of finding the electron at some point $\boldsymbol{r} = (x, y, z)$. The power of the Schrödinger equation is illustrated by solving eq. (1) for the case of a single hydrogenic atom. It is found that solutions exist only if the wave function ψ is characterized by three distinct quantum numbers n, l and m whose significance has been discussed at the beginning of the preceding chapter. A fourth quantum number, m_s, representing the spin of the electron results from a relativistic extension of the Schrödinger equation. Thus, the existence of different orbital shells and hence the chemistry of the Periodic Table follows naturally from quantum mechanics through the Schrödinger equation.

WIGNER and SEITZ [1933] were the first to apply the Schrödinger equation to the problem of bonding in metals. In their classic paper they studied the formation of the bond in *monovalent* sodium and obtained the cohesive energy, equilibrium lattice constant, and bulk modulus to within 10% of the experimental values. However, it took nearly another fifty years before the same accuracy was achieved for the *polyvalent* metals. Whereas WIGNER and SEITZ [1933] could assume that the single valence electron on a sodium atom feels only the potential due to the ion core, in a polyvalent metal a given electron will also feel the strong coulomb repulsion from other valence electrons in its vicinity. Thus the problem becomes much more complex. Firstly, the potential $v(\boldsymbol{r})$ must be computed *self-consistently* in that $v(\boldsymbol{r})$ now depends on the coulomb field of valence electrons whose wave functions and hence average charge distributions themselves depend on $v(\boldsymbol{r})$ through eq. (1). Secondly, it is necessary in order to obtain bonding to go beyond the *average* self-consistent field of the Hartree approximation and to include the correlations between the electrons. Pauli's exclusion principle keeps *parallel* spin electrons apart, thereby lessening their mutual coulomb repulsion and lowering the energy by an amount called the *exchange* energy. These *statistical* correlations are described by the Hartree-Fock approximation. In addition, *dynamical* correlations also exist between the anti-parallel spin electrons, which lower the energy of the

system by an amount called the *correlation* energy.

A major breakthrough in solid-state physics occurred with the realization that these very complicated exchange and correlation effects could be accurately modeled by adding a simple local exchange correlation potential $v_{xc}(r)$ to the usual Hartree coulomb potential

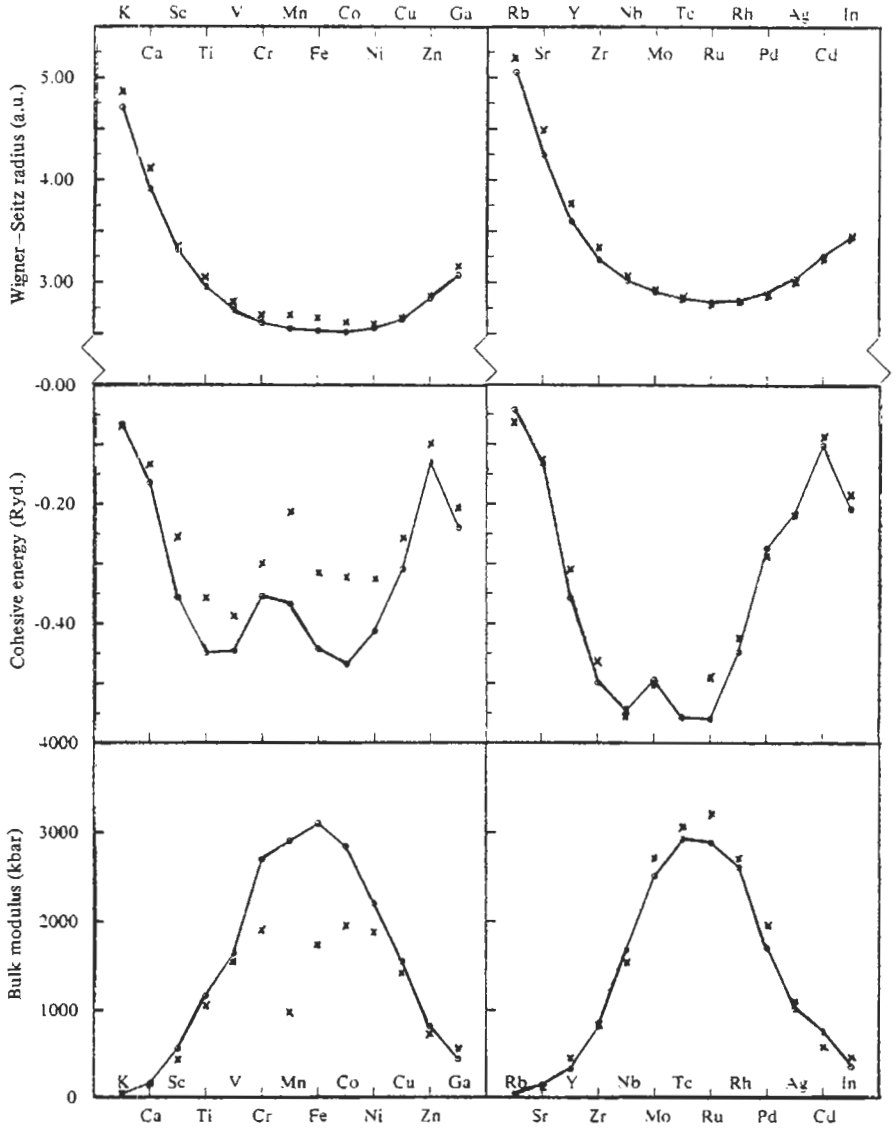

Fig. 1. The equilibrium Wigner–Seitz radii, cohesive energies, and bulk moduli of the 3d and 4d transition series. Experimental values are indicated by crosses and the computed LDF values by the connected points. (From MORUZZI *et al.* [1978].)

References: p. 129.

in eq. (1). The resulting so-called *local density functional* (LDF) equations (HOHENBERG and KOHN [1964] and KOHN and SHAM [1965]) have been shown to yield a surprisingly good description of the energetics of atoms, molecules, and solids (GUNNARSSON and LUNDQUIST [1976], HARRIS and JONES [1978], MORUZZI *et al.* [1978], JONES and GUNNARSSON [1989] and FINNIS [1992]). The success of the LDF scheme is illustrated in fig. 1 by the results of MORUZZI *et al.* [1978] for the cohesive properties of the elemental metals across the 3d and 4d transition series. We see that for the nonmagnetic 4d series the equilibrium Wigner–Seitz radius (or lattice constant), cohesive energy and bulk modulus are given to better than 10%. The large deviations in lattice constant and bulk modulus observed amongst the 3d series is due to the presence of magnetism and is removed by generalizing the LDF theory to include spin polarization (JANAK and WILLIAMS [1976]). It must be stressed that there are no arbitrary parameters in the theory, the only input being the nuclear charge and crystal structure.

This success of the LDF theory in describing the bonding between atoms allows the interpretation of the results within a *band* framework, since the motion of a given electron is governed by the *one-electron* Schrödinger equation (1). As is well-known, the energy levels, E, of the free atom broaden out into bands of states as the atoms are brought together to form the solid. In this chapter the nature of these energy bands in simple metals, transition metals and binary alloys is discussed, thereby unraveling the microscopic origin of the attractive and repulsive forces in the metallic bond. In § 2.1 we begin with a detailed description of the constituent atoms, since we will see that many bulk properties are related to the relative position of the atomic energy levels and to the size of the ionic cores. In § 2.2 the diatomic molecule is used to illustrate *bond* formation and in § 2.3 the general principle of *band* formation in solids is outlined. The nature of *simple-* and *transition*-metal bands is then discussed in §§ 3 and 4 respectively, the former being treated within the nearly-free-electron approximation, the latter within the tight-binding approximation. In § 5 the knowledge of the energy band behaviour is used to provide a microscopic picture of metallic bonding which is responsible for the cohesive properties of the elemental metals displayed in fig. 1. In § 6 *structural* stability is discussed both in the elemental metals and in binary intermetallic phases. In § 7 the ideas on metallic bonding are extended to a discussion of the *heats of formation*, ΔH, of binary alloys. Finally in § 8 the band theory of *magnetism* is presented which accounts for the antiferromagnetism of Cr and Mn and the ferromagnetism of Fe, Co, and Ni amongst the 3d transition metals.

2. *Band formation*

2.1. The constituent atoms

The hundred basic building blocks of nature, which are enshrined in the Periodic Table, lead to matter having a wide range and variety of physical properties. This diversity reflects the essential uniqueness of each element in the Periodic Table. For example, even though copper, silver and gold lie in the same noble-metal group, nobody except possibly a theoretician would be prepared to regard them as identical. In this

subsection the differences between the elements are *quantified* by discussing the behaviour of the atomic energy levels and the radii throughout the Periodic Table.

The structure of the Periodic Table results from the filling-up of different orbital shells with electrons, as outlined in the previous chapter. The chemical behaviour of a given atom is governed by both the *number* and the *angular-momentum* character of the electrons in the outer partially filled shells. (We shall refer to these electrons as *valence* in contrast to the filled shells of *core* electrons.) The angular-momentum character is determined by the orbital quantum number l, since the *magnitude* of the total orbital angular momentum $\boldsymbol{L}$ is given by quantum theory as:

$$L = \hbar\sqrt{l(l+1)}, \tag{2}$$

where l = 0, 1, 2,... A free-atom electron can, therefore, take only *discrete* values of angular momentum (i.e. 0, $\hbar\sqrt{2}$, $\hbar\sqrt{6}$,...) unlike a classical particle which would have a *continuous* spectrum. However, as in the classical case, the angular momentum is *conserved* because the electron is moving in the central spherically symmetric potential of the free atom. Electrons with l = 0, 1, 2 and 3 orbital quantum numbers are referred to as s, p, d and f electrons, respectively (after the old terminology of sharp, principal, diffuse and fine spectroscopic lines).

Angular momentum is a vector. Therefore, in addition to the *magnitude* L of the orbital angular momentum $\boldsymbol{L}$, the electronic state is also characterized by the *components* of the angular momentum. Within quantum theory the component in a given direction (say along the z-axis, specified experimentally by the direction of a very weak applied magnetic field) is quantized and given by

$$L_z = m\hbar, \tag{3}$$

where the magnetic quantum number, m, takes the $(2l+1)$ values 0, ± 1,..., ± $(l-1)$, ± l. Because the *energy* of the electron can not depend on the direction of the angular momentum in a spherically symmetric potential, these $(2l+1)$ states have the same energy and are said to be *degenerate*. Allowing for the additional *spin* quantum number, m^s, which can take two values (corresponding to an up, ↑, or down, ↓, spin electron), each l-state will be $2(2l+1)$-fold degenerate. Thus an s-shell can hold 2 electrons, a p-shell 6 electrons, a d-shell 10 electrons and an f-shell 14 electrons as discussed in ch. 2, § 1.

The state of angular momentum of the electron determines the *angular dependence* of the wave function ψ and hence the angular dependence of the probability-density $|\psi|^2$. The s-state has zero orbital angular momentum corresponding to a spherically symmetric probability density which is illustrated schematically in fig. 2a. The p-state, corresponding to $l=1$, $m=0$, has an angular variation given by $\cos\theta$, where θ is the polar angle. Because the Cartesian coordinates (x, y, z) can be related to the spherical polar coordinates (r, θ, ϕ), and in particular $z = r\cos\theta$, it is customary to refer to the $l=1$, $m=0$ state as the p_z *orbital*. Its probability-cloud is illustrated by the left-hand diagram in fig. 2b. We see that it has lobes pointing out along the z-axis, in which direction there is a maximum probability of finding the electron ($\cos^2\theta = 1$ for $\theta = 0, \pi$). On the other

hand, there is zero probability of finding the electron in the x–y plane ($\cos^2\theta = 0$ for $\theta = \pi/2$). Since we often deal with atoms in a *cubic* environment in which all three Cartesian axes are equivalent (e.g., fcc or bcc crystals), we form the p_x and p_y orbitals by taking linear combinations of the two remaining states corresponding to $m = +1$. They are illustrated in fig. 2b. The probability clouds of the five d orbitals corresponding to $l = 2$ are shown in fig. 2c. We might expect from fig. 2 that the nature of the bonding between atoms will be very dependent on the angular momentum character of the atomic valence electrons. This will be discussed in § 2.2.

Historically it was the discrete lines of the atomic spectra and their ordering according to Balmer's formula that led Bohr to postulate his famous model of the hydrogen atom from which he deduced that the *energy* levels were given by

$$E_n = -\left(me^4 / 32\pi^2\varepsilon_0^2\hbar^2\right) / n^2, \tag{4}$$

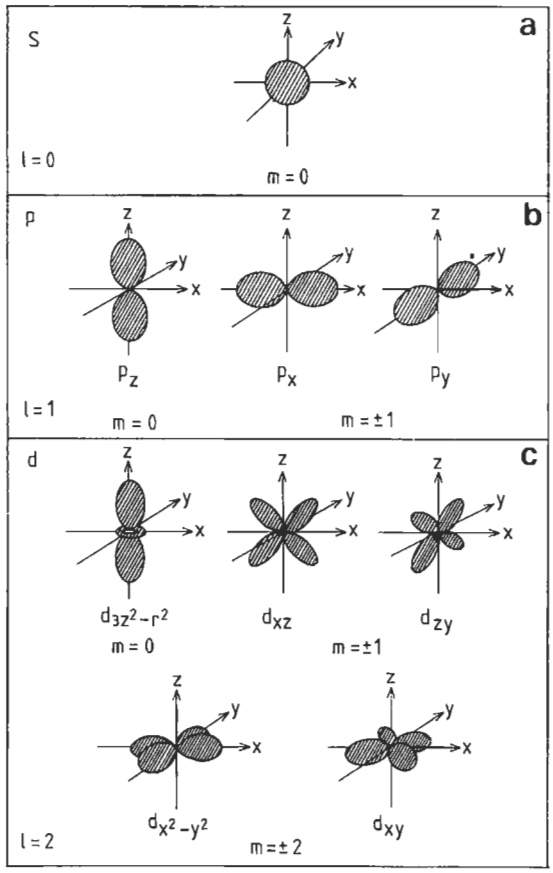

Fig. 2. The probability clouds corresponding to s, p and d orbitals are shown in (a), (b) and (c), respectively.

where e is the magnitude of the electronic charge, ε_0 is the permittivity of free space, and n is a positive integer. The corresponding radii of the so-called stationary orbits were given by

$$a_n = \left(4\pi\varepsilon_0\hbar^2 / me^2\right)n^2. \tag{5}$$

Substituting into eqs. (4) and (5) the SI values $m = 9.1096 \times 10^{-31}$ kg, $e = 1.6022 \times 10^{-19}$ C, $4\pi\varepsilon_0 c^2 = 10^7$, $c = 2.9979 \times 10^8$ m/s and $\hbar = 1.0546 \times 10^{-34}$ Js, we have:

$$E_n = 2.1799 \times 10^{-18} / n^2 \quad \text{J} \tag{6}$$

and

$$a_n = n^2 \text{ au}. \tag{7}$$

The *ground state* of the hydrogen atom, which corresponds to $n = 1$, has an energy, therefore, of 2.18×10^{-18} J and an orbital Bohr radius of 0.529×10^{-10} m or 0.529 Å. Because of the small magnitude of the energy in SI units, it is customary for solid-state physicists to work in *atomic units,* where the unit of energy is the Rydberg (Ry) and the unit of length is the atomic unit (au). The former is the ground-state energy of the hydrogen atom, the latter is the first Bohr radius. Thus, in atomic units we have

$$E_n = -n^{-2} \text{ Ry} \tag{8}$$

and

$$a_n = n^2 \text{ au}. \tag{9}$$

It follows from eqs. (4), (5), (8) and (9) that $\hbar^2/2m = 1$ in atomic units. Another frequently used unit is the electron-Volt, where 1 Ry = 13.6 eV. In this chapter *electronic* energy levels, *E,* will be given in either eV or Ry, whereas *total* energies will be given in either eV/atom or Ry/atom. Conversion to other units may be achieved by using 1 mRy/atom = 0.314 kcal/mole = 1.32 kJ/mole. Length scales will be given either in au or in Å, where 1 au = 0.529 Å.

Solution of the Schrödinger equation (1) for the hydrogen atom leads directly to Bohr's expression (4) for the energy levels, E_n, where n is identified as the *principal* quantum number. For the particular case of the hydrogen atom where the potential $v(r)$ varies inversely with distance r from the nucleus, the energy levels do not depend on the angular-momentum quantum numbers l and m. Figure 3 shows the energy levels of atomic *hydrogen* given by eq. (8), where use has been made of the quantum-theory result that for a given n the orbital quantum number l must be such that $0 \leq l \leq (n-1)$. The total degeneracy of each orbital including spin, namely $2(2l+1)$, is given at the bottom of the figure and accounts for the structure of the Periodic Table, discussed in the previous chapter. In practice, the energy-level diagram of elements other than hydrogen is different from fig. 3, because the presence of more than one electron outside the nucleus leads to the potential $v(r)$ no longer showing a simple inverse distance behaviour, so that states with the same principal quantum number n but different orbital quantum

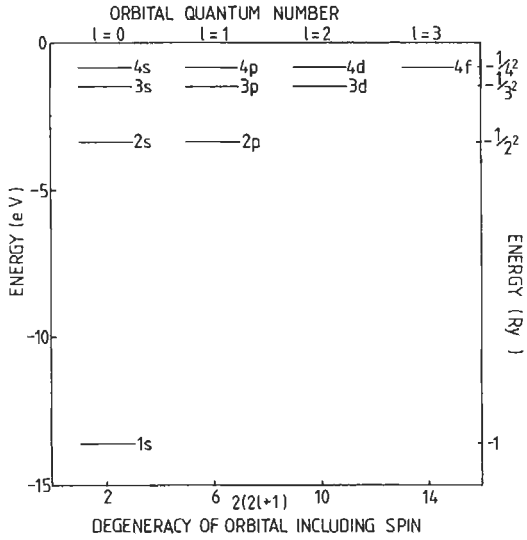

Fig. 3. The energy levels of atomic hydrogen.

numbers l have their degeneracy lifted. This is illustrated in fig. 4, where it is clear, for example, that the 2s level of the second-row elements B to Ne lies well below that of the corresponding 2p level. These atomic energy levels were taken from the tables compiled by HERMAN and SKILLMAN [1963] who solved the Schrödinger equation (1) self-consistently for all the elements in the Periodic Table.

Figure 4 illustrates several important features to which we will be returning throughout this chapter. Firstly, the valence energy levels vary *linearly across* a given period. As

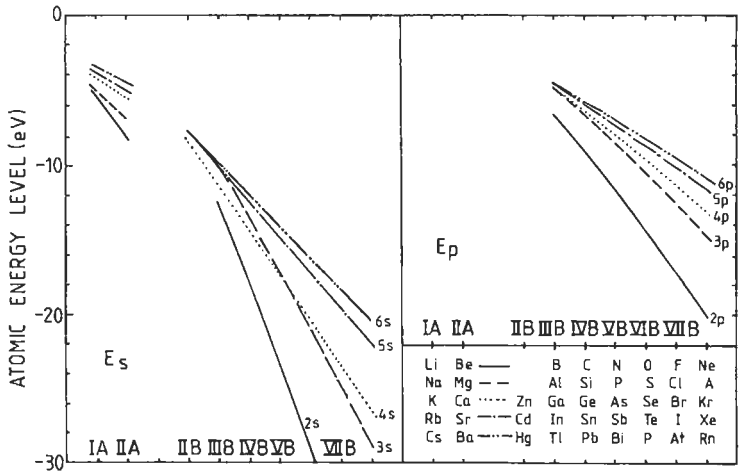

Fig. 4. The valence s and p energy levels (after HERMAN AND SKILLMAN [1963]).

the nuclear charge Ze increases, the electrons are bound more tightly to the nucleus. However, rather than varying as Z^2, which would be the result for the energy levels of a hydrogenic ion of charge Ze, the presence of the other valence electrons induces the linear behaviour observed. Secondly, the valence s and p energy levels become less strongly bound as one moves *down* a given group, which is to be expected from the hydrogenic energy levels displayed in fig. 3. But there is an exception to this rule: the 4s level has come down and crosses below the 3s level to the left of group VB. This is a direct consequence of the presence of the occupied 3d shell (cf. table 2, ch. 2) whose electrons do not completely screen the core from the valence 4s electrons, which therefore feel a more attractive potential than their 3s counterparts in the preceding row. We will see in § 6.2 that this reversal in the expected ordering of the valence s energy levels is reflected in the structural properties of binary AB compounds containing group IIIB elements. Thirdly, it is clear from fig. 4 that the energy *difference* $E_p - E_s$ decreases as one goes from the rare gases to the alkali metals, from right to left across a given period. This will strongly influence the nature of the energy bands and the bonding in the bulk, since if the energy difference is small, s and p electrons will hybridize to form common sp bands.

Figure 5 shows the valence s and d energy levels across the 3d and 4d transition metal series, after HERMAN and SKILLMAN [1963]. The energy levels correspond to the atomic configuration $d^{N-1}s$, where N is the total number of valence electrons, because this is the configuration closest to that of the bulk metal. Again there are several important features. Firstly, we see that the energy variation is *linear across* the transition metal series as the d shell is progressively filled with electrons. However, once the noble metal group IB is reached the d shell contains its full complement of ten electrons, so that any further increase in atomic number Z adds the additional valence electrons to the

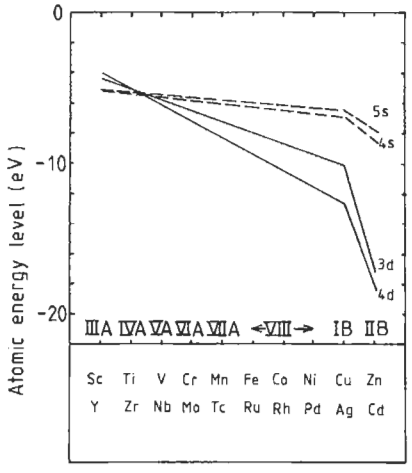

Fig. 5. The valence s and d energy levels across the 3d and 4d transition series (after HERMAN AND SKILLMAN [1963]).

sp outer shell and pulls the d energy rapidly down as is evidenced by the change of slope in fig. 5. Secondly, whereas the *valence* s energy level becomes slightly less strongly bound as one moves *down* a given group, the valence 4d energy level becomes more strongly bound than the valence 3d away from the beginning of the transition-metal series. This behaviour appears to be related to the mutual coulomb repulsion between the negatively charged valence electrons. The 3d orbitals are much more compact than the 4d orbitals, so that the putting of electrons into the 3d shell leads to a more rapid increase in repulsive energy than in the 4d shell. The Sd and 6s energy levels have not been plotted in fig. 5 because *relativistic* effects, which are not included in the Schrödinger equation (1), become important for *heavy* atoms in the Periodic Table. Relativistic corrections are discussed in ch. 2 of HERMAN and SKILLMAN [1963]. Thirdly, since $E_s - E_d$ is about 3 eV in copper but 6 eV in silver, it is not surprising that the noble metals display different physical characteristics.

A concept that is often used in physical metallurgy to discuss and order properties is that of *atomic size.* The microscopic description of the atom, which is provided by quantum mechanics, should be able to give some measure of this quantity. We have seen that quantum mechanics replaces the stationary Bohr *orbits* of radius a_n by orbitals which are not located with a fixed radius but are smeared out in probability-clouds described by $|\psi|^2$. The angular dependence of these probability-clouds has been displayed in fig. 2. We now discuss their radial dependence.

The solution of the Schrödinger equation for a central spherically symmetric potential can be written in separable form, namely:

$$\psi_{nlm}(\boldsymbol{r}) = R_{nl}(r)Y_l^m(\theta, \phi), \tag{10}$$

where r, θ and ϕ are spherical polar coordinates. As expected, the *angular* distribution depends only on the angular-momentum quantum numbers l and m, the functions $Y_l^m(\theta\ \phi)$ being the so-called *spherical harmonics* (see, e.g., SCHIFF [1968]). Y_0^0 is a constant and Y_1^0 is proportional to $\cos\theta$ as we have already mentioned. The *radial* function $R_{nl}(r)$ depends on the principal and orbital quantum numbers, n and l respectively, and therefore changes with energy level E_{nl}. For the hydrogen atom the first few radial functions are (in atomic units)

$$R_{1s}(r) = 2e^{-r}, \tag{11}$$

$$R_{2s}(r) = \frac{1}{\sqrt{2}}\left(1 - \tfrac{1}{2}r\right)e^{-r/2}, \tag{12}$$

$$R_{2p}(r) = \frac{1}{\sqrt{24}}re^{-r/2}. \tag{13}$$

A conceptually useful quantity is the probability of finding the electron at some distance r from the nucleus (in any direction), which is determined by the *radial probability density,* $P_{nl}(r) = r^2R_{nl}^2(r)$.

Figure 6 shows the radial function R_{nl} and the probability density, P_{nl}, as a function

of r for the 1s, 2s and 2p states of hydrogen. We see that there is *maximum* probability of locating the electron at the first Bohr radius a_1 for the 1s state and at the second Bohr radius a_2 for the 2p state. The *average* or expectation value of the radial distance r is given by:

$$\bar{r}_{nl} = n^2\left[1 + \tfrac{1}{2}\left(1 - l(l+1)/n^2\right)\right], \tag{14}$$

so that $\bar{r}_{1s} = 1.5a_1$, $\bar{r}_{2s} = 1.5a_2$ and $\bar{r}_{2p} = 1.25a_2$. Therefore, the 2s orbital is more extended than the corresponding 2p orbital, as is evident from fig. 6. This is due to the fact that all solutions of the Schrödinger equation must be *orthogonal* to one another, i.e., if ψ_{nlm} and $\psi_{n'l'm'}$ are any two solutions and ψ^* is the complex conjugate of ψ, then

$$\int \psi^*_{nlm}\psi_{n'l'm'}\, d\boldsymbol{r} = 0. \tag{15}$$

If the states have *different* angular-momentum character then the angular integration over the spherical harmonics [cf. (eq. 10)] guarantees orthogonality. But if the states have the *same* angular-momentum character then the orthogonality constraint implies that:

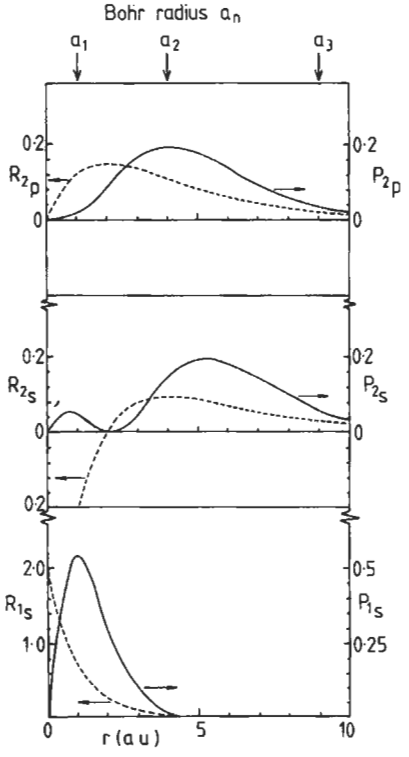

Fig. 6. The radial function R_{nl} (dashed lines) and the probability density, P_{nl} (solid lines) as a function of r for the 1s, 2s and 2p states of hydrogen.

References: p. 129.

$$\int_0^\infty R_{nl}(r)\, R_{n'l}(r) r^2\, dr = 0. \tag{16}$$

For the orbitals drawn in fig. 6, therefore, we must have

$$\int_0^\infty R_{1s}(r)\, R_{2s}(r) r^2\, dr = 0, \tag{17}$$

which can be verified by substituting eqs. (11) and (12) into this equation. This is the origin of the *node* at $r=2$ au in $R_{2s}(r)$, where the radial function changes sign. The 3s radial function must be orthogonal to the 2s and, therefore, has two nodes, the 4s has three nodes, etc. Just as the energetically lowest I s state has *no* nodes, so the 2p, 3d and 4f states are nodeless since they correspond to the states of lowest energy for a given l (see fig. 3).

The position of the outer node of the *valence* electron's radial function may be used as a measure of an l-dependent core size, since we have seen that the node arises from the constraint that the valence state be orthogonal to the more tightly bound core states. This relationship between node and core size has been demonstrated quantitatively for the case of the sp core of the 4d transition metals (PETTIFOR [1977] and § 4.3) and has been discussed for other elements by BLOCH and SCHATTEMAN [1981]. A not unrelated measure of size has been adopted by ZUNGER [1980] who defined l-dependent radii R_l by the condition (cf. ST. JOHN and BLOCH [1974]) that

$$v_l^{\text{eff}}(R_l) = 0, \tag{18}$$

where $v_l^{\text{eff}}(r)$ is some effective angular-momentum dependent atomic potential (which is given by a first-principles screened pseudopotential, cf. § 3.3). Figure 7 shows the resultant values of $-R_s^{-1}$ and $-R_p^{-1}$ for the sp bonded elements. We see a *linear* variation across a given period and a close similarity with the valence energy level behaviour

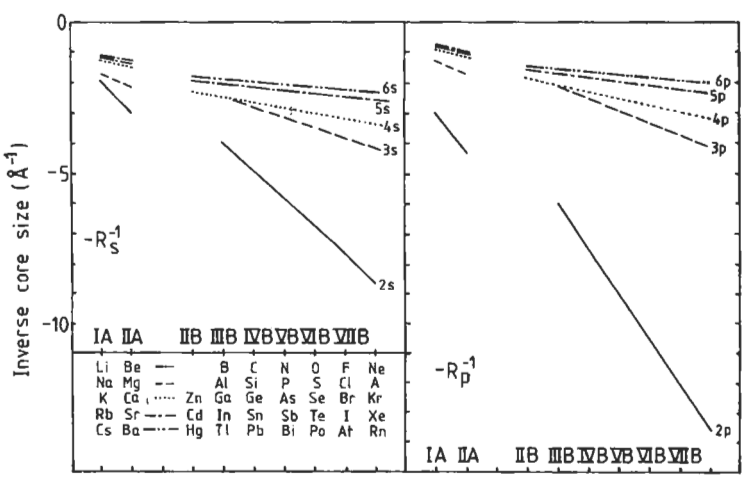

Fig. 7. The negative of the inverse s and p pseudopotential radii (after ZUNGER [1980]).

illustrated in fig. 4. As expected, the s and p radii contract *across* a period as the nuclear charge Ze increases, and they expand *down* a column as additional full orbital shells are pulled into the core region. Figure 7 clearly demonstrates that the sizes of the second-row elements B, C, N and O are a lot smaller than those of the other elements in their respective groups, a fact which manifests itself in their different alloying behaviour (cf. fig. 38, below).

2.2. Bond formation

In this subsection we consider what happens to the atomic energy levels and wave functions as two atoms A and B are brought together from infinity to form the AB diatomic molecule.

Suppose the A and B valence electrons are characterized by the free atomic energy levels E_A and E_B and wave functions ψ_A and ψ_B, respectively. Let us assume, following the experience of theoretical quantum chemists, that the *molecular* wave function ψ_{AB} can be written as a *linear combination of the atomic orbitals*,

$$\psi_{AB} = c_A\psi_A + c_B\psi_B, \tag{19}$$

where c_A and c_B are constant coefficients. Then it follows from the Schrödinger eq. (1) that

$$(\hat{H} - E)(c_A\psi_A + c_B\psi_B) = 0 \tag{20}$$

where $\hat{H}$ is the Hamiltonian operator for the AB dimer, namely $\hat{H} = -\nabla^2 + V_{AB}$ where we have used the fact that $\hbar^2/2m = 1$ in atomic units. Multiplying by ψ_A (or ψ_B) and integrating over all space we find the well-known secular equation (taking $\psi^* = \psi$ as ψ is real)

$$\begin{bmatrix} H_{AA} - E & H_{AB} - ES_{AB} \\ H_{BA} - ES_{BA} & H_{BB} - E \end{bmatrix} \begin{bmatrix} c_A \\ c_B \end{bmatrix} = 0 \tag{21}$$

where the Hamiltonian and overlap matrix elements are given by

$$H_{\alpha\beta} = \int \psi_\alpha \hat{H} \psi_\beta \, \mathrm{d}\boldsymbol{r} \tag{22}$$

and

$$S_{\alpha\beta} = \int \psi_\alpha \psi_\beta \, \mathrm{d}\boldsymbol{r}. \tag{23}$$

The Hamiltonian matrix elements can be simplified by assuming that the molecular potential V_{AB} is given by the sum of the free atom potentials V_A and V_B. The *diagonal* elements H_{AA} and H_{BB} then take the free atom values E_A and E_B respectively, provided the energy shift due to the neighbouring potential fields can be neglected. The *off-diagonal* element H_{AB} can be written

$$H_{AB} = \int \psi_A \overline{V} \psi_B \, \mathrm{d}\boldsymbol{r} + \overline{E}S \tag{24}$$

References: p. 129.

where $\bar{E} = \frac{1}{2}(E_A + E_B)$, $\bar{V} = \frac{1}{2}(V_A + V_B)$, and $S = S_{AB}$. Substituting in equation (21) we obtain the secular equation

$$\begin{bmatrix} -\frac{1}{2}\Delta E - (E - \bar{E}) & h - (E - \bar{E})S \\ h - (E - \bar{E})S & \frac{1}{2}\Delta E - (E - \bar{E}) \end{bmatrix} \begin{bmatrix} c_A \\ c_B \end{bmatrix} = 0 \tag{25}$$

where $\Delta E = (E_B - E_A)$ is the *atomic energy level mismatch* and $h = \int \psi_A \bar{V} \psi_B \, d\boldsymbol{r}$ is the hopping or *bond integral* between atoms A and B. For s orbitals h is negative since the average potential $\bar{V}$ is attractive.

Equation (25) may be solved for the eigenvalues and eigenvectors. To first order in the overlap integral S

$$E_{AB}^{\pm} = \bar{E} - hS \pm (1 + \delta^2)^{1/2} h \tag{26}$$

and

$$\psi_{AB}^{\pm} = c_A^{\pm} \psi_A + c_B^{\pm} \psi_B \tag{27}$$

where

$$c_A^{\pm} = \frac{1}{\sqrt{2}} \left[1 \pm (\delta - S) / (1 + \delta^2)^{1/2} \right]^{1/2} \tag{28}$$

$$c_B^{\pm} = \pm \frac{1}{\sqrt{2}} \left[1 \mp (\delta + S) / (1 + \delta^2)^{1/2} \right]^{1/2} \tag{29}$$

with $\delta = \Delta E / 2|h|$. Therefore, as shown in Fig. 8 s valent diatomic molecules are characterized by bonding and anti-bonding states which are separated in energy by the amount ω_{AB} such that

$$\omega_{AB}^2 = 4h^2 + (\Delta E)^2. \tag{30}$$

The formation of the bond is accompanied by a redistribution of the electronic charge. It follows from equation (27) that the electronic density which corresponds to occupying the bonding state with two valence electrons of opposite spin, namely $\rho_{AB} = 2(\psi_{AB}^{-})^2$ may be written in the form

$$\rho_{AB}(\boldsymbol{r}) = (1 + \alpha_i)\rho_A(\boldsymbol{r}) + (1 - \alpha_i)\rho_B(\boldsymbol{r}) + \alpha_c \rho_{bond}(\boldsymbol{r}) \tag{31}$$

where

$$\rho_{A(B)}(\boldsymbol{r}) = \left[\psi_{A(B)}(\boldsymbol{r}) \right]^2 \tag{31a}$$

and

$$\rho_{bond}(\boldsymbol{r}) = 2\psi_A(\boldsymbol{r})\psi_B(\boldsymbol{r}) - S[\rho_A(\boldsymbol{r}) + \rho_B(\boldsymbol{r})]. \tag{32}$$

α_i and α_c are determined by the normalised energy level mismatch δ through

$$\alpha_i = \delta/\left(1+\delta^2\right)^{1/2} \tag{33}$$

and

$$\alpha_c = 1/\left(1+\delta^2\right)^{1/2}. \tag{34}$$

For the case of *homonuclear* diatomic molecules $\delta = 0$, so that the change in the electronic charge distribution on forming the molecule is given solely by the *bond charge* contribution ρ_{bond} in equation (31). This is illustrated in fig. 9 for the case of the hydrogen molecule where we see that, as expected, the electronic charge has moved from the outer regions of the molecule into the bond region between the atoms. We should note from equations (32) and (23) that the total charge associated with ρ_{bond} over all space is identically zero. Equation (32) shows explicitly that the formation of the bond is a *quantum* interference effect, the charge piling up in the bond region because of the interference contribution $\psi_A\,\psi_B$. In practice, in order to satisfy the virial theorem, the formation of the bond is accompanied by some modification of the free-atom orbitals $\psi_{A,B}$, which has been discussed by RUEDENBERG [1962] and SLATER [1963]. This leads to the energy levels $E_{A,B}$ not being directly identifiable as the *free*-atom energy levels, a point which will be discussed further in § 5.2 on transition-metal bonding.

For the case of a *heteronuclear* diatomic molecule $\delta \neq 0$, so that the electronic charge distribution in equation (31) contains the *ionic* contributions $\alpha_i \rho_A$ and $-\alpha_i \rho_B$ in addition to

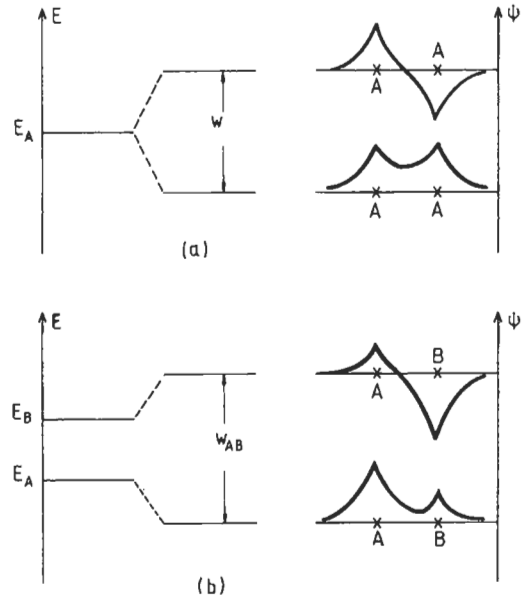

Fig. 8. The bonding (lower lines) and antibonding (upper lines) states for (a) the homonuclear and (b) the heteronuclear diatomic molecule.

the *covalent* bond charge contribution $\alpha_c \rho_{bond}$. α_i and α_c are said to measure the degree of ionicity and covalency of the bond (see, for example, COULSON *et al.* [1962], PHILIPS [1970] and HARRISON [1980]). Note that $\alpha_i^2 + \alpha_c^2 = 1$.

The term covalency will be used in this chapter to describe the bonding which arises from the *quantum* mixing of *valence* states on neighbouring sites into the final state wave function. It is not necessarily associated with *pairs* of electrons of opposite spin, as the lone electron in the hydrogen molecular ion H_2^+, for example, shows all the characteristics of the covalent homonuclear bond discussed above.

A diatomic molecule has cylindrical symmetry about the internuclear axis, so that angular momentum is conserved in this direction. Quantum-mechanically this implies that the state of the molecule is characterized by the quantum number m, where $m\hbar$ gives the component of the angular momentum along the molecular axis. However, unlike the free atom where the $(2l+1)$ different m values are degenerate, the degeneracy is lifted in the molecule. By analogy with the s, p, d, ... states of a free atom representing the orbital quantum numbers $l=0, 1, 2, \ldots$, it is customary to refer to σ, π, δ, ... states of a molecule as those corresponding to $m=0, \pm1, \pm2, \ldots$ respectively.

Figure 10 illustrates the different characteristics of the σ, π and δ bonds. We have seen from our previous discussion on the homonuclear molecule that a given atomic energy level will split into bonding and antibonding states separated by $2|h|$, where h is the matrix element that couples states ψ_A and ψ_B together through the atomic potential

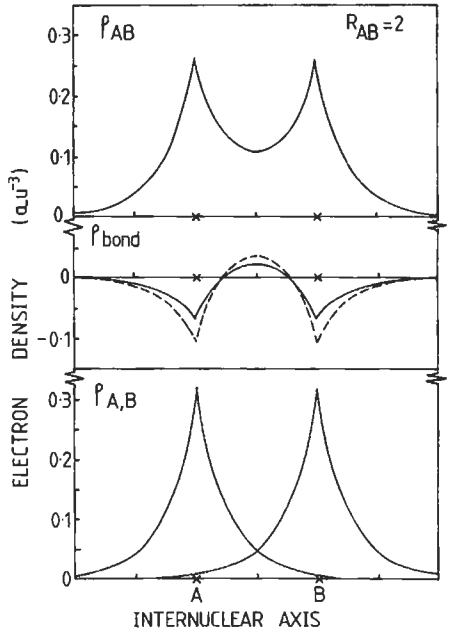

Fig. 9. The electron density of the homonuclear molecule (upper panel) can be regarded as the sum of the *non-interacting* free-atom electron densities (lower panel) and the *quantum-mechanically* induced bond density (middle panel). The dashed curve represents the first-order result, eq. (32), for the bond density.

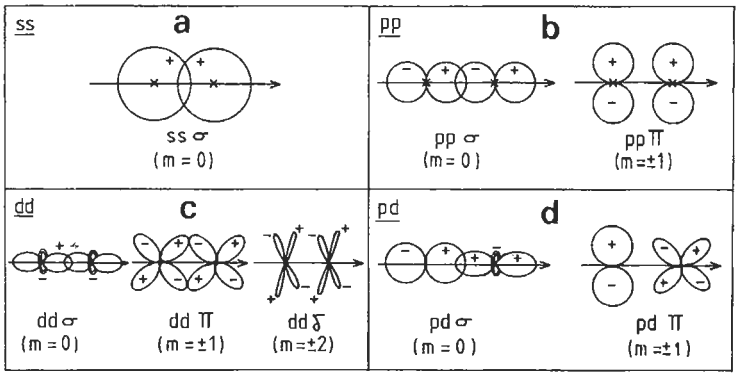

Fig. 10. The formation of σ, π and δ bonds from s, p and d orbitals, see text.

v. If $\psi_{A,B}$ are spherically symmetric s orbitals, then a ssσ bond is formed as shown schematically in fig. 10a. If $\psi_{A,B}$ are p orbitals whose probability clouds are drawn in fig. 2, then the threefold degenerate free atom level (excluding spin degeneracy) splits into the singly degenerate ppσ molecular state (m = 0) and the doubly degenerate ppπ molecular state (m = ±1) shown in fig. 10b. If $\psi_{A,B}$ are d orbitals, whose probability clouds are sketched in fig. 2, then the fivefold degenerate free atom level splits into the singly degenerate ddσ molecular state (m = 0) and the two doubly degenerate molecular states ddπ (m = ±1) and ddδ (m = ±2) as shown in fig. 10c. For the case of a heteronuclear molecule such as NbC where the carbon p orbitals overlap the niobium d orbitals, a pd bond will be formed from the pdσ and pdπ states illustrated in fig. 10d. It is clear from fig. 10 that the σ bond is relatively strong since the angular lobes point along the molecular axis and can give rise to a large overlap in the bonding region. On the other hand, the ppπ and ddδ bonds will be relatively much weaker since their angular lobes extend in the plane perpendicular to the molecular axis. The importance of σ, π and δ bonding in determining the behaviour of the *bulk* band structure will be demonstrated in § 4.1.

The term covalency will be used in this chapter to describe the bonding which arises from the *quantum* mixing of *valence* states on neighbouring sites into the final-state wave function. It is not necessarily associated with *pairs* of electrons of opposite spin, as the lone electron in the hydrogen molecular ion H_2^+, for example, shows all the characteristics of the covalent homonuclear bond discussed above.

2.3. Band formation

Figure 11 illustrates how the free-atom energy levels E_s and E_p broaden into *bands* as the atoms are brought together from infinity to form the bulk. Just as the single atomic energy level splits into two energy levels on bringing two atoms together (cf. fig. 8a), so the single level on a free atom splits into N levels on bringing N atoms together, thereby conserving the total number of electronic states. These levels lie between the bottom of the band, which represents the most bonding state, and the top of the band, which represents the most antibonding state. Since $N \approx 10^{23}$ for 1 cm^3 of bulk material, these N

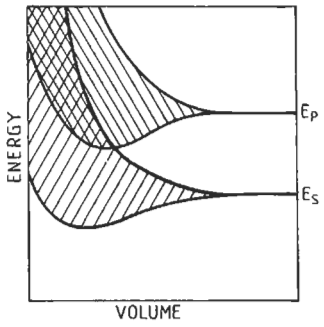

Fig. 11. Energy band formation.

levels form a quasi-continuous band of states and it is customary to work with the *density of states, n(E),* where $dN = n(E)\,dE$ gives the number of states in the energy range from E to $E + dE$. The conservation of states requires that:

$$\int_{-\infty}^{\infty} n_\alpha(E)\,dE = \begin{cases} 2 \\ 6 \\ 10 \end{cases} \quad \text{for } \alpha = \begin{cases} \text{s} \\ \text{p}, \\ \text{d} \end{cases} \tag{35}$$

where $n_\alpha(E)$ is the density of states *per atom* associated with a given atomic s, p or d level.

In metals at their equilibrium volume, the bands corresponding to different valence energy levels overlap and mix as shown on the left-hand side of fig. 11. The mixing or hybridization in *simple* metals is such as to produce *nearly-free-electron*-like behaviour of the energy bands and density of states, which is discussed in the following section. On the other hand, the density of states in *transition* metals is dominated by a well defined d band, which is accurately described within the *tight-binding* approximation by a linear combination of atomic d orbitals and is discussed in § 4.

3. *Simple-metal bands*

3.1. The free-electron approximation

It had been realized before the advent of quantum mechanics that some metallic properties such as electrical or thermal conductivity could be well understood by regarding the valence electrons as a non-interacting gas of particles which were *free* to travel throughout the metal without being affected by the parent ions. However, it remained for quantum mechanics to remove a striking failure of the classical model, namely its inability to explain the *linear* temperature dependence of the electronic heat capacity, since according to classical statistical mechanics a free particle has a *constant* heat capacity of $\frac{3}{2}$, where k_B is the Boltzmann constant.

The Schrödinger equation for a free-electron gas may be written in atomic units as

$$-\left(\frac{\partial^2}{\partial x^2}+\frac{\partial^2}{\partial y^2}+\frac{\partial^2}{\partial z^2}\right)\psi(\boldsymbol{r}) = E\psi(\boldsymbol{r}) \tag{36}$$

If the electrons are contained within a box of side L then a normalized solution of eq. (36) is the *plane wave:*

$$\psi_k(\boldsymbol{r}) = L^{-3/2}\ \mathrm{e}^{\mathrm{i}\boldsymbol{k}\cdot\boldsymbol{r}}, \tag{37}$$

which can be seen by writing $\boldsymbol{k}\bullet\boldsymbol{r}$ as $k_x x+k_y y+k_z z$ and substituting eq. (37) into eq. (36).

This solution corresponds to an electron with kinetic energy E given by:

$$E = k_x^2 + k_y^2 + k_z^2 = k^2. \tag{38}$$

Since the kinetic energy equals $p^2/2m$ where p is the electronic momentum, it follows from eq. (38) that

$$p^2 = 2mE = 2mk^2 = \hbar^2 k^2, \tag{39}$$

using $\hbar^2/2m = 1$. Thus, we have recovered the de Broglie relation

$$p = \hbar k = h/\lambda, \tag{40}$$

because $k = 2\pi/\lambda$ where λ is the wavelength of the plane wave.

The wavelength, λ, of the plane wave is constrained by *boundary conditions* at the surface of the box. For the case of the Bohr orbits in the hydrogen atom, de Broglie had argued that λ must be such that *integer* multiples of the wavelength fit around the circumference of the orbit. Similarly, imposing *periodic* boundary conditions on the box, which in one dimension corresponds to joining both ends in a closed ring, we have that

$$n_x\lambda_x = n_y\lambda_y = n_z\lambda_z = L, \tag{41}$$

where n_x, n_y, n_z are integers. Therefore,

$$\boldsymbol{k} = \frac{2\pi}{L}\left(n_x, n_y, n_z\right) \tag{42}$$

so that the allowed values of the wave vector $\boldsymbol{k}$ are discrete and fall on a fine mesh as illustrated in fig. 12.

By Pauli's exclusion principle each state corresponding to a given $\boldsymbol{k}$ can contain *two* electrons of opposite spin. Therefore, at absolute zero all the states $\boldsymbol{k}$ will be occupied within a sphere of radius k_F, the so-called *Fermi sphere,* because these correspond to the states of lowest energy (cf. fig. 13a). The Fermi wave vector k_F may be related to the total number of valence electrons, N, by

$$\tfrac{4}{3}\pi k_F^3 2V/(2\pi)^3 = N, \tag{43}$$

where $V = L^3$, since it follows from eq. (42) that unit volume of $\boldsymbol{k}$-space contains $V/(2\pi)^3$ states capable of holding two electrons each. Thus,

$$\boldsymbol{k}_F = \left(3\pi^2 N/V\right)^{1/3} \tag{44}$$

References: p. 129.

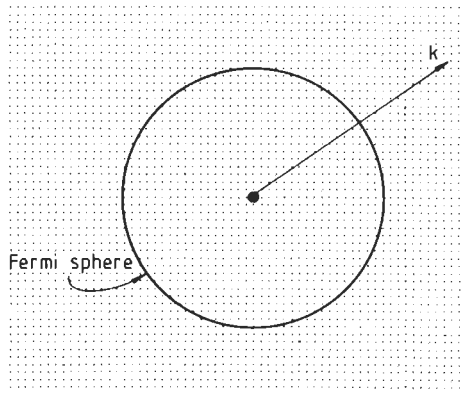

Fig. 12. The fine mesh of allowed $\boldsymbol{k}$ values. At absolute zero only the states $\boldsymbol{k}$ within the Fermi sphere are occupied.

and the corresponding *Fermi energy*, E_F is given by

$$E_F = \left(3\pi^2 N/V\right)^{2/3}. \tag{45}$$

The electron concentration, N/V, for sodium, magnesium and aluminium at their equilibrium atomic volumes is such that the Fermi energy E_F equals 3.2, 7.1 and 11.6 eV respectively.

The free-electron *density of states* $n(E)$ may be obtained from eq. (43) by writing it in the form

$$N(E) = \left(V/3\pi^2\right)E^{3/2}, \tag{46}$$

where $N(E)$ is the total number of states of both spins available with energies less than E. Differentiating eq. (46) with respect to the energy gives the density of states:

$$n(E) = \left(V/2\pi^2\right)E^{1/2}, \tag{47}$$

which is illustrated in fig. 13b. We can now see why the experimental electronic heat capacity did not obey the classical result of $\frac{3}{2}k_B$. By Pauli's exclusion principle the electrons can be excited only into the *unoccupied* states above the Fermi energy E_F.

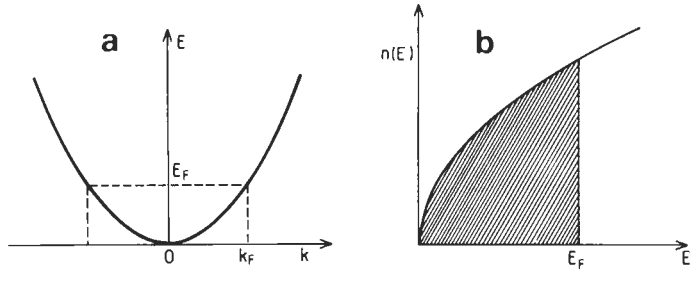

Fig. 13. The free-electron energy dispersion $E(\boldsymbol{k})$ (a) and density of states $n(E)$ (b).

Therefore, only those electrons within about $k_B T$ of E_F will have enough thermal energy to be excited across E_F. Since $k_B T \approx 0.03$ eV at room temperature, these electrons will comprise a very small fraction, $f \approx k_B T/E_F$, of the total number of electrons N. The classical heat capacity is accordingly reduced by this factor f, as is observed experimentally. Using the correct Fermi-Dirac statistics to describe the occupation of the electron states, we find (see, e.g., KITTEL [1971]):

$$C_V = \frac{\pi^2}{2} k_B (k_B T/E_F) \tag{48}$$

in agreement with the previous qualitative argument.

3.2. Nearly-free-electron approximation

The electrons in a real metal are affected by the *crystalline* lattice, since the potential which they feel is not uniform but varies *periodically* as

$$v(\boldsymbol{r} + \boldsymbol{R}) = v(\boldsymbol{r}) \tag{49}$$

where $\boldsymbol{R}$ is any lattice vector. (For simplicity we will be considering only those crystal structures, such as fcc or bcc, in which there is only *one* atom per primitive lattice site, in contrast to hcp or the diamond structure, for example, which have a basis of *two* atoms, cf. KITTEL [1971].) Consider first an infinite *one-dimensional* periodic lattice of atoms with repeat distance a such that

$$v(x + na) = v(x). \tag{50}$$

Because all the atoms are equivalent, the probability of locating the electron about a site must be the same for all sites, so that:

$$|\psi(x + na)|^2 = |\psi(x)|^2. \tag{51}$$

For $n = 1$ this implies that

$$\psi(x + a) = e^{ika}\psi(x), \tag{52}$$

where k is a number (in units of $1/a$) which specifies the *phase factor* e^{ika} linking the wave functions on neighbouring sites. Repeating eq. (52) n times gives:

$$\psi_k(x + na) = e^{ikna}\psi_k(x), \tag{53}$$

which is the usual statement of *Bloch's theorem* in one dimension. Thus the translational symmetry of the lattice leads to the eigenfunctions being characterized by the Bloch vector, k. However, k is only defined modulo $(2\pi/a)$, since $k + m(2\pi/a)$ results in the same phase factor in eq. (53) as k alone. It is, therefore, customary to label the wave function ψ_k by restricting k to lie within the *first Brillouin zone*, defined by

$$-\pi/a \leq k \leq +\pi/a. \tag{54}$$

We note that in one dimension na is a direct lattice vector, whereas $m(2\pi/a)$ is a *reciprocal* lattice vector. Their product is an integer multiple of 2π.

Extending these ideas to three dimensions, Bloch's theorem, eq. (53) may be written as:

$$\psi_k(\boldsymbol{r}+\boldsymbol{R}) = e^{i\boldsymbol{k}\cdot\boldsymbol{R}}\psi_k(\boldsymbol{r}), \tag{55}$$

where $\boldsymbol{R}$ is any *direct lattice* vector which may be expressed in terms of the fundamental translation vectors $\boldsymbol{a}_1$, $\boldsymbol{a}_2$, $\boldsymbol{a}_3$ as:

$$\boldsymbol{R} = n_1\boldsymbol{a}_2 + n_2\boldsymbol{a}_2 + n_3\boldsymbol{a}_3, \tag{56}$$

where n_1, n_2, n_3 are integers. The corresponding *reciprocal lattice* vectors are defined by:

$$\boldsymbol{G} = m_1\boldsymbol{b}_1 + m_2\boldsymbol{b}_2 + m_3\boldsymbol{b}_3, \tag{57}$$

where m_1, m_2, m_3 are integers and the fundamental basis vectors are:*

$$\left.\begin{aligned}\boldsymbol{b}_1 &= (2\pi/\tau)\boldsymbol{a}_2 \times \boldsymbol{a}_3\\ \boldsymbol{b}_2 &= (2\pi/\tau)\boldsymbol{a}_3 \times \boldsymbol{a}_1\\ \boldsymbol{b}_3 &= (2\pi/\tau)\boldsymbol{a}_1 \times \boldsymbol{a}_2\end{aligned}\right\}, \tag{58}$$

with $\tau = |\boldsymbol{a}_1\bullet(\boldsymbol{a}_2 \times \boldsymbol{a}_3)|$ being the volume of the primitive unit cell defined by $\boldsymbol{a}_1$, $\boldsymbol{a}_2$ and $\boldsymbol{a}_3$. It is apparent from their definition (58) that

$$\boldsymbol{a}_i \bullet \mathbf{b}_j = 2\pi\delta_{ij}, \tag{59}$$

where $\delta_{ij}=1$ for $i=j$ but zero otherwise.

The phase factor in eq. (55) only defines the Bloch vector within a reciprocal lattice vector $\boldsymbol{G}$ since it follows from eqs. (56)–(59) that $\boldsymbol{G}\bullet\boldsymbol{R}$ is an integer multiple of 2π. Just as in the one-dimensional case, it is customary to label the wave function ψ_k by restricting $\boldsymbol{k}$ to lie within the *first Brillouin zone* which is the closed volume about the origin in reciprocal space formed by bisecting near-neighbour reciprocal lattice vectors. For example, consider the *simple cubic* lattice with basis vectors $\boldsymbol{a}_1$, $\boldsymbol{a}_2$, $\boldsymbol{a}_3$ along the Cartesian axes x, y, z respectively. Because $a_1=a_2=a_3=a$ it follows from eq. (58) that the reciprocal space basis vectors $\boldsymbol{b}_1$, $\boldsymbol{b}_2$, $\boldsymbol{b}_3$ also lie along x, y and z respectively, but with magnitude $(2\pi/a)$. Thus, the reciprocal lattice is also simple cubic and it is shown in fig. 14 in the x–y plane. It is clear that the bisectors of the first nearest-neighbour (100) reciprocal lattice vectors form a closed volume about the origin which is not cut by the second or any further nearest-neighbour bisectors. Hence, the Brillouin zone is a cube of volume $(2\pi/a)^3$. From eq. (42) it contains as many allowed $\boldsymbol{k}$ points as there are primitive unit cells in the crystal. Figure 15 illustrates the corresponding Brillouin zones for the body-centred cubic and face-centred cubic lattices (see, e.g., KITTEL [1971]).

The solutions E_k of the Schrödinger equation for $\boldsymbol{k}$ lying within the Brillouin zone

* Note the additional factor of 2π compared to the definition of reciprocal lattice vectors in the appendix of ch. 11.

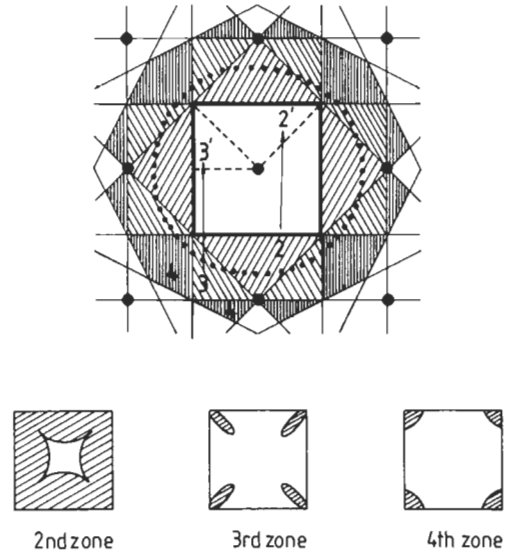

Fig. 14. The first four zones of the simple cubic lattice corresponding to $k_z = 0$. The dotted circle represents the cross-section of a spherical Fermi surface.

determine the *band structure*. Figure 16 shows the band structure of aluminium in the $|100\rangle$ and $|111\rangle$ directions, after MORUZZI *et al.* [1978]. It is very similar to the free-electron band structure

$$E_k = (\boldsymbol{k} + \boldsymbol{G})^2 \tag{60}$$

which results from folding the free-electron eigenvalues shown in fig. 13a into the first Brillouin zone. This "folding-in" is illustrated in fig. 14 for the case of the *simple cubic* lattice. For this two-dimensional cross-section we see that the four contributions to the second zone *2* may be translated through (100) reciprocal lattice vectors into the four

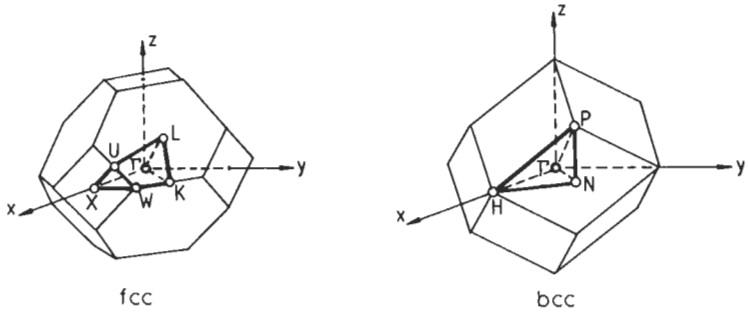

Fig. 15. The fcc and bcc Brillouin zones. Γ labels the centre of the zone. The intersections of the $|100\rangle$ and $|111\rangle$ directions with the Brillouin-zone boundary are labelled X and L in the fcc case and H and P in the bcc case.

zones 2′, which together completely fill the reduced Brillouin zone in the x–y plane. Similarly, the third and fourth zones shown in fig. 14 may each be translated through reciprocal lattice vectors to fill the first Brillouin zone. For the *fcc* lattice the two lowest eigenvalues given by eq. (60) in the $|100\rangle$ direction are:

$$E_k^{(1)} = k^2, \qquad E_k^{(2)} = (\boldsymbol{k}+\boldsymbol{g})^2, \tag{61}$$

where $\boldsymbol{k} = (k_x, 0, 0)$ and $\boldsymbol{g} = (2\pi/a)(\bar{2}, 0, 0)$. These two eigenvalues are degenerate at the zone boundary $\boldsymbol{X}$, where $\boldsymbol{k} = (2\pi/a)(1, 0, 0)$ because from eq. (61) they both take the value $4\pi^2/a^2$. For aluminium $a = 7.60$ au and $4\pi^2/a^2 = 9.3$ eV, so that the two free-electron eigenvalues given by eq. (61) reflect the broad behaviour of the band structure shown along ΓX in fig. 16.

However, in order to recover the *energy gap* at the zone boundary X, it is necessary to lift the free-electron degeneracy by perturbing the free-electron gas with the periodic potential of the crystalline lattice. Within the *nearly-free-electron* (NFE) approximation this is achieved by writing the wave function ψ_k as a linear combination of the plane-wave eigenfunctions corresponding to the two free-electron eigenvalues given by eq. (61); that is:

$$\psi_k = c_1\psi_k^{(1)} + c_2\psi_k^{(2)}, \tag{62}$$

where from eq. (37):

$$\psi_k^{(1)} = V^{-1/2}\exp(i\boldsymbol{k}\cdot\boldsymbol{r}), \tag{63}$$

$$\psi_k^{(2)} = V^{-1/2}\exp[i(\boldsymbol{k}+\boldsymbol{g})\cdot\boldsymbol{r}]. \tag{64}$$

Substituting eq. (62) into the Schrödinger equation (1), pre-multiplying by $\psi_k^{(1)*}$ or $\psi_k^{(2)*}$ and integrating over the volume of the crystal, V, yields the *NFE secular equation*:

$$\begin{pmatrix} k^2 - E & v(200) \\ v(200) & (\boldsymbol{k}+\boldsymbol{g})^2 - E \end{pmatrix}\begin{pmatrix} c_1 \\ c_2 \end{pmatrix} = 0. \tag{65}$$

$v(200)$ is the $(2\pi/a)(2, 0, 0)$ Fourier component of the crystalline potential, where

$$v(\boldsymbol{g}) = \frac{1}{V}\int v(\boldsymbol{r})\, e^{i\boldsymbol{g}\cdot\boldsymbol{r}}\, d\boldsymbol{r}. \tag{66}$$

The energy, E in eq. (65) is measured with respect to the average potential $v(000)$. Non-trivial solutions exist if the secular determinant vanishes, i.e. if

$$\begin{vmatrix} k^2 - E & v(200) \\ v(200) & (\boldsymbol{k}+\boldsymbol{g})^2 - E \end{vmatrix} = 0. \tag{67}$$

This quadratic equation has solutions

$$E_k = \tfrac{1}{2}\left[k^2 + (\boldsymbol{k}+\boldsymbol{g})^2\right] \pm \tfrac{1}{2}\left\{\left[(\boldsymbol{k}+\boldsymbol{g})^2 - k^2\right]^2 + \left[2v(200)\right]^2\right\}^{1/2}. \tag{68}$$

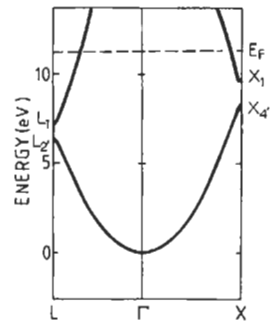

Fig. 16. The band structure of fcc aluminium (after MORUZZI *et al.* [1978]).

Therefore, at the zone boundary X where $k^2=(\boldsymbol{k}+\boldsymbol{g})^2$, the eigenvalues are given by

$$E_X = 4\pi^2/a^2 \pm v(200) \tag{69}$$

and the eigenfunctions are given from eqs. (62) and (65) by:

$$\psi_X = (2/V)^{1/2} \times \begin{cases} \cos(2\pi x/a) \\ \sin(2\pi x/a) \end{cases}. \tag{70}$$

Thus the presence of the periodic potential has opened up a gap in the free electron band structure with energy separation

$$E_{gap}^X = 2|v(200)|. \tag{71}$$

Because the energy gap at X in aluminium is about 1 eV (cf. fig. 16), the magnitude of the Fourier component of the potential within this simple NFE treatment is only 0.5 eV. This is small compared to the free-electron Fermi energy of more than 10 eV in aluminium and, therefore, the band structure E_k and the density of states $n(E)$ are nearly-free-electron-like to a very good approximation.

The NFE behaviour has been observed experimentally in studies of the *Fermi surface,* the surface of constant energy E_F in $\boldsymbol{k}$-space, which separates filled states from empty states at $T=0$. For a free-electron gas the Fermi surface is spherical as illustrated in fig. 12. However, in simple metals we have seen that the free-electron band structure is perturbed by the periodic lattice potential, and energy gaps open up across zone boundaries. As illustrated in fig. 14 for the simple cubic lattice, a spherical free-electron Fermi surface (whose cross-section is represented by the circle of solid dots) will be folded into the first Brillouin zone by the relevant reciprocal lattice vectors. The states in the second zone 2, for example, are folded back into 2′ in the reduced zone, thereby giving rise to the shaded occupied regions of $\boldsymbol{k}$-space and the corresponding Fermi surface indicated in the lower panel of fig. 14. Similarly, the occupied states in the third and fourth zones are folded back into the reduced Brillouin zone as shown. Therefore, even though the crystalline potential may be very weak, it is sufficient to destroy the *spherical* free-

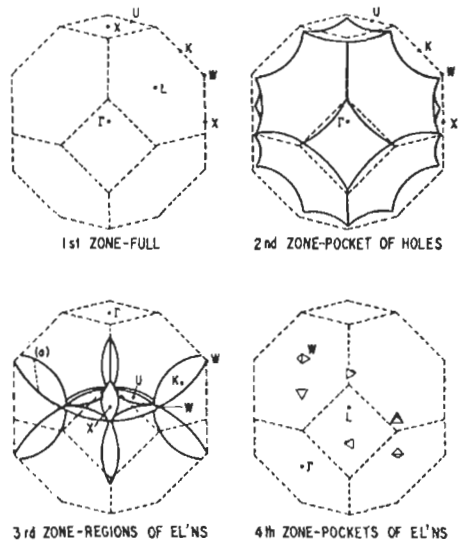

Fig. 17. The free-electron Fermi surface of aluminium (after HARRISON [1959]).

electron Fermi surface and to create a new Fermi surface topology, as is illustrated in fig. 14 by the appearance of the electron *pockets* in the third and fourth zones. A very simple procedure for constructing the Fermi surfaces of free-electron-like materials has been suggested by HARRISON [1959, 1960] and fig. 17 shows the resulting Fermi surface of fcc aluminium. A much more detailed treatment of Fermi surfaces may be found in HARRISON [1966], HEINE and WEAIRE [1970] and KITTEL [1971], where the interested reader is also referred for a discussion of transport properties and concepts such as holes and effective mass.

3.3. Volume dependence

Although the energy bands of simple metals *appear* to be describable by the NFE approximation as discussed in the previous subsection, there is a major difficulty. If the (200) Fourier component of the aluminium lattice potential is estimated from *first principles* using eq. (66), then

$$v(200) \approx -5 \text{ eV}. \tag{72}$$

But the magnitude of this is ten times larger than the value we obtained by *fitting* to the first-principles band structure of MORUZZI *et al.* [1978], namely $|v(200)| = 0.5$ eV. Moreover, by looking at the symmetry of the eigenfunctions at X, we see from fig. 16 that the bottom of the band gap corresponds to X_4, or p-like symmetry whereas the top of the band gap corresponds to X_1 or s-like symmetry (see, e.g., TINKHAM [1964]). It follows from fig. 2 and eq. (70) that the NFE states at the bottom and top of the band gap correspond to $\sin(2\pi x/a)$ and $\cos(2\pi x/a)$, respectively. Therefore, in the state with *lower* energy the electron is never located in the planes containing the ion cores, which

correspond to $x = na/2$ for the fcc lattice, since $\sin(2\pi x/a)$ vanishes. Instead, the electron has maximum probability of being located midway between these atomic planes. This implies that the relevant Fourier component of the atomic potential is *repulsive,* thereby driving the electrons away from the ion cores, i.e.

$$v^{\text{fit}}(200) = +0.5 \text{ eV}. \tag{73}$$

The origin of the discrepancy between eqs. (72) and (73) is easily found once it is remembered that the NFE bands in aluminium are formed from the *valence* 3s and 3p electrons. These states must be orthogonal to the s and p *core* functions as outlined in § 2.1 and they, therefore, contain nodes in the core region as illustrated for the case of the 2s wavefunction in fig. 6. In order to reproduce these very-short-wavelength oscillations, plane waves of *very high* momentum must be included in the plane-wave expansion of ψ_k, so that a linear combination of only the *two* lowest energy plane waves in eq. (62) is an extremely bad approximation. In 1940, HERRING circumvented this problem by starting at the outset with a basis of plane waves that had *already* been orthogonalized to the core states, the so-called orthogonalized plane-wave (OPW) basis. The OPW method led to a secular determinant for the eigenvalues that was identical to the NFE determinant, except that in addition to the Fourier component of the crystal potential $v(\boldsymbol{G})$ there is also a *repulsive* contribution coming from the core-orthogonality constraint. This tended to cancel the *attractive* coulomb potential term in the core region, thereby resulting in much weaker net Fourier components and hence nearly-free-electron-like behaviour of the band structure E_k for the simple metals.

This led to the concept of the *pseudopotential* in which the true potential $v(r)$ in the Schrödinger equation (1) is replaced by a much *weaker* potential $v_{\text{ps}}(\boldsymbol{r})$ which is chosen to preserve the original eigenvalues E_k so that

$$\left(-\nabla^2 + v_{\text{ps}}\right)\phi_k = E_k\phi_k \tag{74}$$

(see, e.g., HARRISON [1966] and HEINE and WEAIRE [1970]). The pseudo-*eigenfunctions*, ϕ_k, however, differ from the true eigenfunctions ψ_k because in general they do *not* contain the nodes in the core region as these have been pseudized-away by the inclusion of the repulsive core component in v_{ps}. A plane-wave expansion of ϕ_k therefore, leads to rapidly convergent eigenvalues E_k in eq. (74). Thus, the NFE approximation will provide a good description of the band structure of simple metals provided the Fourier components of the pseudopotential rather than the true potential are taken in the NFE secular equation (67).

Pseudopotentials are not unique, and certain criteria have been given for their choice (see, e.g., BACHELET *et al.* [1982] and VANDERBILT [1990]). However, in this chapter we shall describe only the Ashcroft *empty-core* pseudopotential because of its simplicity. In 1966, ASHCROFT assumed that the cancellation between the repulsive core-orthogonality contribution and the attractive coulomb contribution is exact within some ion core radius R_c, so that:

$$v_{\text{ps}}^{\text{ion}}(\boldsymbol{r}) = \begin{cases} 0 & r < R_c \\ -2Z/r & \text{for } r > R_c \end{cases} \tag{75}$$

References: p. 129.

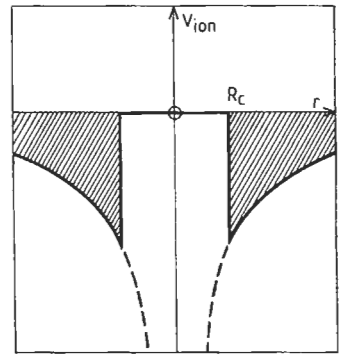

Fig. 18. The Ashcroft empty-core pseudopotential.

where the *ionic* potential falls off coulombically outside the core (cf. $e^2=2$ in atomic units). The Ashcroft empty-core pseudopotential is shown in fig. 18. The resulting ionic lattice has Fourier components given by eq. (66), namely:

$$v_{ps}^{ion}(q) = -\left(8\pi Z/\Omega q^2\right)\cos qR_c, \tag{76}$$

where Ω is the volume per atom. In the absence of the core $R_c=0$ and the Fourier components are *negative* as expected. However, in the presence of the core the Fourier components oscillate in sign and may, therefore, take *positive* values. For the case of aluminium the Ashcroft empty-core radius is about 1.2 au (cf. table 16–1 of HARRISON [1980]) and $v_{ps}^{ion}(200)$ will, therefore, be positive. The corresponding Fourier components $v_{ps}(q)$ are obtained from eq. (76) by allowing the free-electron gas to screen the bare ionic lattice. The resulting Fourier components of the aluminium potential are illustrated in fig. 19 for the more sophisticated HEINE and ABARENKOV [1964] pseudopotential. We see that the values of $v_{ps}(111)$ and $v_{ps}(200)$ are in good agreement with the values, 0.17 and 0.53 eV respectively, which are obtained from fitting the first-principles band structure within the NFE approximation (cf. fig. 16, eq. (71) and p. 52 of MORUZZI *et al.* [1978]).

Figure 20 shows the densities of states, $n(E)$ of the sp-bonded simple metals, which have been computed from first principles by MORUZZI *et al.* [1978]. We see that Na, Mg

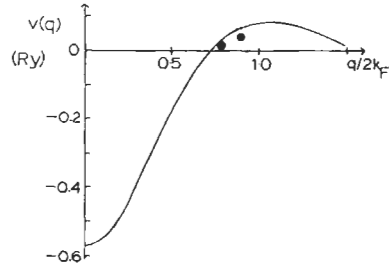

Fig. 19. The HEINE AND ABARENKOV [1964] aluminium pseudopotential $v_{ps}(q)$. The two points give the values of $v_{ps}(111)$ and $v_{ps}(200)$ deduced from fig. 16 using eq. (71).

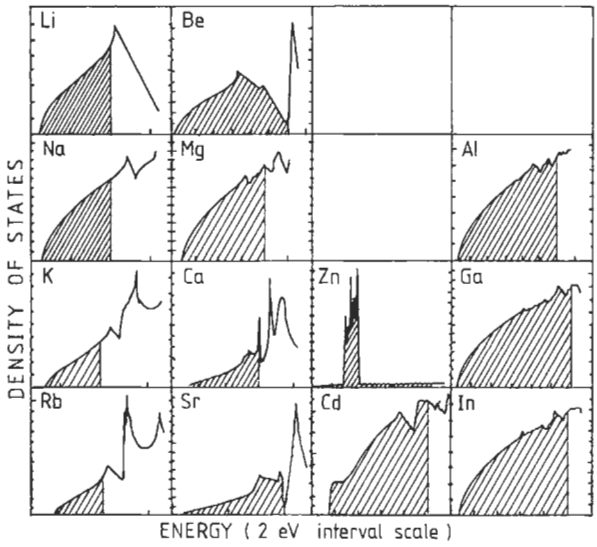

Fig. 20. The density of states, $n(E)$, of sp-bonded metals (after MORUZZI *et al.* [1978]).

and Al across a period and Al, Ga and In down a group are good NFE metals, because their densities of states are only very small perturbations of the free-electron density of states shown in fig. 13b. However, we see that Li and Be display very strong deviations from free electron behaviour. This is a direct consequence of these elements having no p core electrons, so that there is no repulsive core-orthogonality component to cancel the attractive coulomb potential which the valence 2p electrons feel. This leads to sizeable Fourier components of the potential and hence very large band gaps. For example, in fcc Be, $E_{\text{gap}}^{\text{L}} = 5.6$ eV compared to the gap of only 0.34 eV in Al, where L is the point $(2\pi/a)(\frac{1}{2},\frac{1}{2},\frac{1}{2})$ in fig. 15. In fact, the band gaps in different directions at the Brillouin zone boundary (cf. fig. 16) are nearly large enough for a gap to open up in the Be density of states, thereby leading to semiconducting behaviour. We note that the effective potential which the valence electrons feel in Li or Be depends on whether they have s- or p-type character, because there *are* 1s core states but no p core states. Such an l-dependent potential is said to be *non-local* (cf. HARRISON [1966] and HEINE and WEAIRE [1970]), whereas the Ashcroft empty-core pseudopotential of fig. 18 is *local.*

The heavier alkalis K and Rb and alkaline earths Ca and Sr have their occupied energy levels affected by the presence of the respective 3d or 4d band which lies just above the Fermi energy (cf. the relative positions of the s and d free-atom energy levels in fig. 5). This leads to a more than free-electron admixture of $l=2$ component into the occupied energy states, which requires the use of non-local pseudopotential theory for accurate agreement with experimental properties (see e.g., TAYLOR and MACDONALD [1980] and MORIARTY [1982]). It is clear from fig. 20 that Sr is not a simple NFE metal since the perturbation is very strong and the hybridized bottom of the d band has moved

References: p. 129.

below the Fermi energy. Just as in Be, a gap has nearly opened up at E_F, and theoretically it requires only 0.3 Gpa of pressure to turn Sr into a semiconductor, which is in reasonable agreement with high-pressure resistivity data (JAN and SKRIVER [1981]). The group-IIB elements Zn and Cd, on the other hand, have their valence states strongly distorted by the presence of the *filled* d band. In fig. 5 we see that the 5s–4d energy separation in Cd is larger than the 4s 3d separation in Zn, which results in the Cd 4d band lying about 1 eV below the bottom of the valence 5sp band (p. 152 of MORUZZI *et al.* [1978]). Figure 20, therefore, demonstrates that not all simple metals display good NFE behaviour and particular care needs to be taken with Li, Be and the group-II elements on either side of the transition metal series.

The presence of the ion core in simple metals determines the volume dependence of the energy bands. Wigner and Seitz had calculated the behaviour of the bottom of the NFE band in sodium in their classic paper of 1933. They argued that since the bottom of the band corresponded to the most bonding state, it satisfied the *bonding* boundary condition implicit in eq. (27), namely that the gradient of the wave function vanishes across the boundary of the *Wigner–Seitz cell.* This cell is formed in *real* space about a given atom by bisecting the near-neighbour position vectors in the same way that the Brillouin zone is formed in *reciprocal* space. The Wigner-Seitz cell of the bcc lattice is the fcc Brillouin zone and vice versa (cf. KITTEL [1971]). Since there are 12 nearest neighbours in the fcc lattice and 14 first and second nearest neighbours in the bcc lattice, it is a very good approximation to replace the Wigner–Seitz *cell* by a Wigner–Seitz *sphere* of the same volume (cf. fig. 15). Imposing the bonding boundary condition across the Wigner Seitz sphere of radius S, where

$$\Omega = \tfrac{4}{3}\pi S^3, \tag{77}$$

the energy of the bottom of the band Γ_1 is fixed by

$$\left[\mathrm{d}R_s(r,E)/\mathrm{d}r\right]_{r=S,E=\Gamma_1} = 0, \tag{78}$$

where $R_s(r, E)$ is the $l=0$ solution of the radial Schrödinger equation within the Wigner–Seitz sphere. The bonding boundary condition is determined by the $l=0$ radial function because the bottom of the NFE band at Γ_1 is a pure s state (cf. fig. 16).

Figure 21 shows the resulting behaviour of the bottom of the band Γ_1, in sodium as a function of S after WIGNER and SEITZ [1933]. We see that as the free atoms are brought together from infinity, the bonding state becomes more and more bonding until about 3 au when Γ_1, turns upwards and rapidly loses its binding energy. This behaviour is well described *at metallic densities* by the Frohlich–Bardeen expression,

$$\Gamma_1^{\mathrm{ws}} = -(3Z/S)\left[1-(R_c/S)^2\right] \tag{79}$$

since the single valence electron of sodium is assumed to feel only the potential of the *ion* at the Wigner–Seitz sphere centre so that over the boundary

$$v(S) = -2Z/S, \tag{80}$$

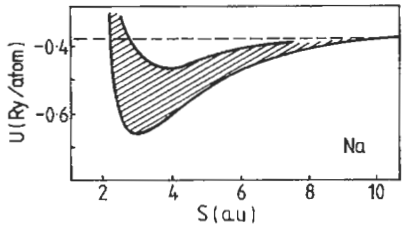

Fig. 21. The total energy, U, as a function of Wigner–Seitz radius, S, for sodium (after WIGNER and SEITZ [1933]). The bottom of the conduction band, Γ_1, is given by the lower curve, to which is added the average kinetic energy per electron (the shaded region).

where $Z=1$ for the monovalent alkali metals (see, e.g., § 3.2 of CALLAWAY [1964]). R_c may be identified as the radius of an Ashcroft empty-core pseudopotential, because the potential energy of one electron distributed uniformly throughout the Wigner–Seitz sphere with an Ashcroft ionic potential at its centre is given by eq. (79). It follows from eq. (79) that the maximum binding energy of this state Γ_1, occurs for

$$S_m = \sqrt{3}R_c. \tag{81}$$

Since for sodium $R_c \approx 1.7$ au (ASHCROFT and LANGRETH [1967] and HARRISON [1980]), eq. (81) predicts that Γ_1, has a minimum at about 2.9 au. This is in good agreement with the curve in fig. 21, which was obtained by solving the radial Schrödinger equation subject to the boundary condition eq. (78).

WIGNER and SEITZ [1933] assumed that the valence electrons of sodium have free-electron-like kinetic energy and density of states, which from fig. 20 is clearly a good approximation. It follows from eqs. (45) and (77) that the Fermi energy E_F may be written as:

$$E_F = \Gamma_1^{WS} + (9\pi/4)^{2/3}/S^2. \tag{82}$$

In § 5 we follow up our understanding of the behaviour of the energy bands by discussing the *total* energy of simple metals and the different factors influencing bulk properties such as equilibrium atomic volume and bulk modulus.

4. *Transition-metal bands*

4.1. Tight-binding approximation

Transition metals are characterized by a partially filled d band, which is well described within the *tight-binding* (TB) approximation by a linear combination of atomic d orbitals. We shall illustrate the TB method (see, e.g., CALLAWAY [1964], PETTIFOR [1992] and SUTTON [1993]) by considering first the simpler case of a lattice of atoms with overlapping *s-state* atomic wave functions ψ_s and corresponding free atomic energy levels E_s. Generalizing eq. (19) for the diatomic molecule to a periodic lattice of N

atoms, we can write the crystal wave function ψ_k as a linear combination of the atomic orbitals:

$$\psi_k(\boldsymbol{r}) = N^{-1/2} \sum_{\boldsymbol{R}} e^{i\boldsymbol{k}\cdot\boldsymbol{R}} \psi_s(\boldsymbol{r} - \boldsymbol{R}), \tag{83}$$

where the phase factor automatically guarantees that $\psi_k(\boldsymbol{r})$ satisfies Bloch's theorem, eq. (55). Assuming that the crystal potential is the sum of the atomic potentials $v(\boldsymbol{r} - \boldsymbol{R})$ and following the method and approximations outlined through eqs. (19)–(30), the eigenvalue E_k may be written as:

$$E_k = E_s + \sum_{R \neq 0} e^{i\boldsymbol{k}\cdot\boldsymbol{R}} \int \psi_s^*(\boldsymbol{r}) v(\boldsymbol{r}) \psi_s(\boldsymbol{r} - \boldsymbol{R})\, d\boldsymbol{r}, \tag{84}$$

where the non-orthogonality and three-centre contributions have been neglected because they do not contribute to first order. Since the atomic s orbitals are spherically symmetric, the ssσ hopping matrix elements in eq. (84) do not depend on the direction of $\boldsymbol{R}$ but only on the magnitude R (see fig. 10), so that

$$E_k = E_s + \sum_{R \neq 0} e^{i\boldsymbol{k}\cdot\boldsymbol{R}} ss\sigma_R. \tag{85}$$

The TB band structure E_k for a *simple cubic* lattice with s orbitals may now be quickly found. Assuming that the hopping matrix elements couple only to the six *first* nearest-neighbour atoms with position vectors $\boldsymbol{R}$ equal to $(\pm a, 0, 0)$ $(0, \pm a, 0)$ and $(0, 0, \pm a)$ eq. (85) gives

$$E_k = E_s + 2ss\sigma_1 \left(\cos k_x a + \cos k_y a + \cos k_z a\right), \tag{86}$$

where $\boldsymbol{k} = (k_x, k_y, k_z)$ Thus the eigenvalues vary *sinusoidally* across the Brillouin zone. The bottom, E^- and top, E^+ of the s band correspond to the Bloch states at the centre of the Brillouin zone (0, 0, 0) and at the zone boundary $(\pi/a)(1, 1, 1)$ respectively. It follows from eq. (86) that

$$E^{\pm} = E_s \pm 6|ss\sigma_1| \tag{87}$$

because $ss\sigma_1$ is negative as can be deduced from fig. 10 and eq. (84). Comparing E^- with eq. (26) and fig. 8a for the diatomic molecule, we see that the most bonding state in the simple cubic lattice corresponds to *maximum* bonding with all six nearest neighbours simultaneously, which from fig. 10 is only possible for the spherically symmetric s orbital case.

The structure of the TB p band may be obtained by writing ψ_k as a linear combination of the *three* p Bloch sums corresponding to the atomic p_x, p_y, and p_z orbitals, where x, y and z may be chosen along the crystal axes for a cubic lattice. That is,

$$\psi_k(\boldsymbol{r}) = N^{-1/2} \sum_{\alpha = x,y,z} c_\alpha \sum_{\boldsymbol{R}} e^{i\boldsymbol{k}\cdot\boldsymbol{R}} \psi_\alpha(\boldsymbol{r} - \boldsymbol{R}), \tag{88}$$

which leads to the 3×3 TB secular determinant for the p band, namely

$$\left|\left(E_{\mathrm{p}} - E_k\right)\delta_{\alpha\alpha'} + T_{\alpha\alpha'}\right| = 0, \tag{89}$$

where

$$T_{\alpha\alpha'} = \sum_{R\neq 0} \mathrm{e}^{\mathrm{i}\,k\cdot R} \int \psi_\alpha^*(r) v(r) \psi_{\alpha'}(r - R)\mathrm{d}r. \tag{90}$$

It is clear from fig. 10 that the hopping matrix elements in eq. (90) *do* depend on the direction of R because the p_x, p_y, and p_z orbitals are angular dependent. SLATER and KOSTER [1954] showed that they can be written directly in terms of the two fundamental hopping integrals $pp\sigma_R$ and $pp\pi_R$ and the direction cosines (l, m, n) of R.

For a *simple cubic* lattice with only first-nearest-neighbour hopping the matrix elements $T_{\alpha\alpha'}$ may be evaluated to give

$$T_{xx} = 2pp\sigma_1 \cos k_x a + 2pp\pi_1\left(\cos k_y a + \cos k_z a\right), \tag{91}$$

with T_{yy} and T_{zz} obtained from T_{xx} by cyclic permutation. The off-diagonal matrix elements vanish for the simple cubic lattice. Therefore, at the centre of the Brillouin zone, Γ, the eigenvalues are *triply* degenerate (if spin is neglected) and given from eqs. (89) and (91) by

$$E_\Gamma^{(3)} = E_{\mathrm{p}} + 2pp\sigma_1 + 4pp\pi_1. \tag{92}$$

This degeneracy is *partially* lifted along the $|100\rangle$ symmetry direction, because from eq. (91) the band structure consists of the *singly* degenerate level

$$E_\Delta^{(1)} = E_{\mathrm{p}} + 4pp\pi_1 + 2pp\sigma_1 \cos k_x a \tag{93}$$

and the *doubly* degenerate level

$$E_\Delta^{(2)} = E_{\mathrm{p}} + 2\left(pp\sigma_1 + pp\pi_1\right) + 2pp\pi_1 \cos k_x a, \tag{94}$$

where the former results from the p_x orbitals and the latter from the p_y and p_z orbitals. The degeneracy is *totally* lifted along a general k direction as from eqs. (89) and (91) there will be three distinct non-degenerate energy levels.

Finally, the structure of the TB d band may be obtained by writing ψ_k as a linear combination of the *five* d Bloch sums corresponding to the five atomic orbitals illustrated in fig. 2. This results in a 5×5 TB secular determinant from which the d band structure may be computed (SLATER and KOSTER [1954]). Starting from first-principles band theory, ANDERSEN [1973] has shown that within the *atomic sphere approximation* (ASA) *canonical* d bands may be derived which depend neither on the lattice constant nor on the particular transition metal, but only on the crystal structure. This approximation leads to hopping integrals of the form

$$\left.\begin{aligned} dd\sigma_R &= -5 \\ dd\pi_R &= 4 \\ dd\delta_R &= -1 \end{aligned}\right\} \times \tfrac{2}{5} W\left(S/R\right)^5, \tag{95}$$

References: p. 129.

where W is the width of the d band, which is obtained by imposing the bonding and antibonding boundary conditions over the Wigner-Seitz *sphere* of radius S. It follows from eq. (95) that the hopping integrals scale uniformly with the band width W and do not depend on the lattice constant as it is the ratio S/R that enters. They fall off quickly with distance as the inverse fifth power.

Figure 22 shows the resulting d band structure for the fcc and bcc lattices along the $|111\rangle$ and $|100\rangle$ directions in the Brillouin zone (ANDERSEN [1973]). We see that at the centre of the Brillouin zone, Γ, there are two energy levels, one of which is *triply* degenerate, the other *doubly* degenerate. The former comprises the xy, yz and xz, T_{2g} orbitals which from fig. 2 are equivalent to one another in a cubic environment. The latter comprises the $x^2 - y^2$, $3z^2 - r^2 E_g$ orbitals which by pointing along the cubic axes are not equivalent to the T_{2g}, orbitals. The degeneracy is partially lifted along the $|111\rangle$ and $|100\rangle$ symmetry directions as indicated in fig. 22, because eigenfunctions which are equivalent at $\boldsymbol{k}=0$ may become non-equivalent for $\boldsymbol{k} \neq 0$ due to the translational phase factor $\exp(i\boldsymbol{k}\cdot\boldsymbol{R})$ (see fig. 8.8 of TINKHAM [1964]).

The band structure of NiO (MATTHEISS [1972]) is shown in fig. 23 because it illustrates s, p and d band behaviour. The three bands arise from the oxygen 2s, 2p and the nickel 3d valence levels, respectively, the ordering being determined by the relative positions of their atomic energy levels in figs. 4 and 5. The Brillouin zone is *face-centred* cubic since the NaCl crystal structure of NiO consists of two interpenetrating fcc lattices, one containing the sodium atoms, the other the chlorine atoms. In the $|100\rangle$ direction along ΓX the s and p band structure is not too dissimilar from that given for the *simple* cubic lattice by eqs. (86), (93) and (94). The d band structure along ΓX in NiO is also similar to that of the fcc canonical d band in fig. 22, except that one level, which joins the upper state at Γ to the *bottom* of the canonical d band at X, has been pushed up and runs across the *top* of the d band in NiO. This is the result of mixing or *hybridization* between the s, p and d blocks in the TB secular determinant (SLATER and KOSTER [1954]), whose strength is determined for example by the non-vanishing $pd\sigma$ and $pd\pi$ hopping matrix elements shown in fig. 10. This mixing can only occur between Bloch states with the same symmetry (TINKHAM [1964]). At the zone boundary X there is only *one* d band state which has the same symmetry X_1 as the s band state. (There are no d band states with the same symmetry as the p band states at X.) The influence of the hybridization on the band structure is enhanced by *orthogonality* constraints which can add a further repulsive contribution to the d states because they must be orthogonal to the valence s and p levels lying beneath them in energy.

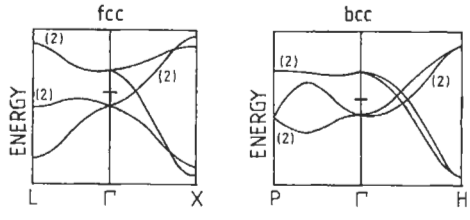

Fig. 22. The fcc and bcc d band structure (after ANDERSEN [1973]).

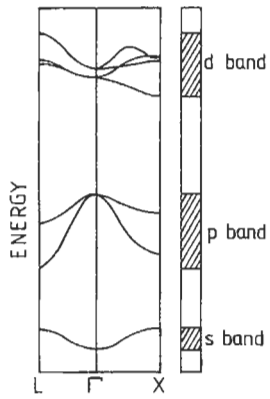

Fig. 23. The band structure of NiO (after MATTHEISS [1972]).

The bands in fig. 23 illustrate an apparent failure of one-electron theory. NiO is an *insulator.* However, adding the ten nickel and six oxygen valence electrons to the bands shown results in the d band containing only eight of its possible ten electrons [cf. eq. (35)]. Thus, the band structure presented in fig. 23 predicts that NiO is a *metal.* The origin of this dramatic failure of band theory was investigated by MOTT [1949], who considered what happens to a lattice of hydrogen atoms as the lattice constant is decreased from some very large value. Initially each atom has a single 1s valence electron associated with it as in the free atom state. The system will, therefore, be *insulating,* because in order for an electron to hop through the lattice it requires an energy given by the difference between the ionization potential of 13.6 eV (corresponding to the atomic 1s level) and the electron affinity of 0.75 eV. This energy difference of about 13 eV is a measure of the coulomb repulsion U between *two* 1s antiparallel spin electrons sitting on the *same* atomic site. However, as the lattice constant decreases the atomic 1s level broadens into a band of states of width W so that the insulating gap will decrease like $U - W$. Therefore, for some sufficiently small lattice spacing W will be large enough for the system to become *metallic* and the hydrogen lattice undergoes a Mott metal-insulator transition.

The very different conducting behaviour of the 3d valence electrons in metallic nickel and insulating nickel oxide can now be qualitatively understood. The width of the d band in NiO is about 2 eV (MATTHEISS [1972]), whereas in pure Ni it is about 5 eV (MORUZZI *et al.* [1978]) since the Ni–Ni internuclear separation is smaller than in the oxide. Because the value of the screened intra-atomic coulomb integral U in 3d transition metals is about 4 eV, U/W is *greater* than unity for NiO but *less* than unity for Ni. Thus, we expect the former to be insulating and the latter metallic as observed experimentally.

The *breakdown* of conventional band theory at *large* lattice spacings can best be illustrated by considering the hydrogen molecule (cf. fig. 8a). In the ground state the two valence electrons 1 and 2 occupy the same bonding molecular orbital ψ_{AB}^{-} with opposite spin, so that the total molecular wave function may be written within the one electron approximation as

$$\psi(1,2) = \psi^{-}_{AB}(1)\psi^{-}_{AB}(2). \tag{96}$$

Substituting from eq. (27), multiplying through and neglecting the normalization factor $[2(1 + S)]^{-1}$ we have

$$\psi(1,2) = \big(\psi_A(1)\psi_B(2) + \psi_B(1)\psi_A(2) + \psi_A(1)\psi_A(2) + \psi_B(1)\psi_B(2)\big). \tag{97}$$

The first two contributions correspond to the two possible *neutral* atom states with a single electron associated with each atom, whereas the latter correspond to the two *ionic* states A^-B^+ and A^+B^- respectively. Since the hydrogen molecule dissociates into two *neutral* atoms, we see that $\psi(1, 2)$ gives the wrong behaviour at large separations (see, e.g., SLATER [1963]).

In practice, the Mott transition to the insulating phase is accompanied by the appearance of local *magnetic* moments (BRANDOW [1977]) so that the band model must be generalized to allow for antiferromagnetic solutions of the Schrödinger equation (SLATER [1951a]; cf. § 8). Within local spin density functional (LSDF) theory (cf. § 1) this leads to a good curve of total energy versus internuclear separation for the hydrogen molecule because the theory now goes over to the neutral free-atom limit (GUNNARSSON and LUNDQUIST [1976]). However, although the antiferromagnetic state leads to a band gap opening up at the Fermi level in NiO (SLATER [1951a]), a proper understanding of CoO and the temperature-dependent properties of these *insulators* can only be obtained by using a more sophisticated *non-local* treatment of exchange and correlation (BRANDOW [1977], JONES and GUNNARSSON [1989]). Fortunately, the bulk properties of simple and transition *metals* considered in this chapter can be well understood within the *local* approximation, even though non-locality can play a role in the finer details of the band structure (see, e.g., Ni; COOKE *et al.* [1980]).

4.2. Hybrid NFE-TB bands

Transition metals are characterized by a fairly tightly-bound d band that overlaps and hybridizes with a broader nearly-free-electron sp band as illustrated in fig. 24. This difference in behaviour between the valence sp and d electrons arises from the d shell lying *inside* the outer valence s shell, thereby leading to small overlap between the d orbitals in the bulk. For example, from eq. (14) the average radial distance of the hydrogenic 3d and 4s wave functions are in the ratio 0.44 :1. Thus, we expect the band structure of transition metals to be represented accurately by a hybrid NFE–TB secular equation of the form (HODGES *et al.* [1966] and MUELLER [1967]):

$$\begin{vmatrix} C - EI & H \\ H^{\dagger} & D - EI \end{vmatrix} = 0 \tag{98}$$

where C and D are sp-NFE and d-TB matrices respectively [cf. eqs. (67) and (89)]. H is the hybridization matrix which couples and mixes together the sp and d Bloch states with the same symmetry, and I is the unit matrix.

A secular equation of this H–NFE–TB form may be derived (HEINE [1967], HUBBARD

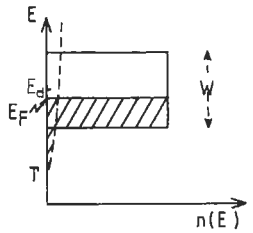

Fig. 24. A schematic representation of transition metal sp (dashed curve) and d (solid curve) densities of states when sp–d hybridization is neglected.

[1967] and JACOBS [1968]) by an exact transformation (PETTIFOR [1972a]) of the first-principle band structure equations of KORRINGA [1946], KOHN and ROSTOKER [1954] (KKR). They have solved the Schrödinger equation (1) by regarding the lattice as a periodic array of scattering sites which individually scatter the electrons with a change in phase η_l. Transition-metal sp valence electrons are found to be scattered very little by the lattice so that they exhibit NFE behaviour with η_0 and η_1 close to zero. Transition-metal d electrons, on the other hand, are strongly scattered, the $l=2$ phase shift showing *resonant* behaviour given by

$$\tan \eta_2(E) = \tfrac{1}{2}\Gamma/(E_d - E), \tag{99}$$

where E_d and Γ determine the position and width of the resonance. This allows the KKR equations to be transformed directly into the H–NFE–TB form, in which the two centre TB hopping integrals and hybridization matrix elements are determined explicitly by the two resonant parameters E_d and Γ. The non-orthogonality contributions to the secular equation (MUELLER [1967]) are obtained by linearizing the implicit energy-dependent matrices C, D and H in a Taylor expansion about E_d.

The nonmagnetic band structure of fcc and bcc iron is shown in fig. 25, being computed from the H–NFE–TB secular equation with resonant parameters $E_d = 0.540$ Ry and $\Gamma = 0.088$ Ry (PETTIFOR [1970a]). The NFE pseudopotential matrix elements were chosen by fitting the first-principle values of WOOD [1962] at the pure p states N_1, $v(_{110} = 0.040$ Ry), L_2' ($v_{111} = 0.039$ Ry) and X_4, ($v_{200} = 0.034$ Ry). Comparing the band structure of iron in the $|100\rangle$ and $|111\rangle$ directions with the canonical d bands in fig. 22, we see there is only the *one* d level with symmetry Δ_1 and Λ_1 respectively which hybridizes with the lowest NFE band, the remaining four d levels being unperturbed. Because of the canonical nature of the pure TB d bands (ANDERSEN [1973]), the band structure of all fcc and bcc transition metals will be very similar to that shown in fig. 25 for iron.

The transition-metal density of states, $n(E)$, is not uniform throughout the band as shown schematically in fig. 24 but displays considerable structure that is characteristic of the given crystal lattice. This is seen in fig. 26 for the bcc, fcc and hcp densities of states, which were calculated by the H–NFE–TB secular equation neglecting non-orthogonality contributions with $E_d = 0.5$ Ry and $\Gamma = 0.06$ Ry (PETTIFOR [1970b]). These early histogram densities of states are displayed rather than more accurate recent

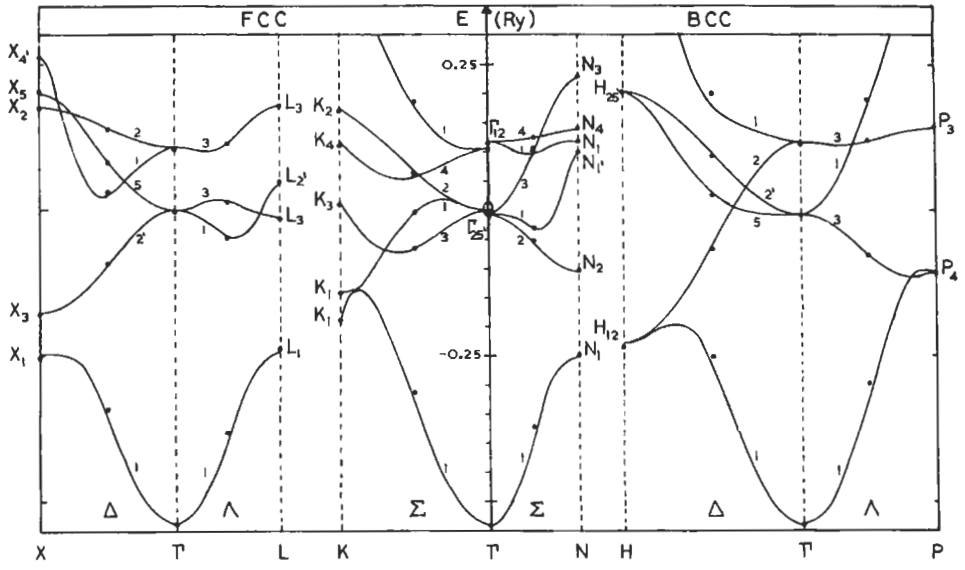

Fig. 25. The H–NFE–TB band structure of fcc and bcc iron in the nonmagnetic state. The solid circles represent the first-principle energy levels of WOOD [1962]. (From PETTIFOR [1970a].)

calculations (see, e.g., RATH and CALLAWAY [1973], JEPSEN *et al.* [1975], MORUZZI *et al.* [1978], PAXTON *et al.* [1990]) because they allow a direct comparison between the bcc, fcc and hcp densities of states for the *same* model element. This will be important when discussing the relative stability of the three different crystal structures in § 6.1 and the stability of the ferromagnetic state in the α, γ and ε phases of iron in § 8.

The structure in the *calculated* densities of states in fig. 26 is reflected in the behaviour of the *experimental* electronic heat constant, γ, across the nonmagnetic 4d and 5d transition metal series. It follows from eqs. (45), (47) and (48) that the electronic heat capacity may be written as

$$C = \gamma T, \tag{100}$$

where

$$\gamma = \tfrac{1}{3}\pi^2 k_B^2 n(E_F). \tag{101}$$

Therefore, ignoring any renormalization effects such as electron–phonon mass enhancement, the linear dependence of the heat capacity gives a direct experimental measure of the density of states at the Fermi level. Figure 27 shows that the H–NFE–TB densities of states in fig. 26 reflect the experimental variation in γ across the series.

4.3. Volume dependence

Figure 28 illustrates the volume dependence of the energy bands of the 4d transition metals Y, Tc and Ag, which were calculated by PETTIFOR [1977] within the atomic–

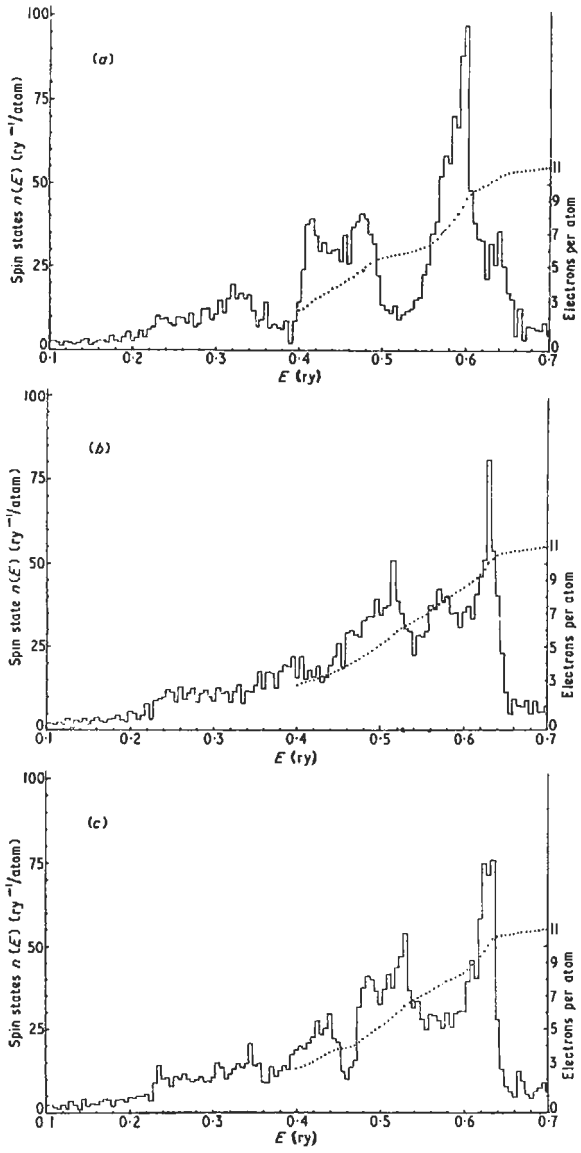

Fig. 26. The density of states for the three structures (a) bcc, (b) fcc, and (c) hcp for a model transition metal. The dotted curves represent the integrated density of states. (From PETTIFOR [1970b].)

sphere approximation of ANDERSEN [1973, 1975]. Similar bands have been obtained by GELATT *et al.* [1977] for the 3d metals Ti and Cu with the renormalized-atom approximation of WATSON *et al.* [1970]. We see from fig. 28 that the bottom of the NFE sp band Γ_1, which was evaluated within LDF theory, is well fitted by the Frohlich–Bardeen expression (79). The values of R_c obtained are found to scale *within 1%* with the position of the outer node of the 5s free-atom radial wave function. This demonstrates quantitat-

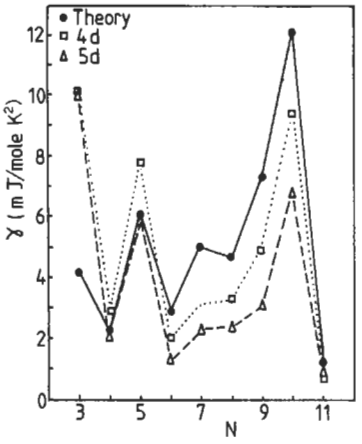

Fig. 27. A comparison of the theoretical and experimental 4d and 5d heat capacities. The theoretical values were obtained directly from eq. (101) and fig. 26, neglecting any changes in the density of states due to band width changes or mass renormalization.

ively that it is the core-orthogonality constraint which is responsible for the rapid turn up in the energy of Γ_1 and that the outer node of the valence s electron is a good measure of the s core size. The free-atom d level broadens into a band of states of width W as the atoms come together from infinity to form the bulk (see figs. 24 and 28). HEINE [1967] has shown that the Wigner–Seitz boundary conditions imply that W should vary approximately as S^{-5}, where S is the Wigner–Seitz radius. Assuming a power-law dependence of W on S, we can write

$$W = W_0(S_0/S)^n, \tag{102}$$

where W_0 and S_0 are the values of the d-band width and Wigner–Seitz radius respectively at the equilibrium lattice spacing of the transition metal. Table 1 gives the values of S_0, W_0 and n for the 4d transition metals (PETTIFOR [1977]). Because of the more extended nature of the d wave functions at the beginning of the transition metal series, n takes a value closer to four than to five which we will see in § 5.2 is reflected in their bulk properties. Values of the band width W for the 3d, 4d and 5d series may be obtained from the table in ANDERSEN and JEPSEN [1977] and are given explicitly in table 20–4 of HARRISON [1980]. The 3d and 5d band widths are approximately 30% smaller and 20% larger respectively than the corresponding 4d widths.

The centre of gravity of the TB-d band, E_d, in fig. 28 rises *exponentially* (PETTIFOR [1977]) as the volume decreases because the potential within the Wigner–Seitz sphere *renormalizes* due to the increase in the electronic charge density (GELATT *et al.* [1977]). This renormalization in position of the free atomic d level plays an important role in transition-metal energetics and will be discussed further in § 5.2.

The different volume dependences of the NFE-sp and TB-d bands displayed in fig. 28 will lead to changes in the relative occupancy of the two bands with volume. This is illustrated in fig. 4 of PETTIFOR [1977] where Y and Zr show a rapid increase in d-band occupancy under compression as the d band widens and the bottom of the sp band moves

Table 1
Equilibrium values of Wigner-Seitz radius S_0 and d band parameters W, n and n/S_0 for 4d series (from PETTIFOR [1977]).

Quantity	Element								
	Y	Zr	Nb	Mo	Tc	Ru	Rh	Pd	Ag
S_0 (au)	3.76	3.35	3.07	2.93	2.84	2.79	2.81	2.87	3.02
W_0 (eV)	6.3	7.8	9.3	9.5	9.1	8.5	7.6	6.0	3.9
n	3.9	4.0	4.1	4.3	4.5	4.6	4.8	5.1	5.6
n/S_0	1.03	1.19	1.33	1.47	1.58	1.65	1.71	1.77	1.84

up (cf. fig. 28a). Eventually Γ_1 moves up through the Fermi level E_F at which point all the NFE-sp states have been emptied into the TB-d states and $N_d = N$. On the other hand, the transition metals with more-than-half-filled d bands display a marked degree of constancy in N_d for volumes about their *equilibrium* values, because the sp core effects are largely counter-balanced by the rapid rise in E_d due to the increasing coulomb repulsion between the d electrons (cf. fig. 28c). However, under very high pressures the bottom of the sp band does eventually move up through the Fermi level, and transition metals with *ten* valence electrons (Ni, Pd and Pt) may become semiconducting (MCMAHAN and ALBERS [1982]). We will return to this dependency of the d-band occupancy on volume and core size when discussing crystal structure stability in § 6.

5. *Bulk properties*

5.1. Simple metals

Within the *free-electron* approximation the total energy per electron may be written (see, e.g., HEINE and WEAIRE [1970]) as:

$$U_{eg} = 2.21/r_s^2 - 0.916/r_s - (0.115 - 0.0313 \ln r_s), \tag{103}$$

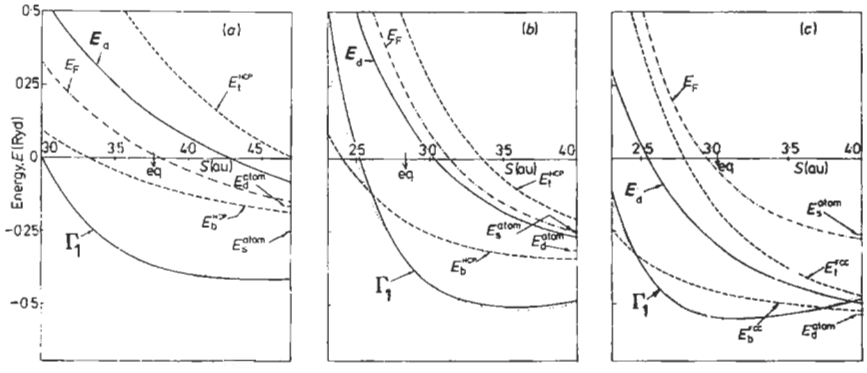

Fig. 28. The energy bands as a function of Wigner–Seitz radius S for (a) Y, (b) Tc, and (c) Ag. The observed equilibrium Wigner–Seitz radii are marked eq. The dotted curve gives the Fröhlich–Bardeen fit (eq. 79) to the bottom of the conduction band Γ_1. E_d, E_t and E_b mark the centre of gravity, and top and bottom of the d band, respectively. (After PETTIFOR [1977].)

where r_s is the radius of the sphere which contains one electron so that

$$r_s = Z^{-1/3} S \tag{104}$$

for a metal with valence Z and Wigner–Seitz radius S. The first term in eq. (103) is the average *kinetic* energy of a free electron gas, namely $\frac{3}{5} E_F$, where E_F is given by eq. (45). The second term is the *exchange* energy which is attractive, because parallel-spin electrons are kept apart by Pauli's exclusion principle, thereby leading to weaker mutual coulomb repulsion. The third term is the *correlation* energy which gives the additional lowering in energy due to the dynamical correlations between the electrons. It follows from eq. (103) that the free electron gas is in equilibrium for $r_s = 4.2$ au with a binding energy per electron of 0.16 Ry or 2.2 eV.

If the electron gas is perturbed to *first order* by the presence of the ionic lattice (HEINE and WEAIRE [1970], GIRIFALCO [1976] and HARRISON [1980]), then the total binding energy *per atom* may be written as:

$$U = Z\left(U_{eg} + U_{ion}\right), \tag{105}$$

where

$$U_{ion} = -\frac{3Z}{S}\left[1 - \left(\frac{R_c}{S}\right)^2\right] + \frac{1.2Z}{S}. \tag{106}$$

The first and second terms in eq. (106) give the electron–ion [cf. eq. (79)] and the electron–electron potential energies, respectively. The potential energy has been evaluated within the WIGNER–SEITZ [1933] approximation of neglecting the coulomb interaction between different Wigner–Seitz cells as they are electrically neutral. Within the free-electron approximation the ion cores had been smeared out into a uniform positive background so that there was zero net potential energy and U_{ion} vanished.

The equilibrium Wigner–Seitz radius, S_0, which is found from eq. (105) by requiring that U is stationary, depends explicitly on the core radius R_c through the equation

$$\left(\frac{R_c}{S_0}\right)^2 = \tfrac{1}{5} + \frac{0.102}{Z^{2/3}} + \frac{0.0035 S_0}{Z} - \frac{0.491}{Z^{1/3} S_0}, \tag{107}$$

where the first four terms are coulomb, exchange, correlation and kinetic contributions respectively. GIRIFALCO [1976] has taken the experimental values of the Wigner–Seitz radius S_0 to determine an effective Ashcroft empty-core radius R_c from eq. (107). The resultant values are given in table 2 where, as expected, the core size increases as one goes down a given group in the Periodic Table. It is clear from table 2 that only sodium has an equilibrium value of r_s that is close to the free-electron-gas value of 4.2 au.

The bulk modulus (or inverse compressibility), which is defined by

$$B = V\left(\mathrm{d}^2 U / \mathrm{d}V^2\right), \tag{108}$$

may be written from eqs. (105) and (107) in the form

$$B/B_{ke} = 0.200 + 0.815 R_c^{\,2}/r_s \tag{109}$$

Table 2
Equilibrium bulk properties of the simple and noble metals.

Metal	Quantity						
	Z	U_{coh}/Z (eV/electron)	S_0 [a] (au)	r_s [a] (au)	R_c (au)	B/B_{ke} (eq. 109)	B/B_{ke} (expt.)
Li	1	1.7	3.27	3.27	1.32	0.63	0.50
Na	1	1.1	3.99	3.99	1.75	0.83	0.80
K	1	0.9	4.86	4.86	2.22	1.03	1.10
Rb	1	0.9	5.31	5.31	2.47	1.14	1.55
Cs	1	0.8	5.70	5.70	2.76	1.29	1.43
Be	2	1.7	2.36	1.87	0.76	0.45	0.27
Mg	2	0.8	3.35	2.66	1.31	0.73	0.54
Ca	2	0.9	4.12	3.27	1.73	0.95	0.66
Sr	2	0.9	4.49	3.57	1.93	1.05	0.78
Ba	2	0.9	4.67	3.71	2.03	1.11	0.84
Zn	2	0.7	2.91	2.31	1.07	0.60	0.45
Cd	2	0.6	3.26	2.59	1.27	0.71	0.63
Hg	2	0.3	3.35	2.66	1.31	0.73	0.59
Al	3	1.1	2.99	2.07	1.11	0.69	0.32
Ga	3	0.9	3.16	2.19	1.20	0.74	0.33
In	3	0.9	3.48	2.41	1.37	0.83	0.39
Tl	3	0.6	3.58	2.49	1.43	0.87	0.39
Cu	1	3.5	2.67	2.67	0.91	0.45	2.16
Ag	1	3.0	3.02	3.02	1.37	0.71	2.94
Au	1	3.8	3.01	3.01	1.35	0.69	4.96

[a] From GIRIFALCO [1976].

at equilibrium, where the correlation contribution has been neglected since it contributes less than a few percent. B_{ke} is the bulk modulus of the non-interacting free electron gas, namely

$$B_{ke} = 0.586/r_s^5. \tag{110}$$

It follows from eq. (109) and table 2 that the presence of the ion core is crucial for obtaining realistic values of the bulk modulus of simple metals, as was first demonstrated by ASHCROFT and LANGRETH [1967]. However, the simple *first*-order expression eq. (109) is leading to large errors for the polyvalent metals with valence greater than two because the *second*-order contribution is not negligible and must be included (ASHCROFT and LANGRETH [1967]). Table 2 also demonstrates that the noble metals are not describable by the NFE approximation, the theoretical bulk moduli being a factor of five too small. We will return to this point in § 5.2.

The *cohesive* energy of the simple metals is observed in table 2 to be about 1 eV *per valence electron*. For example, Na, Mg and Al have cohesive energies of 1.1, 0.8 and 1.1 eV per electron respectively. These are an order of magnitude smaller than the corresponding *binding* energies given by eq. (105), the experimental values being 6.3, 12.1, and 18.8 eV per electron respectively. Although NFE perturbation theory can yield good estimates of *bulk* properties such as the equilibrium atomic volume, structural stability

and heat of formation, it can not provide reliable cohesive energies which require an accurate comparison with the *free* atom whose wave functions are not describable by weakly perturbed plane waves. It is necessary, therefore, to perform *similar* calculations in both the free atom and the bulk as, for example, WIGNER and SEITZ [1933] and MORUZZI *et al.* [1978] have done in their evaluation of the cohesive energies in figs. 21 and 1 respectively. We should point out, however, that eqs. (103)–(106) do yield a *bulk* binding energy for sodium that is very similar to Wigner and Seitz's [cf. eq. (82)], because the additional exchange, correlation and self-energy terms in eqs. (105) and (106) give a net contribution of less than 0.01 eV per sodium atom. CHELIKOWSKY [1981] has linked the cohesive energy of simple metals to a kinetic-energy change which accompanies the transformation of the exponentially damped free-atom wave function to plane-wave bulk states. As expected from table 2 and fig. 20, it is necessary to include an additional *non-local* bulk bonding contribution in order to obtain the stronger cohesion of Li and Be and the weaker cohesion of Zn, Cd and Hg. The anomalously large cohesion of the noble metals Cu, Ag and Au will be discussed in the next subsection.

5.2. Transition metals

The theoretical points in fig. 1 were computed (MORUZZI *et al.* [1978]) by solving the Schrödinger equation (1) with the potential $v(r)$ given by

$$v(r) = v_H(r) + v_{XC}(r), \tag{111}$$

where v_H is the usual Hartree potential and v_{XC} is the exchange-correlation potential evaluated within the local density functional (LDF) approximation of HOHENBERG and KOHN [1964] and KOHN and SHAM [1965], namely

$$v_{XC}(r) = \frac{d}{d\rho}\left(\rho\varepsilon_{XC}(\rho)\right). \tag{112}$$

$\varepsilon_{XC}(\rho)$ is the exchange and correlation energy per electron of a homogeneous electron gas of density ρ. It follows from eqs. (103) and (112) that the *exchange* contribution to the potential may be written as:

$$v_X(r) = \tfrac{3}{4}\,\varepsilon_X(r), \tag{113}$$

where

$$\varepsilon_X(r) = -1.477\left[\rho(r)\right]^{1/3}. \tag{114}$$

Thus the exchange potential varies as the third power of the *local* density, due to the exclusion of parallel spin electrons from the immediate neighbourhood (SLATER [1951b]).

The total energy can *not* be written simply as the sum over the occupied one-electron energies E_i of the Schrödinger equation, because the eigenvalue E_i of the ith electron contains the potential energy of interaction with the jth electron and vice versa. Thus, $E_i + E_j$ *double-counts* the coulomb interaction energy between electrons i and j. The total LDF energy is, therefore, given by

$$U = \sum_i E_i - \tfrac{1}{2}\iint \frac{2\rho(r)\rho(' r')}{|r - r'|}\,dr dr' - \int \rho(r)[v_{XC} - \varepsilon_{XC}]dr, \tag{115}$$

where the second and third contributions correct for the "double-counting" of the coulomb and exchange-correlation energies respectively. The potential energy has been written down in eq. (115) within the Wigner–Seitz sphere approximation, the coulomb interaction between neighbouring Wigner–Seitz cells, or Madelung contribution, being neglected. (Note that $e^2 = 2$ in atomic units, which accounts for the factor of two in the integrand of the coulomb integral.)

The presence of the double-counting contribution in eq. (115) does not allow for a direct interpretation of the *total* energy in terms of the one-electron eigenvalues E_i whose behaviour we have studied in the previous sections. For example, as can be seen from fig. 28b the one-electron sum alone would lead to no binding in Tc because the d-electron eigenvalues at the equilibrium atomic volume are everywhere higher than the free-atom d level. The inclusion of the double-counting term is crucial for bonding since it counters to a large extent the shift in the centre of gravity of the d bands E_d due to the *renormalization* of the potential under volume change. In copper, for example, GELATT *et al.* [1977] found that the band-shift energy of 78.6 eV/atom, which accompanies the formation of the bulk metal, is almost totally cancelled by a change in the double-counting term of 77.7 eV/atom. The remaining net repulsive contribution of about 1 eV/atom is typical for the 3d and 4d transition metal series (see fig. 4 of GELATT *et al.* [1977]).

The problems associated with double-counting can be avoided, however, by working not with the total energy, U, but with *the first-order change* in energy, δU, on change in the Wigner–Seitz sphere volume, $\delta\Omega$, for the bulk metal (PETTIFOR [1976]) or change in the internuclear separation, δR, for the diatomic molecule (PETTIFOR [1978a]). By starting either from the virial theorem in the form derived by LIBERMAN [1971] or from the total-energy expression (115) following NIEMINEN and HODGES [1976], PETTIFOR [1976, 1978a] showed that the first-order change in *total energy*, δU, may be written, neglecting the Madelung contribution, as:

$$\delta U = \sum_i \delta E_i, \tag{116}$$

where δE_i is the first-order change in the *eigenvalue* which accompanies the first-order volume or distance change *while the potential is kept unrenormalized.* The *general* applicability of this first-order result has been proved by ANDERSEN [1980] for force problems involving arbitrary atomic displacements and by NORSKOV [1982] for embedding problems involving a change in the local atomic environment (cf. § 7). SKRIVER [1982], MCMAHAN and MORIARTY [1983] and PAXTON and PETTIFOR [1992] have demonstrated the applicability of eq. (116) to the evaluation of structural energy differences (cf. § 6).

The first-order expression (116) is important because it allows a direct identification of the different roles played by the valence sp and d electrons in bulk transition metal energetics. The eigenstates can be decomposed within the Wigner–Seitz sphere into their different angular momentum components, l, so that eq. (116) may be written as:

$$\delta U = -P\delta\Omega = -\sum_l P_l \delta\Omega, \tag{117}$$

where P is the pressure, given by $P = -\,\mathrm{d}U/\mathrm{d}\Omega$. By working within the atomic-sphere approximation of ANDERSEN [1973] the *partial pressures* P_l may be expressed (PETTIFOR [1976]) directly in terms of parameters describing the energy bands, namely:

$$3P_{sp}\Omega = 3N_{sp}\left(\Gamma_1 - \varepsilon_{xc}\right) + 2U_{sp}^{ke}, \tag{118}$$

$$3P_d\Omega = 2N_d\left(E_d - \varepsilon_{xc}\right)/m_d + 5U_d^{bond}, \tag{119}$$

where

$$U_{sp}^{ke} = \int^{E_F} \left(E - \Gamma_1\right) n_{sp}(E)\mathrm{d}E, \tag{120}$$

$$U_d^{bond} = \int^{E_F} \left(E - E_d\right) n_d(E)\mathrm{d}E, \tag{121}$$

with $\varepsilon_{XC} = \varepsilon_{XC}(S)$. m_d is the d-band effective mass which is related to the width W through $W = 25/(m_d S^2)$. Additional small contributions to eqs. (118) and (119) have been neglected for simplicity in the present discussion (cf. eqs. (13) and (14) of PETTIFOR [1978b]).

The sp partial pressure consists of two terms which give the first-order changes in the *bottom* of the sp band, Γ_1, and in the *kinetic* energy, respectively. In the absence of hybridization with the d band, $n_{sp}(E)$ is free-electron-like and eq. (118) is consistent with the pressure which would be obtained from the simple-metal expression (105) if correlation is neglected. This follows from eqs. (111), (113) and (79) because within LDF theory the bottom of the band is given by

$$\Gamma_1 = \Gamma_1^{WS} + 2.4\,Z/S + \tfrac{4}{3}\varepsilon_X \tag{122}$$

since the electron sees the average Hartree field of the valence electrons and the exchange potential v_X in addition to the ion core pseudopotential.

The d partial pressure also consists of two terms which give the first-order changes in the *centre of gravity* of the d band, E_d, and the d *bond* energy, respectively. In the absence of hybridization we may assume that $n_d(E)$ is rectangular as illustrated in fig. 24, so that from eq. (121) the d bond energy may be written

$$U_d^{bond} = -\tfrac{1}{20} W N_d\left(10 - N_d\right). \tag{123}$$

Assuming that $E_d - E_d^{atom}$ and W vary inversely as the fifth power of S, P_d may be integrated with respect to volume to give the d contribution to the *cohesive* energy, namely:

$$U_d = N_d\left(E_d - E_d^{atom}\right)/4m_d + N_d\left(\tfrac{4}{3}E_d^{atom} - \varepsilon_{xc}\right)/2m_d + U_d^{bond}. \tag{124}$$

It follows from fig. 28a that for Tc at its equilibrium volume $E_d - E_d^{atom} = 6$ eV, $\frac{4}{3}E_d^{atom} - \varepsilon_{XC} = 1$ eV and $m_d = 5$. Therefore, taking, from table 2, $W = 10$ eV and $N_d = 6$, we have

$$U_d = 1.8 + 0.6 - 12 = -10\text{eV/atom}, \tag{125}$$

which is in reasonable agreement with the LDF value of -8 eV/atom for the Tc cohesive energy in fig. 1.

The dominant contribution to the *cohesive energy* of transition metals is, therefore, the d bond term in eq. (125) as emphasized by FRIEDEL [1964, 1969] and illustrated by GELATT *et al.* [1977] in their fig. 4. From eq. (123) it varies parabolically with band filling and accounts for the observed variation of the cohesive energy across the *nonmagnetic* 4d and Sd series shown in fig. 1. It attains a maximum value of $-5\ W/4$ for $N_d = 5$ when all the bonding and none of the antibonding states are occupied. Equation (124) shows that the shift in centre of gravity of the d band contribution $N_d(E_d - E_d^{atom})$ is reduced by at least an order of magnitude through the factor $(4m_d)^{-1}$, thereby accounting *analytically* for the cancellation arising from the double-counting term in eq. (115).

Figure 29 shows the sp and d partial pressures for Tc. As expected from eq. (123) there is a large *attractive* d bond contribution which is pulling the atoms together in order to maximize the strength of the bond. This is opposed for $S < 4.0$ au by a rapidly increasing *repulsive* d centre-of-gravity contribution which reflects the renormalization in E_d. The resulting total d partial pressure is *attractive* at the observed equilibrium volume of Tc (see fig. 29b). As expected from the behaviour of Γ_1 in fig. 28b the bottom of the sp band contribution is attractive for large values of S but becomes repulsive in the vicinity of the equilibrium volume as Γ_1 moves up in energy. Thus, whereas in simple metals this contribution is attractive because the ion cores occupy only about 10% of the atomic volume (see fig. 21 and table 3), in transition metals it is repulsive because

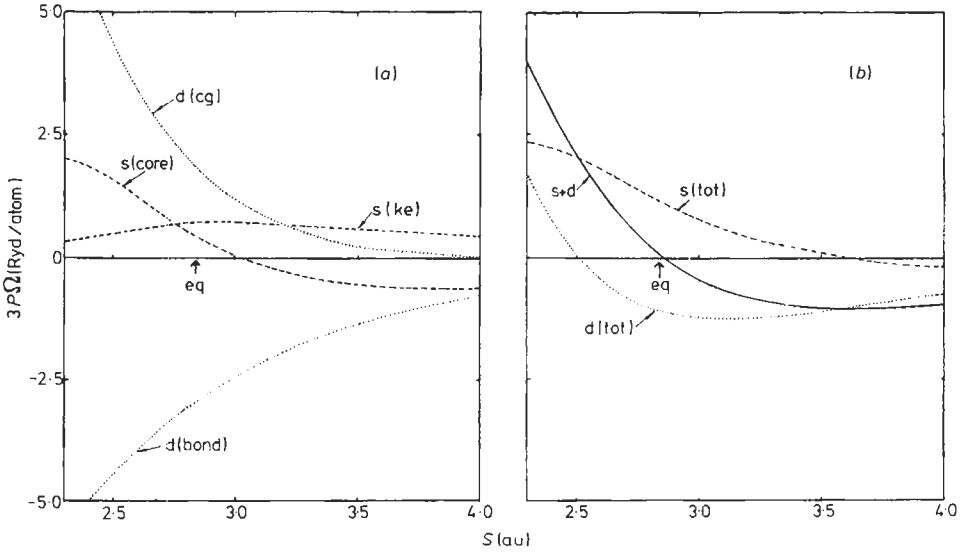

Fig. 29. (a) The *individual* and (b) the *total* sp and d partial pressures as a function of the Wigner-Seitz radius S for T_c. "eq" marks the observed equilibrium Wigner–Seitz radius. (From PETTIFOR [1978b]).

Table 3
The values of λ for the 3d, 4d, and 5d transition metal series.

Period	Element and value of λ (in au^{-1})							
	Sc	Ti	V	Cr	Mn	Fe	Co	Ni
3	1.08	1.23	1.37	1.49	1.61	1.74	1.88	2.07
	Y	Zr	Nb	Mo	Tc	Ru	Rh	Pd
4	1.08	1.23	1.37	1.49	1.60	1.72	1.85	2.02
	Lu	Hf	Ta	W	Re	Os	Ir	Pt
5	1.11	1.25	1.38	1.49	1.60	1.72	1.84	2.01

the ion cores occupy a much larger percentage due to their smaller equilibrium atomic volumes (cf. fig. 1). Together with the sp kinetic energy contribution, the bottom of the sp band contribution provides the necessary repulsion to counter the attractive d partial pressure at equilibrium.

The *size* of a transition-metal atom, which is defined by the equilibrium atomic volume of the pure metal, is not necessarily a helpful quantity for discussing alloy energetics. We have seen that it will be very sensitive to the nature of the local atomic environment, since it is the d bond contribution which is responsible in fig. 1 for the skewed parabolic behaviour of the equilibrium Wigner–Seitz radius across the nonmagnetic 4d series. This may be demonstrated by modifying the simple model of DUCASTELLE [1970] and approximating the total energy of a transition metal by

$$U = U^{\text{rep}} + U_{\text{d}}^{\text{bond}}, \tag{126}$$

where the Born–Mayer contribution, U^{rep}, is:

$$U^{\text{rep}} = aN^2 e^{-2\lambda S} \tag{127}$$

with a being constant across a given series. This form is suggested by the nature of the repulsive d centre-of-gravity contribution in eq. (124) and fig. 29, although we have assumed that U^{rep} is proportional to N^2 rather than N_{d}^2 as a reminder that the sp electrons also contribute to the repulsion. The d bond contribution, eq. (123), is proportional to the band width W which is assumed to vary exponentially as

$$W = b\lambda^2 e^{-\lambda S} \tag{128}$$

with b being constant across a given series.

The cohesive energy, equilibrium Wigner–Seitz radius and bulk modulus are given from eqs. (126)–(128) by:

$$U_{\text{coh}} = \tfrac{1}{2} U_{\text{d}}^{\text{bond}}, \tag{129}$$

$$S_0 \left[\ln\left(-2aN^2 / U_{\text{d}}^{\text{bond}}\right) \right] / 2\lambda, \tag{130}$$

$$B = -\left(\lambda^2 / 12\pi S_0\right) U_{\text{d}}^{\text{bond}}. \tag{131}$$

a and b for a given period are obtained from the known bulk modulus and band width of 3d Cr, 4d Mo and 5d W, the values of *(a, b)* being given in atomic units by (24.3, 11.6), (77.2, 25.8) and (98.9, 31.9) respectively. λ is found by fitting to the *nonmagnetic* Wigner–Seitz radius, assuming that the transition metals have only one sp valence electron. We see from fig. 30 and table 3 that although the equilibrium atomic volume has a minimum in the vicinity of $N=8$, λ varies nearly *linearly* across the series as expected for a parameter characterizing the free atom (cf. figs. 4, 5 and 7). Thus, although Mo and Ag have almost the same size factors with their equilibrium Wigner–Seitz radii of 2.93 and 3.02 au, respectively, they are immiscible because Mo will lose a large part of its attractive d bond contribution in a Ag environment. The logarithmic derivative of the band width, $-\lambda$, predicted by this model is in good agreement at the equilibrium atomic volume with the first-principles value, $-n/S_0$, as can be seen by comparing tables 1 and 3 for the 4d series.

The simple model breaks down at the noble-metal end of the series because the Born–Mayer repulsive term in eq. (126) does not describe correctly the d electron behaviour. This can be seen in fig. 31 where the d partial pressure in Cu *is attractive* at the equilibrium atomic volume, the d electrons contributing about 25% to the cohesive energy (WILLIAMS *et al.* [1980a]). Thus, as first pointed out by KOLLAR and SOLT [1974], the filled d shells in copper interact attractively rather than repulsively as assumed by the Born-Mayer contribution (127). This is due to the second term in eq. (124) which dominates at larger atomic volumes. The sp partial pressure of Cu at its minimum is also more attractive than that of K due to the incomplete screening of the Cu ion core by the 3d valence electrons. The net result is that whereas the simple metal K has a cohesive energy of 0.9 eV/atom and a bulk modulus of 0.3×10^{10} N/m^2, the noble metal Cu has a cohesive energy of 3.5 eV/atom and a bulk modulus of 13.7×10^{10} N/m^2, which is reflected by the behaviour of the curves in fig. 31.

6. *Structural stability*

6.1. Elemental metals

The crystal structure of the *simple* metals can be studied (see, e.g., HARRISON [1966], HEINE and WEAIRE [1970], HAFNER [1974, 1989] and MORIARTY [1982, 1983 and 1988]) by perturbing the free electron gas to *second* order in the pseudopotential, thereby extending the first-order expression (105) considered in § 5.1. The resulting binding energy per atom is given in the real-space representation (FINNIS [1974]) by

$$U = ZU_{e\xi} - \tfrac{1}{2} V\mathrm{ic}_{eg}^{-1} + \tfrac{1}{2}\phi(\boldsymbol{R}=0; r_s) + \tfrac{1}{2}\sum_{\boldsymbol{R}\neq 0}\phi(\boldsymbol{R}; r_s), \tag{132}$$

where κ_{eg} is the compressibility of the free electron gas. $\phi(\boldsymbol{R}=0;\ r_s)$ represents the electrostatic interaction between an ion and its own screening cloud of electrons, whereas $\phi(\boldsymbol{R}\neq 0;\ r_s)$ is a *central* interatomic pair potential which for a local pseudopotential may be written as:

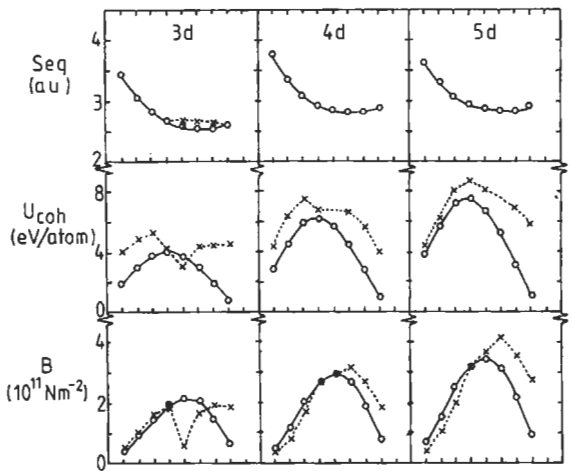

Fig. 30. The theoretical (open circles) and experimental (crosses) values of the equilibrium Wigner-Seitz radius, cohesive energy, and bulk modulus of the 3d, 4d, and 5d transition metals.

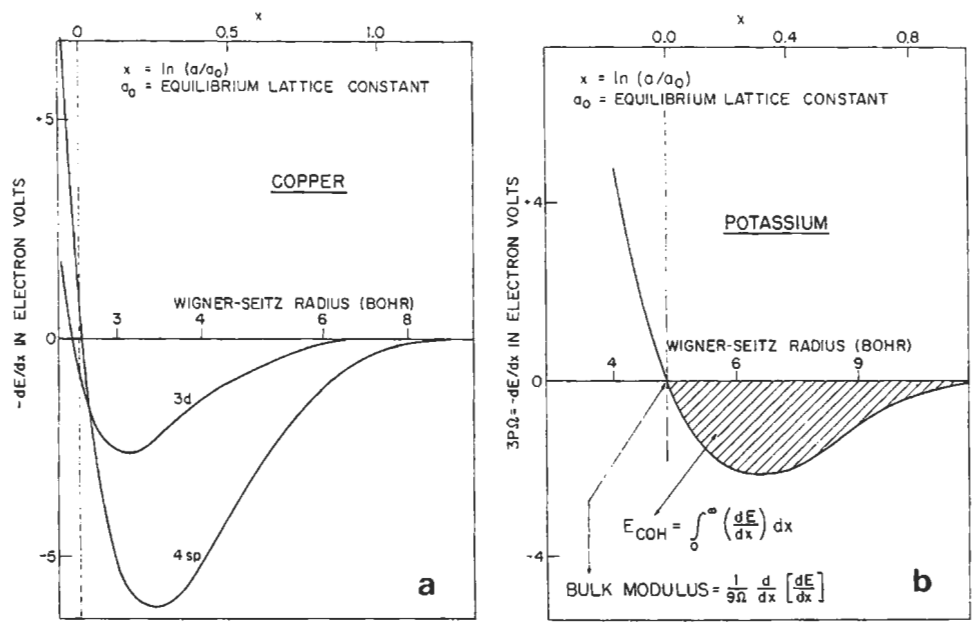

Fig. 31. (a) The sp and d partial pressures for Cu and (b) the sp pressure for K as a function of the Wigner–Seitz radius. The independent variable x is the logarithm of the ratio of the lattice constant a (or Wigner-Seitz radius S) to its equilibrium value a_0 (or S_0), so that equilibrium corresponds to the zero value of x on the upper horizontal axis. The cohesive energy associated with a given pressure curve is the area between the curve and the axis, as illustrated in (b). (From WILLIAMS *et al.* [1980a].)

$$\phi(\boldsymbol{R} \neq 0; r_s) = \frac{2Z^2}{R}\left[1 - \tfrac{2}{\pi}\int_0^\infty \chi(q, r_s)\left[\hat{v}_{ps}^{ion}(q)\right]^2 \frac{\sin qR}{q}\,dq\right]. \tag{133}$$

$\hat{v}_{ps}^{ion}(q)$ is proportional to the Fourier component of the ionic pseudopotential, taking the value $\cos qR_C$ for the Ashcroft potential [cf. eq. (76)]. $\chi(q, r_s)$ is the free-electron-gas response function which screens the ion cores (see, e.g., JACUCCI and TAYLOR [1981]). The first term in eq. (133) gives the direct ion–ion coulomb repulsion, the second the attractive ion–electron contribution.

The interatomic potential (133) may be expressed analytically (PETTIFOR [1982]) at metallic densities as the sum of damped oscillatory terms, namely

$$\phi(\boldsymbol{R} \neq 0; r_s) = (2Z^2/R)\sum_n A_n \cos(2k_n R + \alpha_n)e^{-\kappa_n R}, \tag{134}$$

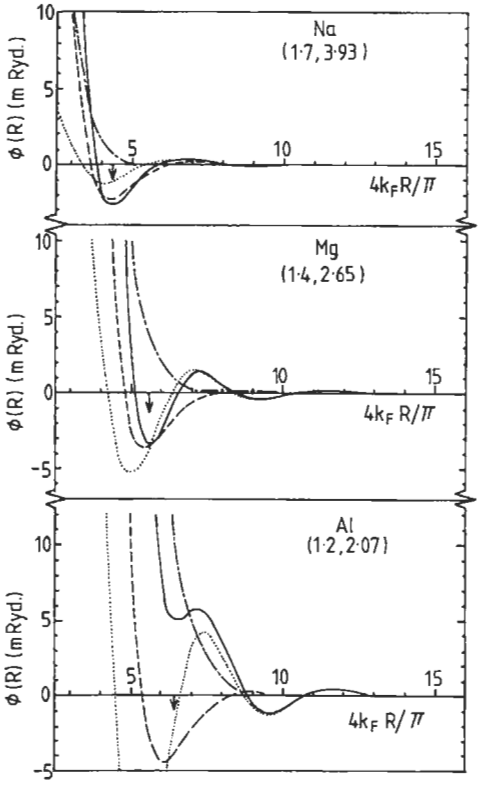

Fig. 32. The analytic pair potential (solid curve) for Na, Mg, and Al, the three individual contributions being given by the dotted–dashed, dashed, and dotted curves respectively. The arrows mark the position of the twelve nearest neighbours in the close-packed fcc and hcp lattices. The values of R_c and r_s are written (R_c, r_s) for each element. (After PETTIFOR and WARD [1984].)

where k_n and κ_n depend only on the density of the free electron gas through r_s, whereas the amplitude A_n and the phase α_n depend also on the ionic pseudopotential (through R_c). The interatomic potentials for Na, Mg and Al are illustrated in fig. 32, where the first three terms in eq. (134) have been retained and an Ashcroft empty-core pseudopotential used (PETTIFOR and WARD [1984]). We see that all three metals are characterized by a repulsive hard-core contribution (dotted–dashed curve), an attractive nearest-neighbour contribution (dashed curve), and an oscillatory long-range contribution (dotted curve). For *very large* interatomic separations the pair potential behaves asymptotically (FRIEDEL [1952]) as

$$\phi(R \neq 0; r_s) \sim A\left[v_{ps}(2k_F)\right]^2 \cos(2k_F R)/R^3, \tag{135}$$

where from eqs. (44) and (104) $k_F = (9\pi/4)^{1/3}/r_s$.

A cautionary note must be sounded concerning the use of interatomic pair potentials for describing the energetics of simple metals. It is clear from fig. 32 that the pair-potential contribution to the binding energy of sodium and magnesium is only about 0.25 eV/atom, which is small compared to their cohesive energies of 1.1 and 1.6 eV/atom, respectively. Moreover, in aluminium the pair contribution acts *against* cohesion. Thus, there is no microscopic justification for describing the bonding in simple metals by pair potentials alone. Their cohesion is determined primarily by the *volume*-dependent terms in eq. (132). However, the pair potential description is valid for tackling problems concerned with *structural* rearrangement in which the volume remains fixed, for example in lattice dynamics or in determining the relative stability of the close- or nearly close-packed fcc, hcp and bcc lattices.

Figure 33 compares the stability of the fcc, hcp and bcc lattices of Na, Mg and Al as their volume is reduced from the equilibrium value by nearly an order of magnitude, which was computed by MORIARTY and MCMAHAN [1982] using a generalized non-local pseudopotential to second order. We see that under pressure Na, Mg and Al are predicted to transform from hcp → bcc → hcp, hcp → bcc → fcc and fcc → hcp → bcc, respectively. The first of these structural transitions occurs at about 1, 57 and 130 GPA for Na, Mg and Al respectively and should, therefore, be verifiable by modern high-pressure technology. The trends displayed in fig. 33 may be understood from the behaviour of the first three contributions to the pair potential in fig. 32 (PETTIFOR and WARD [1984]; see

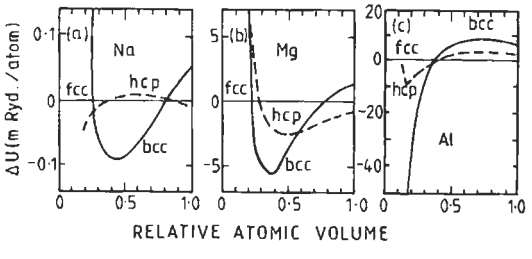

Fig 33. The energy of the bcc and hcp lattices with respect to the fcc lattice for Na, Mg, and Al as a function of their atomic volume relative to the observed equilibrium volumes (after MORIARTY and MCMAHAN [1982]).

also McMAHAN and MORIARTY [1983]). Because the close-packed structures fcc and hcp have identical first and second nearest-neighbour distances their relative stability is determined by the position of their next few neighbours with respect to the long-range oscillatory tail which is drawn dotted in fig. 32. Since the phase α_3 of this contribution depends on r_s, under pressure the minima shift with respect to the neighbour positions and the close-packed phases can reverse their relative stability. On the other hand, the competition between the close-packed phases and bcc is determined primarily by the contribution from the twelve first nearest neighbours and fourteen first and second nearest neighbours respectively. Although at their equilibrium volume the first twelve close-packed neighbours fall at the minimum of the pair potential, thereby favouring the close-packed structures (cf. fig. 32), under pressure this minimum moves and the bcc phase may be stabilized (cf. fig. 33).

The *close-packed* metallic behaviour of Na, Mg and Al gives way to the *open* diamond structure of the semiconductor Si as one proceeds *across* the third row of the Periodic Table. This transition from close-packed to open structure is accompanied by a 30% volume expansion so that the volume-dependent term in the binding energy cannot be neglected when determining structural stability. YIN and COHEN [1980] have solved the Schrödinger equation self-consistently for Si using an ionic pseudopotential, and have evaluated the LDF binding energy [cf. eq. (115)] as a function of volume for seven different crystal structures as illustrated in fig. 34a. They find that the diamond structure has the lowest energy with a predicted equilibrium atomic volume, cohesive energy and bulk modulus within 5% of the experimental values. Moreover, the relative ordering of the metallic bcc and hcp phases and their equilibrium energy of about 0.5 eV/atom with respect to the diamond structure is in good agreement with that deduced from experiment (KAUFMAN and NESOR [1973]). The transition to the open semiconducting phase, therefore, contributes about 10% to the total cohesive energy of 4.6 eV/atom.

In moving *down* group IV we see from figs. 4 and 7 that Ge is very similar to Si with about a 10% larger core, whereas Sn and Pb have approximately 30% and 45% larger cores respectively. Thus the binding–energy–volume curves of Ge are found to be almost identical to those of Si except that the close-packed structures move down relative to the diamond structure by about 20% (compare figs. 34a and b; YIN and COHEN [1980, 1981]). The further increase in core size in going from Ge to Sn is probably responsible for the β-Sn structure being stabilized under only 2 GPA of pressure and the still much larger core of Pb at the bottom of group IV leads to the close-packed fcc structure being most stable. The structural trends across the sp-valent elements within the periodic table has recently been discussed by CRESSONI and PETTIFOR [1991] using the Tight Binding approximation.

The crystal structure of the *transition* metals can be understood by comparing the d bond contribution eq. (121) to the total energy, because we saw in § 5.2 that it dominates the cohesive energy. Figure 35 shows that as the unhybridized tight-binding d band is filled with electrons the structure-trend predicted is hcp → bcc → hcp → fcc → bcc (PETTIFOR [1972b]). Apart from the incorrect stability of the bcc phase at the noble-metal end of the series, this trend agrees with experiment for the *nonmagnetic* 4d and 5d series. The stability of the bcc phase in V and Cr, Nb and Mo, Ta and W, when the d band is

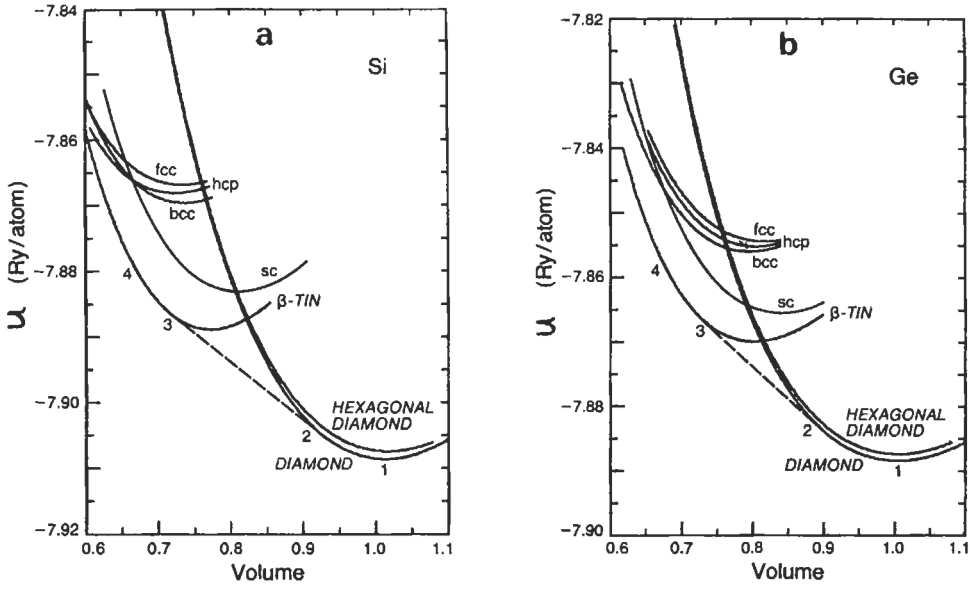

Fig. 34. The binding energy as a function of volume of (a) Si and (b) Ge for seven different crystal structures. The dashed line is the common tangent of the energy curves for the semiconducting diamond phase and the metallic β-tin phase, the system moving from $1 \rightarrow 2 \rightarrow 3 \rightarrow 4$ under pressure. (from YIN and COHEN [1980, 1981] and YIN [1982]).

nearly half-full, is due to the strong bonding-antibonding separation which is manifest in the bcc density of states compared to the close-packed (cf. fig. 26). The appearance of the bcc phase in iron is due to the presence of *ferromagnetism* (see § 8). The stability of different stacking-fault structures shows the same oscillatory behaviour as displayed by the fcc hcp curve in fig. 35 (PAPON *et al.* [1979]).

The number of d electrons, N_d, also influences the structure of the heavier alkalis and alkaline earths (TAKEMURA *et al.* [1982] and SKRIVER [1982]) and the rare earths (DUTHIE and PETTIFOR [1977]). N_d increases on moving down the *alkaline earth* group as the d band starts to fill (cf. fig. 20) so that Ca, Sr and Ba have 0.51, 0.59 and 0.87 $l=2$ electrons within the Wigner–Seitz sphere, respectively (SKRIVER [1982]). Similarly, under pressure N_d increases as the NFE-sp band moves up with respect to the TB-d band (cf. § 4.3). SKRIVER [1982] has computed the structural energy differences, using eq. (116), and has found that the trend hcp $\rightarrow$ fcc $\rightarrow$ bcc $\rightarrow$ hcp correlates with increasing Nd in agreement with the observed behaviour down group IIA (Be,Mg: hcp; Ca,Sr: fcc; Ba,Ra: bcc) and under pressure. The trivalent *rare-earth* crystal structure sequence hcp $\rightarrow$ Sm-type $\rightarrow$ double hcp $\rightarrow$ fcc, which is observed for decreasing atomic number and increasing pressure, can similarly be explained in terms of the change in number of d electrons accompanying valence s to d transfer (DUTHIE and PETTIFOR [1977]). Due to the lanthanide contraction of the ion core La has a 20% larger core radius than Lu, which results in La having 0.6 d electrons more than Lu and taking the double-hcp rather than the hcp crystal structure even though they are both trivalent.

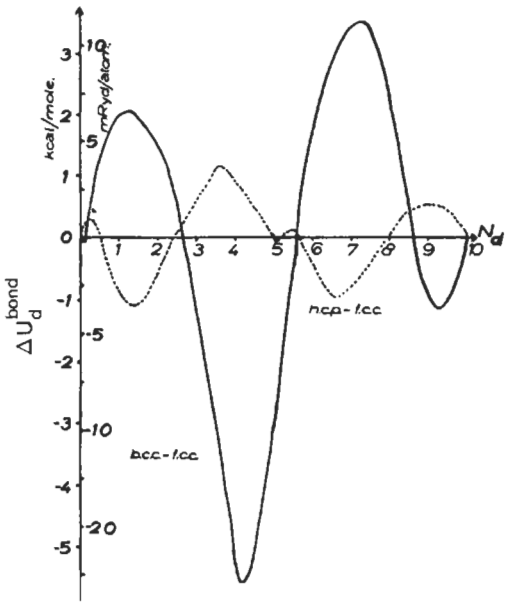

Fig. 35. The d bond energy of the bcc (solid line) and the hcp (dotted line) lattices with respect to the fcc lattice as a function of band filling N_d (from PETTIFOR [1972b]).

Recently *ab initio* Local Density Functional (LDF) calculations have been used to study the transformation path from bcc to hcp in barium under pressure at the absolute zero of temperature (CHEN *et al.* [1988]; HO and HARMAN [1990]). As illustrated in fig. 36, the bcc to hcp transformation involves atomic displacements corresponding to the zone boundary [110] T_1 phonon mode and an additional lattice shear (BURGERS [1934]). The dashed lines in fig. 36b show that a displacement $\delta = \sqrt{2}\,a/12$ in this bcc phonon mode creates a nearly hexagonal geometry, the perfect geometry being achieved in fig. 36c through a subsequent shear which changes the angle θ from 109.47° to 120°. Figure 37 displays the calculated total energy contours as a function of both co-ordinates δ and θ for barium at its equilibrium atomic volume Ω_0, $0.793\Omega_0$ and $0.705\Omega_0$, respectively. The latter volume corresponds to a pressure of 38.4 kbar. We see that at $\Omega = \Omega_0$ the upper contour plot shows that bcc barium is more stable than hcp, in agreement with experiment. However, as pressure is applied, the hcp phase has its energy lowered with respect to bcc. The middle contour plot shows that at $\Omega = 0.793\Omega_0$ their energies are approximately equal, with an energy barrier between them of about 4meV/atom. The lower contour plot shows that at $\Omega = 0.705\Omega_0$ the energy barrier has gone and the bcc phase is no longer metastable. The predicted $T = 0$ transformation pressure is 11 kbar, corresponding to the bcc and hcp lattices having equal enthalpies. However, at low temperatures the system would not be able to overcome the energy barrier so that the bcc phase would probably remain metastable until the T_1 N-point phonon mode became soft at 31 kbar. Experimentally the phase transformation occurs at a pressure of 55 kbar at room temperature so that the LDF predicted pressure appears too low, reflecting the intrinsic errors in the local approximation to density functional theory (see, for example, fig. 1).

References: p. 129.

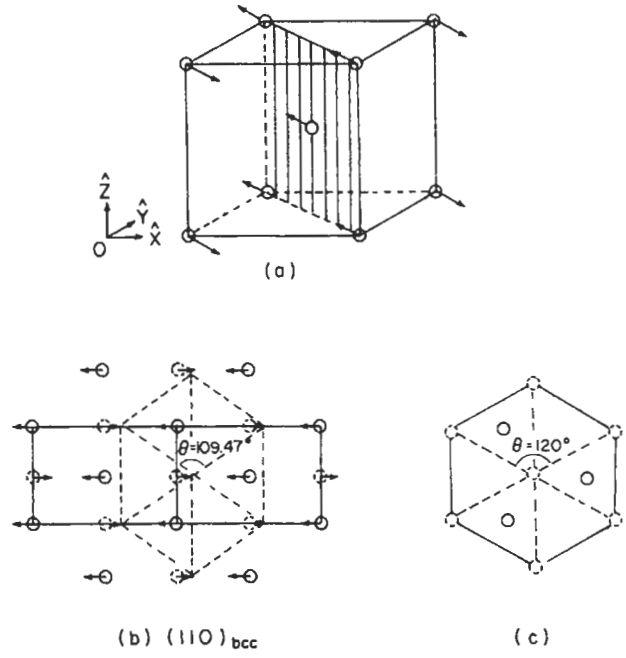

Fig. 36. Illustration of the bcc to hcp phase transformation. The arrows in (a) and (b) indicate the atomic displacements in the bcc lattice corresponding to the polarisation vector of the T_1 N-point phonon mode. A final long-wavelength shear changes the angle from 109.47° to 120° to obtain the hcp lattice in (c) (from Ho and Harmon [1990]; reproduced with permission).

6.2. Binary intermetallic phases

The structural trends within binary intermetallic phases $A_{1-x}B_x$ may be displayed by ordering the structural data base within a single three-dimensional structure map ($\mathfrak{M}_A$, $\mathfrak{M}_B$, x) where $\mathfrak{M}$ is a *phenomenological* co-ordinate which characterises each element in the periodic table (Pettifor [1988a]). The relative ordering *number* $\mathfrak{M}$ is obtained by running a one-dimensional string through the two-dimensional periodic table as shown in fig. 38; pulling the ends of the string apart places all the elements in sequential order, labelled by $\mathfrak{M}$.

The resultant two-dimensional isostoichiometric ground-state structure map ($\mathfrak{M}_A$, $\mathfrak{M}_B$) for the 50:50 AB binary compounds is shown in fig. 39 using the experimental database of Villars and Calvert [1985]. Similar maps for other stoichiometries may be found elsewhere (Pettifor [1988a], [1988b] and [1992])). The bare patches correspond to regions where compounds do not form due to either positive heats of formation or the competing stability of neighbouring phases with different stoichiometry. The boundaries do not have any significance other than they were drawn to separate compounds of

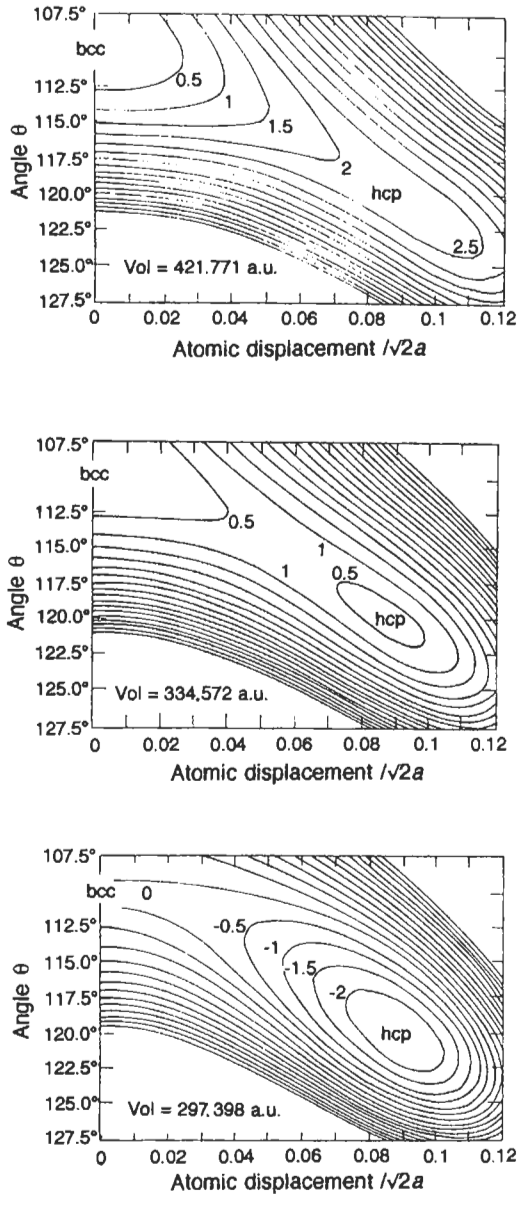

Fig. 37. Contour plots of the LDF energy for barium as a function of the atomic displacement δ corresponding to the T_1 N-point phonon mode and the angle θ of the shear motion. The upper, middle and lower panels correspond to the volumes Ω_0, $0.793\,\Omega_0$ and $0.705\,\Omega_0$, where Ω_0 is the observed equilibrium volume at ambient pressure. The energy contours are in steps of 0.5 mRy/cell (from Ho and HARMON [1990]; reproduced with permission).

References: p. 129.

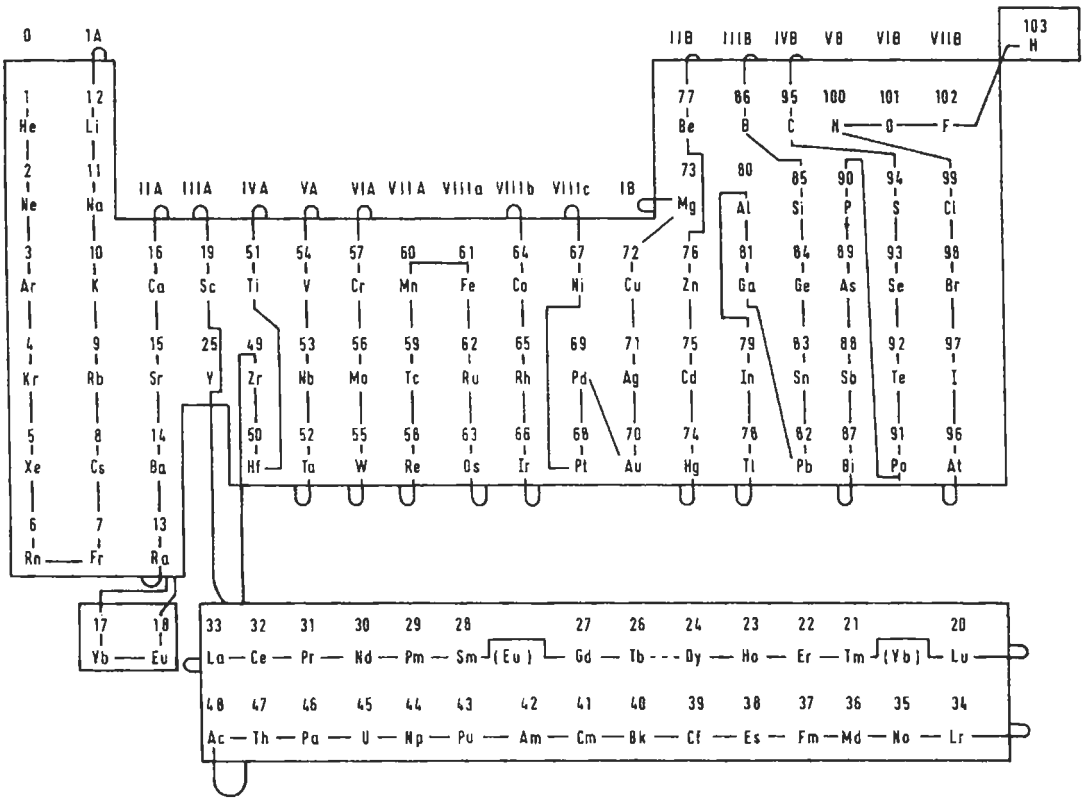

Fig. 38. The string running through this modified periodic table puts all the elements in sequential order according to the relative ordering number. (PETTIFOR [1988a]). Note that group II A elements Be and Mg have been grouped with II B, divalent rare earths have been separated from trivalent, and Y has been slotted between Tb and Dy.

different structure type. In regions where there is a paucity of data the boundary is usually chosen as the line separating adjoining groups in the periodic table. We see that excellent structural separation has been achieved between the 52 different AB structure types that have more than one representative compound each. The two most common structure types, namely B1 (NaCl) and B2 (CsCl), are well separated, the NaCl lattice being found only outside the region defined by $\mathfrak{M}_A$, $\mathfrak{M}_B \leq 81$, which encloses the main CsCl domain. There is only one exception, namely the very small region of Cs-containing salts. The AB structure map successfully demarcates even closely related structure types such as B27 (FeB) and B33 (CrB); $B8_1$ (NiAs) and B31 (MnP); or B3 (cubic ZnS, zincblende) and B4 (hexagonal ZnS, wurtzite). Moreover, coherent phases with respect to the bcc lattice, namely B2 (CsCl), B11 (CuTi), and B32 (NaTl) are also well separated, as too are the close-packed polytypes cubic $L1_0$ (CuAu) and hexagonal B19 (AuCd).

The structural trends within the pd-bonded AB compounds in fig. 39 have been successfully explained by PETTIFOR and PODLOUCKY [1984, 1986] within a simple two-centre, orthogonal Tight Binding (TB) model. The upper panel of fig. 40 shows the

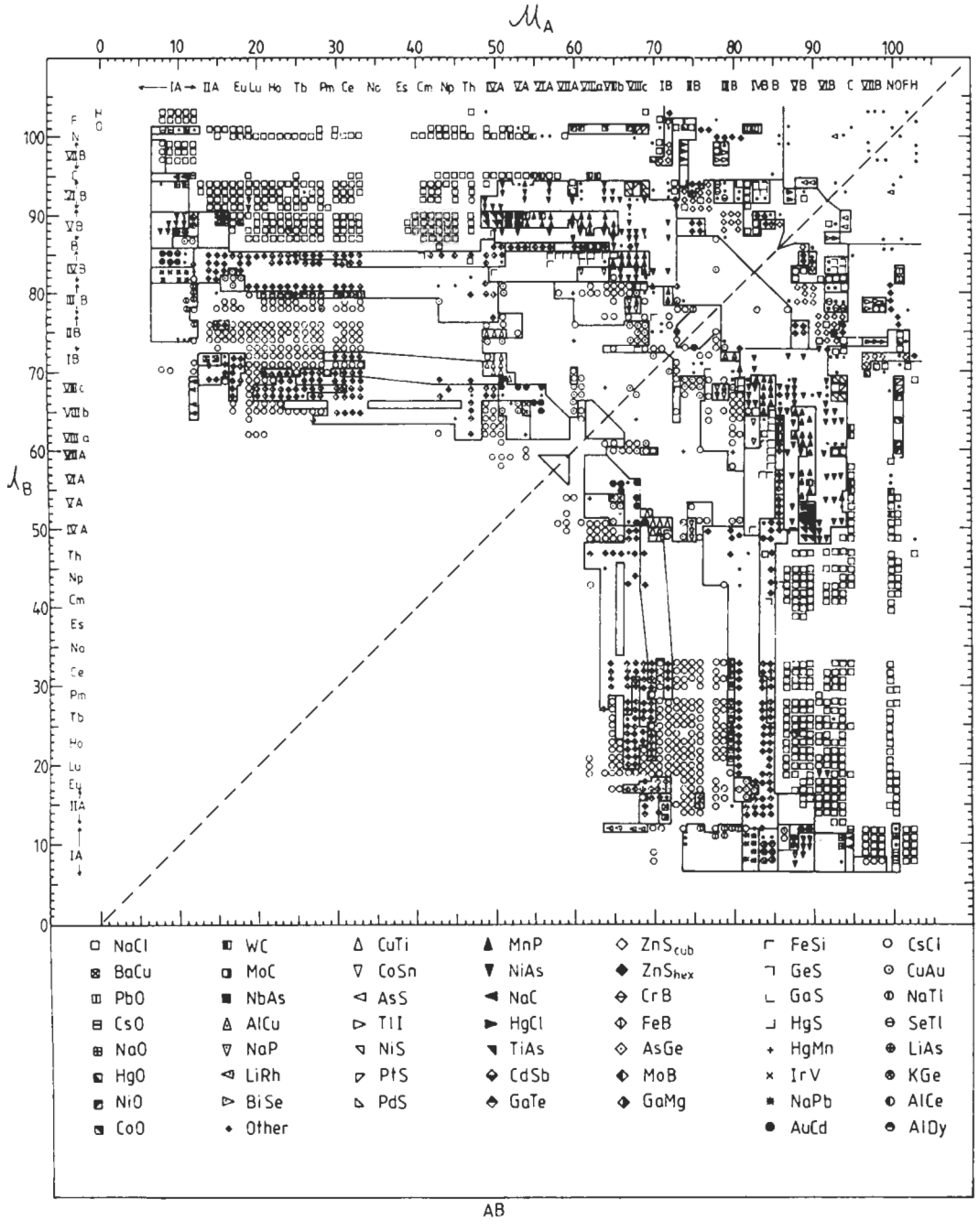

Fig. 39. The AB structure map (PETTIFOR [1988a]).

experimental structural domains for the seven most frequently occurring structure types, namely NaCl, CsCl, NiAs, MnP, FeB, CrB and FeSi respectively (using the socalled chemical scale χ which orders the elements in a similar way to the relative ordering number $\mathfrak{M}$ in fig. 38, PETTIFOR [1984]). The lower panel shows the *predicted* AB structure map (N_p, N_d) where N_p and N_d are the number of p and d valence electrons associated with atoms A and B respectively. We see that the TB model predicts the broad topological features of the experimental map. In particular, NaCl in the top left-hand corner adjoins NiAs running across to the right and boride stability running down to the bottom. MnP stability is found in the middle of the NiAs domain and towards the bottom right-hand corner, where it adjoins CsCl towards the bottom. The main failure of this simple pd TB model is its inability to predict the narrow-tongue of FeSi stability of the transition metal silicides, which is probably due to the total neglect of the valence s electrons within the model.

The theoretical TB calculations allowed the different roles played by relative atomic size, electronegativity difference, and electron per atom ratio in stabilizing a given structure type to be investigated directly (PETTIFOR and PODLOUCKY [1984, 1986]). Fig. 41 shows the fractional change in volume $(\Delta V)/V$ between a given structure type and

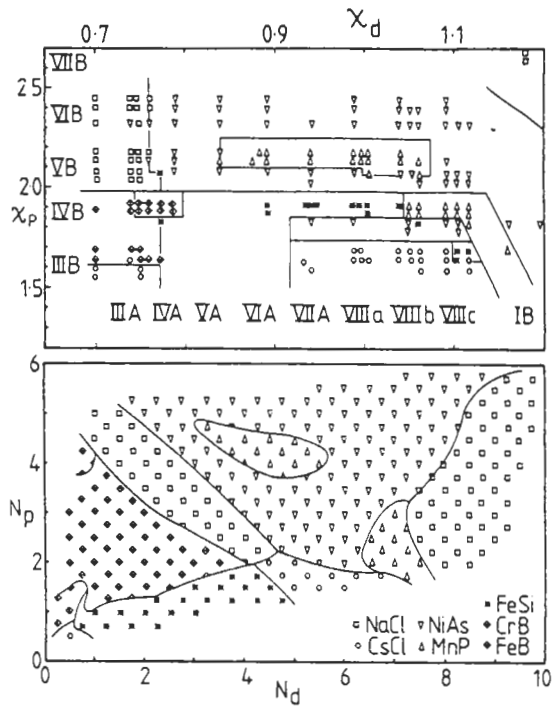

Fig. 40. The *upper* panel shows the structure map (χ_p, χ_d) for 169 pd bonded AB compounds, where χ_p and χ_d are values for the A and B constituents of a certain chemical scale, χ, which orders the elements in a similar way to the relative ordering number $\mathfrak{M}$. The *lower* panel shows the theoretical structure map (N_p, N_d) where N_p and N_d are the number of p and d valence electrons respectively on the CsCl lattice. (From PETTIFOR and PODLOUCKY [1984].)

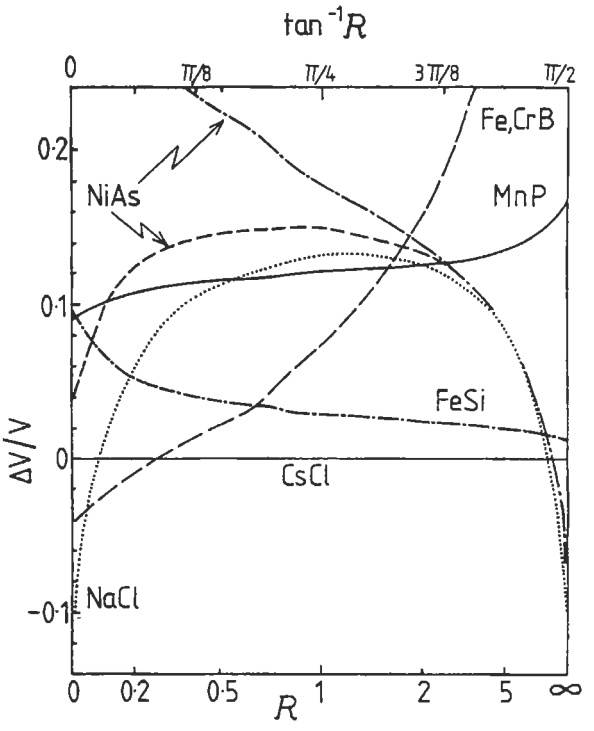

Fig. 41. The fractional change in volume $(\Delta V)/V$ with respect to the CsCl lattice versus the relative size factor $\mathfrak{R}$ (see text). The upper and lower NiAs curves correspond to $c/a = 1.39$ and $(8/3)^{1/2}$ respectively (PETTIFOR and PODLOUCKY [1984]).

the CsCl lattice as a function of the *relative size factor* $\mathfrak{R}$ of the constituent atoms. Within the TB model, $\mathfrak{R}$ had been defined through the relative strength of the pp repulsive pair potential compared to the dd repulsive pair potential. As expected, the NaCl lattice has the smallest volume at either end of the $\mathfrak{R}$ scale, because as the size of either the p-valent atom or the d-valent atom shrinks to zero the repulsion will be dominated by one or other of the close-packed fcc sublattices. On the other hand, in the middle of the scale, where the nearest-neighbour pd repulsion dominates, the volume of the NaCl lattice with six nearest neighbours is about 13% larger than the CsCl with eight nearest neighbours. The packing of hard spheres rather than the softer atoms would have led to the much larger volume difference of 30%.

The structural stability of the pd-bonded AB compounds may then be predicted by comparing the TB band energy of the different structure types at the volumes determined by the relative size factor $\mathfrak{R}$. Fig. 42 shows the resultant structural energies as a function of the *electron per atom ratio* or band filling N for the case where the atomic p level on the A site and the atomic d level on the B site are equal i.e. $E_{pd} = E_p - E_d = 0$. As the electron per atom ratio increases we find the structural sequence CsCl → FeSi → CrB

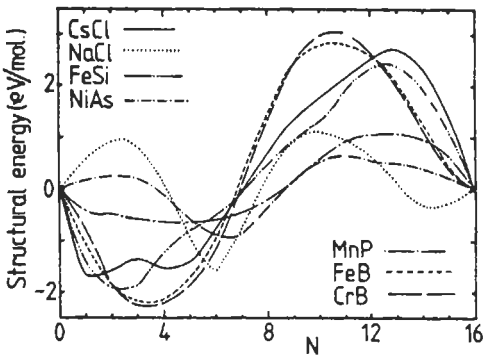

Fig. 42. The structural energy as a function of band filling N for the seven different crystal lattices with E_{pd} = 0 (PETTIFOR and PODLOUCKY [1984]).

→ NaCl → NiAs → (MnP) → NiAs → NaCl, where MnP, a distorted NiAs structure, has been put in parentheses because it does not quite have the lowest energy for $N \approx 9$. The structural energy depends not only on the electron per atom ratio but also on $E_{pd} = E_p - E_d$ which is a measure of a Mulliken-type *electronegativity difference*. Curves similar to fig. 42 have, therefore, been calculated for values of the atomic energy level difference in the range from −10 to +5 eV (in steps of 2.5 eV). Rather than plotting the most stable predicted structure on a structure map of E_{pd} versus N, the lower panel in fig. 40 uses the rotated frame of N_p versus N_d in order to make direct comparison with the experimental results in the upper panel.

The TB model has successfully accounted for the structural trends not only within the pd bonded AB compounds above but also within other families of AB_2 and AB_3 intermetallic phases (see, for example, JOHANNES *et al.* [1976], DUCASTELLE [1991], BIEBER and GAUTIER [1981], LEE [1991a and b], and OHTA and PETTIFOR [1989]). As expected, the structural stability of the binary phases is found to be controlled by four factors, namely the average number of valence electrons per atom (or band filling), a Mulliken-type electronegativity difference (or atomic energy level mismatch), the atomic size mismatch, and the angular character of the valence orbitals (or whether the bonding is pd, dd etc.). Classic ionic Madelung terms appear to play little role in determining the structures of intermetallic phases since the screening in a metal is perfect.

The most famous example of the crystal structure correlating with the average number of valence electrons per atom or band filling N is the Hume-Rothery alloy system of *noble* metals with the sp bonded elements such as Zn, Al, Si, Ge and Sn (see ch. 4). Assuming that Cu and Ag have a valency of 1, then the fcc α-phase is found to extend to a N of about 1.38, the bcc β-phase to be stabilized around 1.48, the γ-phase around 1.62 and the hcp ε-phase around 1.75. MOTT and JONES [1936] pointed out that the fcc and bcc electron-per-atom ratios correlate with the number of electrons required for a free-electron Fermi *sphere* to first make contact with the fcc and bcc Brillouin-zone faces, $N = 1.36$ and 1.48, respectively. This condition corresponds to $2k_F = |G|$ and

implies that the long-range Friedel oscillations (135) are in phase with the lattice, thereby giving an additional stabilizing energy. However, as found by STROUD and ASHCROFT [1971] this only leads to the fcc lattice being stabilized in the *immediate* vicinity of N = 1.36, the hcp lattice being the most stable for N < 1.3. The fcc noble metals with Z = 1 can, therefore, *not* be described by the NFE approximation.

JONES [1937], on the other hand, started with a realisitic value for the Cu energy gap at L, namely 4 eV, which is an order of magnitude larger than that expected for simple NFE metals (cf. fig. 16). This large gap, which arises from hybridization and orthogonality constraints with the underlying d band (MUELLER [1967]), leads to a very *non-spherical* Fermi surface which *already* for Cu with N = 1 just makes contact with the fcc Brillouin-zone face in the <111> direction. Contact is made with the bcc zone for N = 1.23. The resulting fcc and bcc densities of states look very similar to those for Be (fcc) and Li (bcc) in fig. 20, because JONES [1937] neglected the presence of the copper d band (cf. fig. 26). Comparing the fcc and bcc band energies JONES [1937] found that the fcc lattice was indeed the more stable for $1 \leq N < 1.43$. However, no comparison with the hcp lattice was made.

Recently, PAXTON *et al.* [1992] extended Jones' calculations to include not only the hcp lattice but also a proper treatment of the valence d electrons within the Rigid Band Approximation (RBA). Fig. 43 shows the structural predictions where the expected trend from fcc (α phase) to bcc (β phase) to hcp (ε phase) is found as a function of the electron per atom ratio or band filling N. This trend is a direct consequence of rigidly occupying the copper densities of states n(E) in the middle panel and comparing the resultant band energies, i.e.,

$$\Delta U = \Delta\left[\int^{E_F} En(E)dE\right] \tag{136}$$

where

$$N = \int^{E_F} n(E)dE. \tag{137}$$

It follows from equation (136) that

$$\frac{d}{dN}(\Delta U) = \Delta\left[\frac{dE_F}{dN} E_F n(E_F)\right] = \Delta E_F \tag{138}$$

since on differentiating equation (137) with respect to N we have immediately

$$\frac{dE_F}{dN} n(E_F) = 1. \tag{139}$$

Further, it follows from equations (138) and (139) that

$$\frac{d^2}{dN^2}(\Delta U) = \Delta\left[\frac{1}{n(E_F)}\right]. \tag{140}$$

References: p. 129.

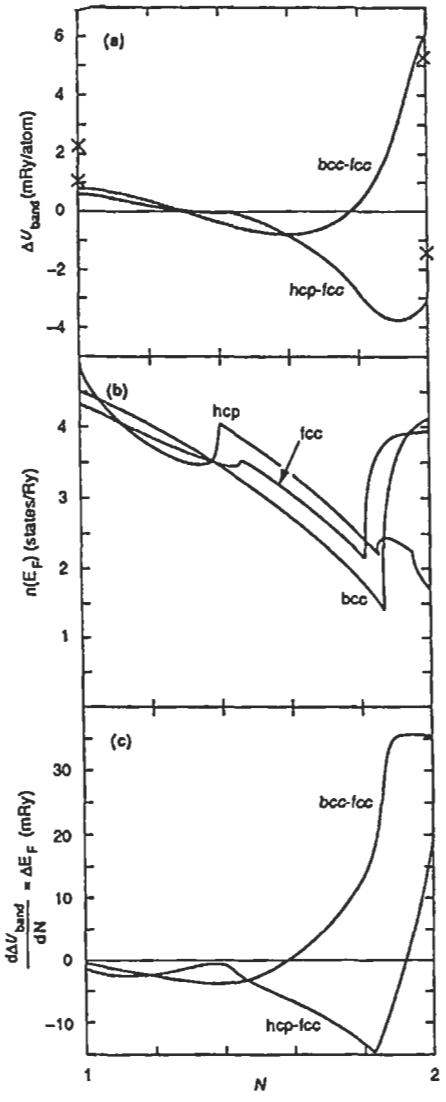

Fig. 43. Analysis of fcc, bcc and hcp relative structural stability within the rigid band approximation for Cu-Zn alloys. (a) The difference in band energy as a function of band filling N with respect to elemental rigid copper bands. (b) The density of states at the Fermi level E_F for fcc, bcc and hcp lattices as a function of band filling N. (c) The difference in the Fermi energies ΔE_F as a function of band filling N (from PAXTON, A. T., M. METHFESSEL and D. G. PETTIFOR [1992] unpublished).

Thus, as first pointed out by JONES [1962], the shape of the band energy difference curves in fig. 43a can be understood in terms of the relative behaviour of the densities of states in the middle panel. In particular, from equation (138) the stationary points in

the upper curve correspond to band occupancies for which ΔE_F vanishes in panel (c). Moreover, whether the stationary point is a maximum or a minimum depends on the relative values of the density of states at the Fermi level through equation (140). In particular, the bcc–fcc energy difference curve has a minimum around N = 1.6, where the bcc density of states is lowest, whereas the hcp–fcc curve has a minimum around N = 1.9, where the hcp density of states is lowest. The fcc structure is most stable around N = 1, where $\Delta E_F \simeq 0$ and the fcc density of states is lowest.

The structural trends in these Hume–Rothery electron phases are thus driven by the van Hove singularities in the densities of states which arise from band gaps at specific Brillouin or Jones zone boundaries as surmised earlier by MOTT and JONES [1936] and JONES [1937]. It is therefore not totally surprising that the NFE second-order perturbation theory results of STROUD and ASHCROFT [1971] and EVANS *et al.* [1979] found energy difference curves that are very similar to those in the top panel of fig. 43 *away* from the copper-rich end. The strong curvature of the bcc–fcc and hcp–fcc curves as a function of band filling can be reproduced only by including explicitly the weak logarithmic singularity in the slope of the Lindhard response function at $q = 2k_F$. It is for this reason that these Hume–Rothery alloys are correctly termed *electron phases* since this singularity is driven solely by the electron-per-atom ratio (through $2k_F$) and does not depend on the particular chemical constituents (through the pseudopotential). The nesting of the Fermi surfaces of noble metal alloys and the implication for long-period superlattices (SATO and TOTH [1961]) have been examined quantitatively by first-principles KRR band calculations (GYORFFY and STOCKS [1983]) assuming total disorder within the coherent-potential approximation (CPA; see, e.g., FAULKNER [1982]).

7. *Heat of formation*

A simple and successful *semi-empirical* scheme for calculating the heats of formation of binary alloys has been developed by MIEDEMA *et al.* [1980], who characterized each element in the Periodic Table by two co-ordinates ϕ^* and $\rho^{1/3}$. The heat of formation of a binary AB alloy is then written (in the simplest case) as:

$$\Delta H = -P(\Delta\phi^*)^2 + Q(\Delta\rho^{1/3})^2, \tag{141}$$

where P and Q are positive constants. The attractive term depends on the difference in the elemental work functions, $\Delta\phi$, (later modified to $\Delta\phi^*$) and is similar in spirit to PAULING'S [1960] electronegativity contribution. The repulsive term depends on the difference in the cube root of the electron densities at the elemental Wigner–Seitz sphere boundaries, $\Delta\rho^{1/3}$, and was argued to arise from the distortion of the charge density across the AB interface. Equation (141) has been useful in providing quantitative values for the heats of formation. In this section the *microscopic* origin of the attractive and repulsive contributions to ΔH will be examined in the light of our understanding of the cohesion of the elemental metals (cf. §§ 5 and 6).

Miedema's expression (141) has been most successful in the treatment of binary

transition-metal alloys, which are well-described by the tight-binding approximation. By analogy with FRIEDEL's [1964] treatment of pure transition metal cohesion, the AB alloy band may be approximated (PETTIFOR [1979, 1987]) by a rectangular density of states of width W_{AB} as shown in fig. 44. It follows from tight-binding theory (CYROT and CYROT-LACKMAN [1976]) that:

$$W_{AB}^2 = W^2 + 3(\Delta E_d)^2, \tag{142}$$

which generalizes the dimer result, eq. (30), to the bulk metal. The first term is the contribution to the square of the alloy band width that arises from nearest-neighbour bonding, whereas the second term reflects the increase in alloy bonding due to the ionicity which is measured by $\Delta E_d = E_d^B - E_d^A$. Thus, the alloy bandwith is given by

$$W_{AB} = \left[1 + 3(\Delta E_d/W)^2\right]^{1/2} W. \tag{143}$$

The heat of formation may now be evaluated explicitly. Filling up the alloy band with the average number of d electrons per atom, $\bar{N}_d$, and comparing the resulting band energy with that obtained from pure metal bands of width W (as illustrated in fig. 44), one finds the contribution to the heat of formation ΔH_0, given by:

$$\Delta H_0/W = -\tfrac{1}{80}(\Delta N_d)^2 - \tfrac{1}{4}\Delta N_d(\Delta E_d/W) - \tfrac{3}{40}\bar{N}_d(10 - \bar{N}_d)(\Delta E_d/W)^2, \tag{144}$$

where eq. (143) has been expanded to second order, and $\Delta N_d = N_d^B - N_d^A$. In addition, there is a further contribution ΔH_1, due to the fact that the elemental equilibrium atomic volumes V_A and V_B are in general different, so that the d bond energy of pure A and B is determined by W_A and W_B, respectively, and not by W as drawn in fig. 44. Assuming that the band width varies inversely with the volume to the five-thirds power (c.f. eq. (102); HEINE [1967]) and that the alloy volume is $V_{AB} = \bar{V} = 1/2(V_A + V_B)$ by Vegard's law, then

$$\Delta W = W_B - W_A = -\tfrac{5}{3} W(\Delta V/\bar{V}). \tag{145}$$

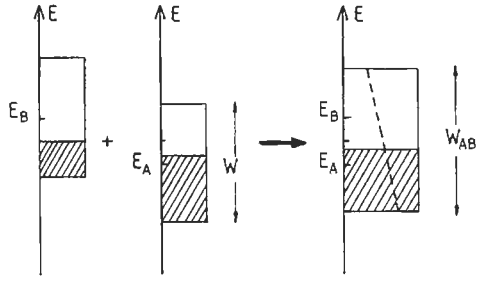

Fig. 44. The rectangular d band model representing AB alloy formation. The dashed line separates the partial density of states associated with atom A from that associated with atom B.

The resulting change in the bond energy due to the change in the band widths of the elemental metals from W to W_A, W_B, respectively is given by

$$\Delta H_1/W = -\tfrac{1}{24}\left(5 - \bar{N}_d\right)\Delta N_d\left(\Delta V/\bar{V}\right). \tag{146}$$

Expressions (144) and (146) may be simplified still further for binary alloys from the *same* transition-metal series. Choosing the 4d series because the 3d row is complicated by the presence of magnetism (cf. § 8), we can write $\Delta E_d = -\Delta N_d$ eV from fig. 5 and $V = V(N_d)$ from fig. 30. Substituting into eqs. (144) and (146) and taking W = 10 eV from table 1, the heat of formation (in eV/atom) is given to second order by

$$\Delta H = \left[f_0\left(\bar{N}_d\right) + f_1\left(\bar{N}_d\right)\right]\left(\Delta N_d\right)^2 \tag{147}$$

where

$$f_0\left(\bar{N}_d\right) = \tfrac{1}{8}\left[1 - \tfrac{3}{50}\,\bar{N}_d\left(10 - \bar{N}_d\right)\right] \tag{148}$$

and

$$f_1\left(\bar{N}_d\right) = -\tfrac{1}{24}\left(5 - \bar{N}_d\right)\left(\frac{\mathrm{d}\,\ln V}{\mathrm{d}N_d}\right)_{\bar{N}_d}. \tag{149}$$

Equation (147) represents the second-order term in a Taylor expansion of $\Delta H(N_d^A, N_d^B)$ in powers of ΔN_d as WILLIAMS *et al.* [1980b] have emphasized.

Figure 45 compares the results of the tight-binding theory with the MIEDEMA *et al.* [1980] semi-empirical values for $\Delta N_d \leq 4$, where we see that reasonable agreement is obtained. The more attractive values of ΔH found by MIEDEMA *et al.* [1980] near $\bar{N}_d = 5$ reflect *structural* bonding effects which are not included in the present model with its uniform alloy density of states (cf. fig. 44). The dependence of the heat of formation on crystal structure has been demonstrated by the first-principles LDF calculations of WILLIAMS *et al.* [1980b] who compared ΔH for the CuAu (fcc) and CsCl (bcc) lattices. It is clear from fig. 45 that the most stable AB alloys will be those for which the average d-band filling is close to 5.5 and ΔN_d is large, for example YPd. On the other hand, for average d-band fillings less than about 4 or greater than 7 the heat of formation will be positive.

The attractive contribution in Miedema's expression (141) may be identified with ΔH_0 provided that ϕ^* is interpreted as the *electronegativity* X rather than the work function ϕ. Within the TB model the charge transfer Q is obtained by assuming partial densities of states $n_A(E)$ and $n_B(E)$ on the A and B sites in the alloy as illustrated in fig. 44. n_A and n_B have been skewed so that their centres of gravity correspond to E_d^A and E_d^A, respectively (PETTIFOR [1980]). The resulting d charge transfer is given by

$$Q_d^B = \tfrac{1}{2}\,\Delta N_d + \tfrac{3}{10}\,\bar{N}_d\left(10 - \bar{N}_d\right)\left(\Delta E_d/W_{AB}\right). \tag{150}$$

The first term reflects the flow of electrons from right to left across the series due to increasing electron density and the second term reflects the flow from left to right due

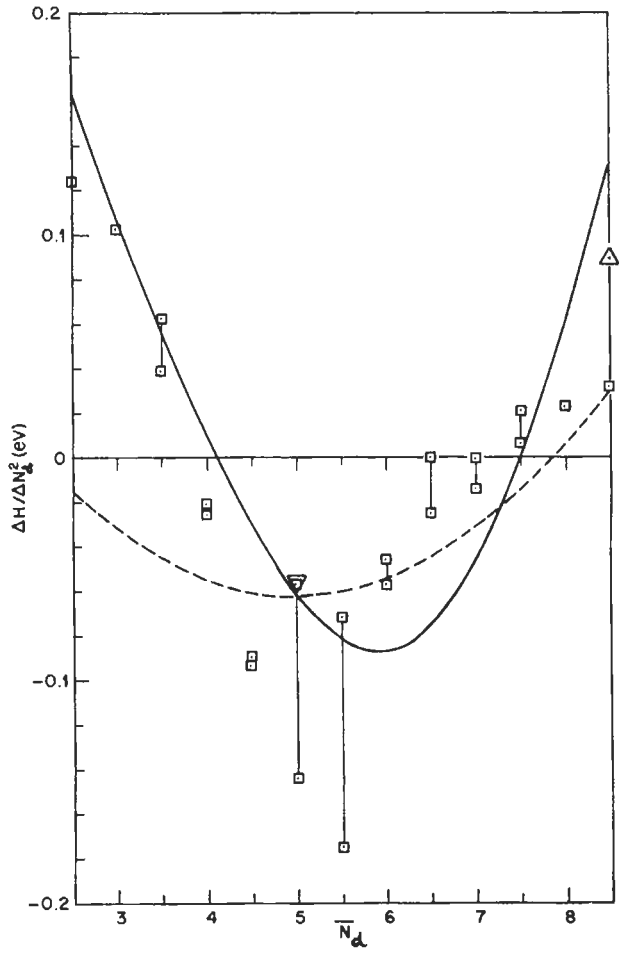

Fig. 45. $\Delta H/(\Delta N_d)^2$ as a function of the average band filling $\bar{N}_d$ for the 4d series. The dashed curve is the ΔH_0 contribution, eq. (148). The squares represent the Miedema values for the 4d alloys with $\Delta N_d \leq 4$, the points with common $\bar{N}_d$ being connected by straight lines. (From PETTIFOR [1979].)

to the increasingly attractive d level as one proceeds across the series (cf. fig. 5). The flow of electrons is, therefore, *not* driven by the difference in the *work functions* $\Delta\phi$ alone, because *all* the electrons throughout the band respond on alloying and not just those in the vicinity of the Fermi level. This can be seen by comparing, in fig. 44, the skewed partial density of states $n_A(E)$ in the AB alloy with the rectangular density of states in the pure metal A.

By implication, the charge transfer is proportional to the difference in the electronegativities, so that we may define a d-electronegativity X_d by

$$\Delta X_d = Q_d. \tag{151}$$

Substituting into eq. (150) and integrating for the 4d series with $\Delta E_d/W = \Delta N_d/10$, the electronegativity is found to be

$$X_d = -\tfrac{1}{2} N_d\left[1 - \tfrac{1}{50} N_d\left(15 - N_d\right)\right] + 1.8, \tag{152}$$

where the constant of integration has been chosen so that Mo with $N_d = 5$ takes the PAULING [1960] value of 1.8. Equation (152) is plotted in fig. 46 and compares surprisingly well with the Pauling electronegativities across the 4d series. It follows from eq. (144) and eqs. (150)–(152) that ΔH_0 can be expressed approximately as:

$$\Delta H_0 = -\tfrac{1}{10} W\left(\Delta X_d\right)^2 \tag{153}$$

for $|\overline{N}_d - 5| \leq 5/\sqrt{3}$. Equation (153) gives the correct value of the dashed curve in fig. 45 at the centre of the band and it vanishes at the correct cross-over points $\overline{N}_d = 5 \pm 5/\sqrt{3}$. Since Miedema's final choice of ordinate ϕ^* is very similar to Pauling's electronegativity X (MIEDEMA *et al.* [1980]), the attractive contribution in eq. (141) may be associated with ΔH_0 through eq. (153). The repulsive contribution in the semi-empirical scheme follows ΔH_1, very closely numerically, but conceptually the latter reflects a mismatch in the d band width rather than the electron density (see also WILLIAMS *et al.* [1982]). The heats of formation of 3d, 4d and 5d transition metal AB alloys have been tabulated by WATSON and BENNETT [1981] who used an optimized version of the d band model.

The heats of formation of *simple*-metal binary alloys may be calculated within second-order perturbation theory provided the valence difference $\Delta Z = Z_B - Z_A$ is not too large (HAFNER [1976] and LEUNG *et al.* [1976]). Neglecting the structurally dependent pair-potential contribution and ignoring the density dependence of $\phi(\boldsymbol{R}=0;\, r_s)$ in eq. (132), the heat of formation ΔH will be determined by the volume-dependent free electron gas terms alone. Assuming Vegard's Law with $V_{AB} = \overline{V} = \frac{1}{2}(V_A + V_B)$, these give (PETTIFOR and GELATT [1983]) the contribution (in eV/atom):

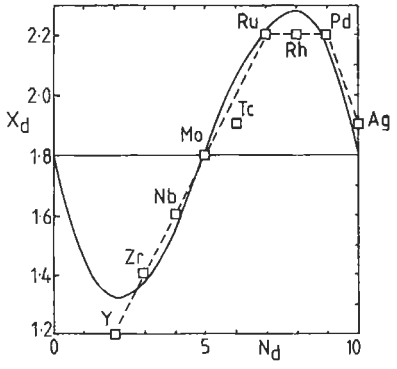

Fig. 46. The d-band electronegativity. X_d, compared to PAULING's [1960] values (squares) for the 4d series.

$$\Delta H_{eg} = \bar{Z} f_{eg}\left(\overline{\rho^{1/3}}\right)\left(\Delta\rho^{1/3}\right)^2, \tag{154}$$

where

$$f_{eg}\left(\rho^{1/3}\right) = -43.39 + 7.81/\rho^{1/3} + 0.17/\left(\rho^{1/3}\right)^2. \tag{155}$$

The three terms in eq. (155) are the kinetic, exchange and correlation contributions respectively, the flow of charge from the more dense to the less dense atom *lowering* the kinetic energy but raising the exchange and correlation energies. Equation (154) is reminiscent of the MIEDEMA *et al.* [1980] repulsive contribution in eq. (141). However, as is clear from fig. 47 the prefactor f_{eg} is not a positive constant Q but is dependent on the average cube root of the density $\rho^{1/3}$. It changes sign from *positive* at low densities (where the exchange and correlation dominate) to *negative* at high densities (where the kinetic energy dominates). The first-principle LDF calculations of ΔH for the Na, Mg, Al, Si, P series with respect to the CsCl (bcc) lattice show the same trend in fig. 47 as eq. (155) although displaced somewhat from the free-electron-gas result because the explicit influence of the core through the last two terms in eq. (132) has been neglected. Figure 6.10 b of HAFNER [1987] shows that equation (154) represents the experimental heat of formation of *liquid* simple metal alloys extremely well.

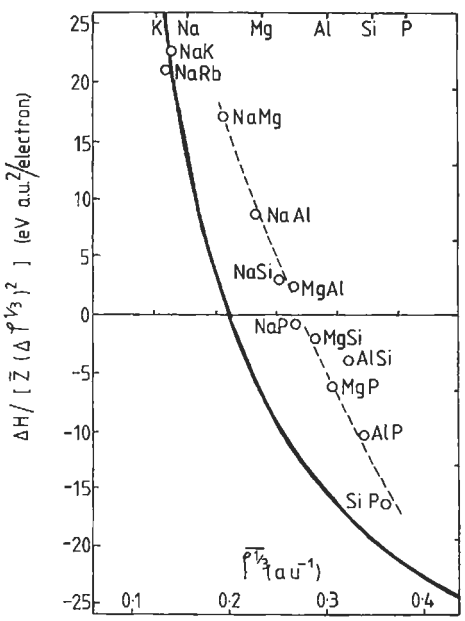

Fig. 47. $\Delta H/[\bar{Z}(\Delta\rho^{1/3})]^2$ as a function of the average cube root of the electron density $\rho^{1/3}$ for the 3s and 3p series. The solid curve is the electron-gas contribution, eq. (155). The open circles are the LDF results for the CsCl lattice. (From PETTIFOR and GELATT [1983]).

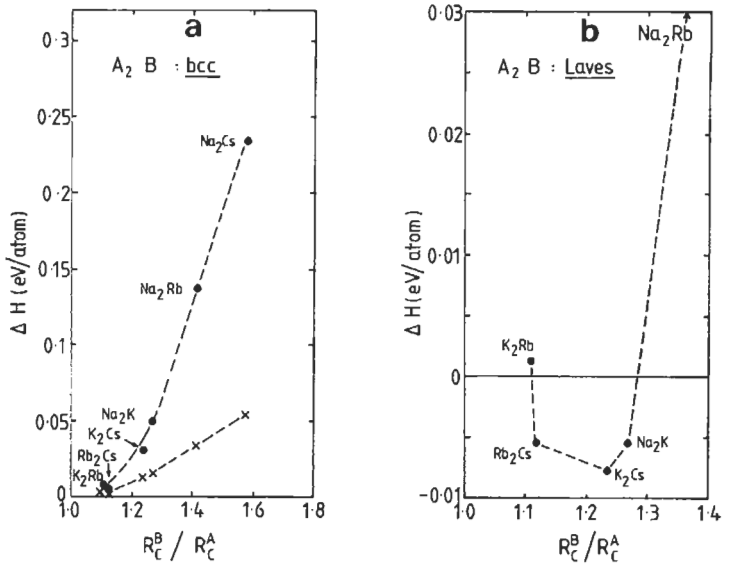

Fig. 48. The *calculated* heats of formation (HAFNER [1977]) of A_2B alkali-metal alloys for (a) the disordered bcc phase and (b) the ordered $MgZn_2$ Laves phase as a function of R_C^B/R_C^A from table 2. The crosses give the electron gas contribution eq. (154) using the *experimental* densities of the elemental metals.

Structural effects can be important in determining the sign of ΔH of simple-metal alloys (cf. § 2.3.2 of MIEDEMA *et al.* [1980]). This has been demonstrated by the second-order pseudopotential calculations of HAFNER [1977] on binary alkali metal alloys, which are illustrated in fig. 48 for the A_2B stoichiometry. (His values of ΔH for the bcc alloys are approximately four times larger than the experimental, LDF or free-electron gas values, because his calculated density differences are larger than experiment.) Whereas the disordered bcc alloys have *positive* heats of formation, the ordered Laves phases Rb_2Cs, K_2Cs and Na_2K have *negative* heats of formation due to the arrangement of the nearest-neighbour atoms with respect to the minimum in the pair potential. Therefore, provided the volume-dependent contribution to ΔH is not too large and positive, the structural contribution due to the pair potential can stabilize the phase. If a semi-conducting gap opens up in the alloy density of states, then this will provide additional stability (MIEDEMA *et al.* [1980]), which requires the theory to be extended beyond second order.

The heats of formation of sp elements with transition metals is illustrated by fig. 49 for the Li-row elements with the 4d transition metals. They were calculated by GELATT *et al.* [1983] using LDF theory for the AB stoichiometry with respect to the NaCl lattice. Their theoretical values agree broadly with the semi-empirical values of MIEDEMA *et al.* [1980] who found it necessary to include for sp-d alloys an additional attractive contribution, $-R$, in their expression (141). R is written as the product of two numbers which are determined by the groups in the Periodic Table from which the sp and d constituents are drawn. GELATT *et al.* [1983] have interpreted their results in terms of an *attractive* sp-d

bonding contribution, which becomes increasingly ionic on proceeding across the sp series from Li to F, and a *repulsive* d-bond contribution. The latter reflects the loss of d-bond energy due to the narrower alloy d band width, which arises from the larger transition-metal-transition-metal nearest neighbour distance in the alloy as compared to the elemental metal. Curves similar to fig. 49 have been obtained by GELATT *et al.* [1978] for the 3d and 4d transition-metal hydrides.

Figure 50 illustrates the reliability of LDF theory for predicting the heats of formation and structural stability of intermetallic phases. Figure 50a gives the LDF heats of formation of different ordered structures with respect to either the fcc or bcc lattices for the aluminium–lithium system (SLUITER *et al.* [1990]). We see that the B32 LiAl structure type is predicted to be much more stable than either the B2 or $L1_0$ equiatomic phases. Moreover, it is this strong stability of the B32 phase that is responsible for the known metastability of the neighbouring $L1_2$ $LiAl_3$ and DO_3 Li_3Al phases. Figure 50b gives the LDF heats of formation of different ordered structures with respect to either the fcc or hcp lattices for the aluminium-titanium system (VAN SCHILFGAARDE *et al.* [1990]). We see that the theory predicts the correct most stable ground state structure for Ti_3Al and $TiAl_3$, namely hexagonal DO_{19} and tetragonal DO_{22} respectively. Furthermore, whereas the metastable cubic $L1_2$ phase is very close to the ground state energy for $TiAl_3$, it is much further removed for Ti_3Al. This accounts for the fact that whereas Ti_3Al has been stabilized as a cubic pseudobinary by suitable alloying additions, it has not been possible to stabilize the cubic phase of Ti_3Al (LIU *et al.* [1989]). This demonstrates the importance of the first principles LDF calculations; they provide information not only about the ground state (which is usually already known experimentally) but also about the metastable phases (which have often not been directly accessed by experiment).

The heat of *solution* of hydrogen and helium in metals may be calculated within the *effective-medium* approximation of STOTT and ZAREMBA [1980], NØRSKOV and LANG

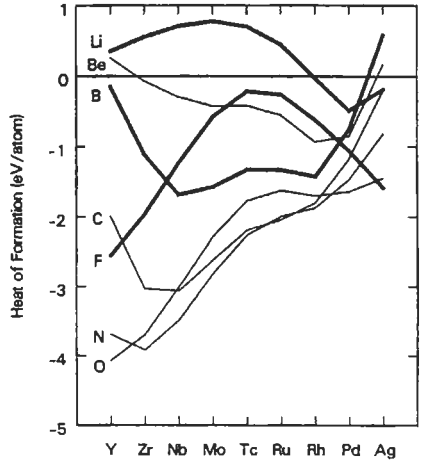

Fig. 49. The heats of formation of 4d transition metals with Li row elements in the NaCl structure (GELATT *et al.* [1983]).

[1980], and JACOBSEN *et al.* [1987]. They assumed that the energy required to embed an atom at some given position $\boldsymbol{R}$ in a host metal which is characterized by an *inhomogeneous* density $\rho(\boldsymbol{r})$, is the same as that required to embed the atom in a *homogeneous* electron gas of density $\rho = \bar{\rho}(\boldsymbol{R})$, where $\bar{\rho}(\boldsymbol{R})$ is the average host electron density seen by the impurity atom at $\boldsymbol{R}$. Then the energy of the impurity atom at position $\boldsymbol{R}$ in the host lattice is given to lowest order by

$$\Delta U(\boldsymbol{R}) = \left[\Delta U_{\text{hom}}(\rho)\right]_{\rho=\bar{\rho}(\boldsymbol{R})}. \tag{156}$$

The homogeneous embedding energy $\Delta U_{\text{hom}}(\rho)$ can be evaluated within LDF theory and the results for H and the rare-gas atoms He and Ne are shown in fig. 51a (PUSKA *et al.* [1981]). We see that the rare-gas atoms display a positive embedding energy at all densities because their full electronic shells *repel* the free electron gas through orthogonality constraints. On the other hand, the open-shell hydrogen atom shows a minimum at $\rho = 0.0026$ au^{-3} (i.e., $\rho^{1/3} = 0.138$ au^{-1}) corresponding to an *attractive* embedding energy of -1.8 eV, although it is repulsive for typical transition-metal densities of 0.02–0.03 au^{-3}.

The heats of solution of H and He across the 3d series are shown in fig. 51b after NØRSKOV [1982] and MANNINEN *et al.* [1982], respectively. The results include an important first-order *electrostatic* correction term to eq. (156), which reduces the slope of the He curve in fig. 51a by half and lowers the *H* curve by -120ρ eV au^3 so that the *H* embedding energy is attractive throughout the entire range of metallic densities (cf. the solid circles in fig. 51b). The behaviour of the helium heat of solution across the 3d series mirrors that of the host metallic density which varies like the bulk modulus shown in fig. 1. The hydrogen heat of solution is measured with respect to the binding energy of the H_2 molecule, namely -2.4 eV/atom. We see in fig. 51b that agreement with experiments is obtained only if a first-order *hybridization* correction is included from eq. (116) which reflects the bonding between the hydrogen impurity and the host nearest neighbour atoms (NØRSKOV [1982]). The effective-medium approximation with first-order electrostatic and hybridization corrections included has been applied successfully to defect problems such as the trapping energies of H and He by interstitials, vacancies and voids (NØRSKOV *et al.* [1982] and MANNINEN *et al.* [1982]). The electron theory of point defects has been reviewed by JENA [1981].

The *ordering* energy of a binary $A_c B_{1-c}$ alloy is defined by

$$\Delta U_{\text{ord}} = U_{\text{ord}} - U_{\text{dis}}, \tag{157}$$

where U_{ord} and U_{dis} are the energies in the completely ordered and disordered states respectively. By using second-order perturbation theory for the NFE *simple* metals (HAYES *et al.* [1968] and INGLESFIELD [1969]) or a generalized perturbation theory for the TB *transition* metals (DUCASTELLE and GAUTIER [1976]) the ordering energy eq. (157) can be expressed directly in terms of effective pair interactions ϕ_1, ϕ_2, ϕ_3,... between the first, second, third,... nearest neighbour atoms. (ϕ_n depends explicitly on $|\Delta v_{\text{ps}}(q)|^2$ for the simple metals and on $|\Delta E_{\text{d}}|^2$ for the transition metals). The ordering energy for $c \leq 0.5$ may be written (see, e.g., DE FONTAINE [1979] and DUCASTELLE [1991]) as:

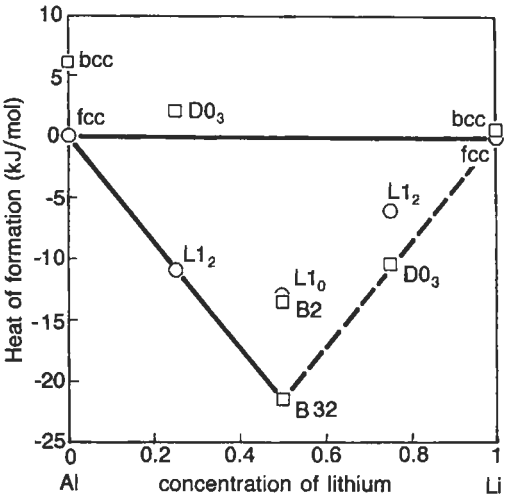

Fig. 50 (a). The predicted heat of formation of fcc- and bcc-based lithium-aluminium ordered compounds (after SLUITER *et al.* [1990]).

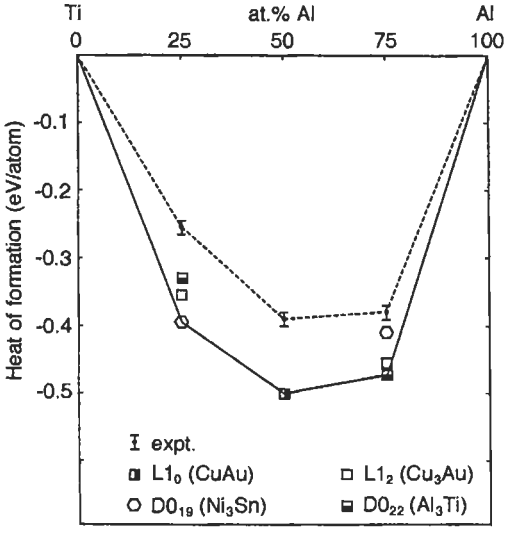

Fig. 50 (b). The predicted heat of formation of fcc- and hcp-based titanium-aluminium ordered compounds (after VAN SCHILFGAARDE *et al.* [1990]).

$$\Delta U_{\text{ord}} = \sum_n \left[p_n - (1-c)^2 z_n \right] \phi_n, \tag{158}$$

where z_n and p_n are the number of nth nearest neighbour atoms and B–B atom pairs respectively.

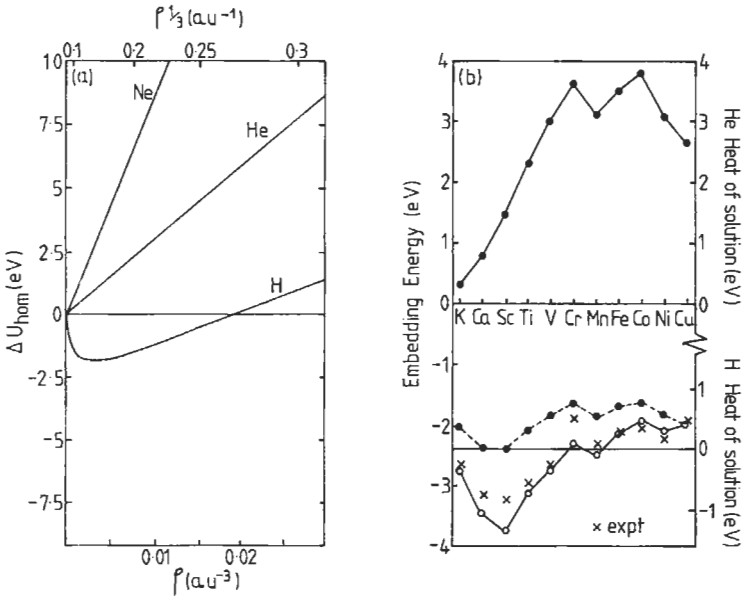

Fig. 51 (a) The homogeneous embedding energy for H and the rare gas atoms He and Ne in a free electron gas of density ρ (after PUSKA *et al.* [1981]). (b) The H and He heats of solution across the 3d series (after NØRSKOV [1982] and MANNINEN *et al.* [1982] respectively). The solid circles include a first-order electrostatic contribution. The open circles include, in addition, a first-order hybridization correction.

The effective pair interaction in transition metals with respect to an fcc lattice is illustrated by fig. 52a where ϕ_1 and ϕ_2 are plotted as a function of average band filling $\overline{N}_d$ for the TB d band alloy with $c = 0.25$ and $\Delta E_d / W = 0.45$ (BIEBER *et al.* [1983]). As expected from the behaviour of the simple-metal pair potentials in § 6.1, the transition-metal pair interactions display oscillations as a function of band filling, $\overline{N}_d$, and nearest neighbour position, n. Figure 52b compares the ordering energy evaluated by the pair interaction of DUCASTELLE and GAUTIER [1976] with the exact TB energy difference from eq. (157). We see that for this particular alloy it is a good approximation in the band-filling region where ordering occurs. Moreover, because the second and further nearest neighbour interactions are at least an order of magnitude smaller than the first nearest neighbour interactions, the ordering energy is dominated by ϕ_1 through eq. (158).

The pair interactions also determine the most stable ordered structure with respect to a given lattice (BIEBER and GAUTIER [1981]). For example, in fig. 53 the Cu_3Au and Al_3Ti structures are shown, which are built on the fcc lattice. They have the same type of first nearest neighbour atoms, so that their relative stability is determined by ϕ_2 and further nearest neighbour interactions. Since ϕ_2 in fig. 52a is negative for $4.4 < \overline{N}_d < 7.3$ when $\Delta E_d / W = 0.45$, the ordered structure with *like* second nearest neighbours will be the more stable, i.e., Cu_3Au. The stability reverses outside this band-filling region, thereby accounting for the nature of the structure map in fig. 53. This displays only a narrow

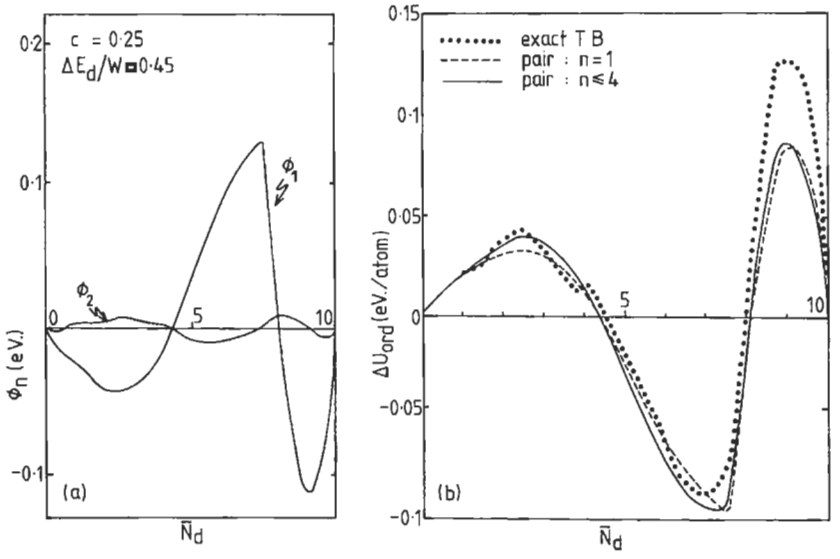

Fig. 52. (a) The first and second nearest neighbour effective pair interactions, ϕ_1 and ϕ_2, as a function of the average band filling, $\bar{N}_d$, for an AB_3 transition-metal alloy with a $\Delta E_d/W = 0.45$ on an fcc lattice. (b) A comparison with the exact result of the ordering energy evaluated using the effective pair interactions. (After BIEBER *et al.* [1983].)

stability range for the Al_3Ti phase, which is in agreement with empirical structure maps (BIEBER and GAUTIER [1981]).

This chapter on Electron Theory has been concerned primarily with the cohesive and structural properties of metals and alloys at the absolute zero of temperature. However, the derivation of effective pair interactions ϕ_n within electron theory allows the first-principles prediction of phase diagram behaviour by using these in an Ising Hamiltonian and performing Monte Carlo or Cluster Variation Method simulations (see, for example, DUCASTELLE [1991] and references therein, and ZUNGER [1994]). Chapter 6 deals explicitly with Phase Diagrams.

8. *Band theory of magnetism*

The magnetic 3d elements have anomalously large equilibrium atomic volumes and small bulk moduli as evidenced by the deviations in fig. 1 between experiment and the non-magnetic LDF theory. In this section we will see that the STONER [1939] theory of band magnetism can explain this anomalous behaviour.

A nonmagnetic system will become magnetic if the lowering in *exchange* energy due to the alignment of the electron spins more than compensates the corresponding increase in kinetic energy. This may be demonstrated by the rectangular d-band model of fig. 54. In the *nonmagnetic* state, the up and down spin electrons are equivalent and, therefore,

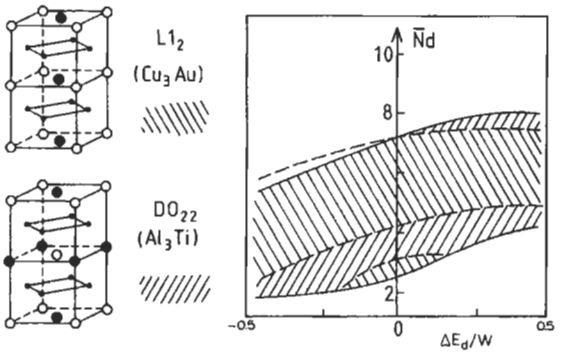

Fig. 53. The relative stability of the Cu_3Au and Al_3Ti structures as a function of the average band filling $\bar{N}_d$, and the renormalized difference in the atomic d levels, $\Delta E_d/W$ (after BIEBER and GAUTIER [1981]).

they have identical density of states $n_\uparrow$ and $n_\downarrow$ as shown in fig. 54a. In the *magnetic* state, the presence of a local magnetic moment, m, produces an exchange field Δ on the atom, of strength

$$\Delta = Im, \tag{159}$$

where I is the Stoner exchange parameter and $m = N_d^{\uparrow} - N_d^{\downarrow}$ in Bohr magnetons (μ_B). In the *ferromagnetic* state, all the atomic moments are aligned in the same direction, so that an up-spin electron sees the atomic level E_d shifted by $-\frac{1}{2}\Delta$ a on every site, the down-spin electron by $+\frac{1}{2}\Delta$. Therefore, the densities of states $n_\uparrow$ and $n_\downarrow$ are shifted *rigidly* apart by Δ as shown in fig. 54b. On the other hand, in the *antiferromagnetic* state, half the atoms have their moments aligned up, the other half have their moment aligned down, so that an electron sees two types of sites, with energies $E_d \pm \frac{1}{2}\Delta$. The problem is, therefore, analogous to that of the AB alloy discussed in the previous section (cf. fig. 44) and the densities of states $n_\uparrow$ and $n_\downarrow$ (corresponding to an atom with net moment up) are obtained by *skewing* the rectangular nonmagnetic densities of states as shown in fig. 54c.

The magnetic energy which accompanies the formation of a local moment m at each site, may be written as:

$$U_{\text{mag}} = \delta T - \tfrac{1}{4} Im^2, \tag{160}$$

where the first term is the change in the kinetic energy and the second is the lowering in energy due to exchange. The *ferromagnetic* (fm) state is created by flipping $\frac{1}{2}m$ down-spin electrons from just below the nonmagnetic Fermi level into the unoccupied up-spin states just above the nonmagnetic Fermi level. This is accompanied by an increase in kinetic energy of $(\frac{1}{2}m)/n(E_F)$ per electron, so that, to second order,

$$U_{\text{fm}} = \tfrac{1}{4} m^2/n(E_F) - \tfrac{1}{4} Im^2 \tag{161}$$

where in this section $n(E_F)$ refers to the nonmagnetic density of states *per spin*. Therefore, the nonmagnetic state will be unstable to ferromagnetism if $U_{\text{fm}} < 0$, i.e. if:

References: p. 129.

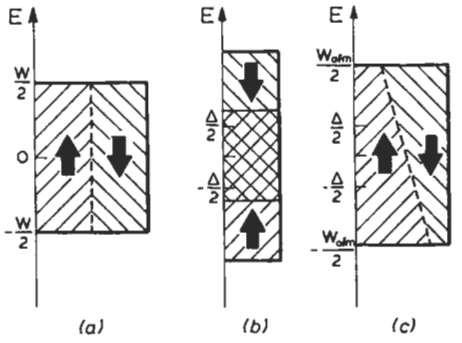

Fig. 54. The rectangular d band model of the (a) nonmagnetic, (b) ferromagnetic, and (c) antiferromagnetic states (after PETTIFOR [1980]).

$$In(E_F) > 1 \tag{162}$$

which is the famous *Stoner criterion.* The *equilibrium* value of m in the ferromagnetic state is determined by the condition

$$\overline{In(N_d, m)} = 1, \tag{163}$$

where $\overline{n(N_d, m)}$ is the average of the nonmagnetic density of states per spin between the two energies corresponding to a band-filling of $N_d^{\downarrow}$ and $N_d^{\uparrow}$ respectively (see, e.g., GUNNARSSON [1976]).

The magnetic energy of the *antiferromagnetic* (afm) state can be obtained (PETTIFOR [1980]) by adding up the band energies in fig. 54c and subtracting off the exchange energy which has been double-counted, i.e.:

$$U_{afm} = -\tfrac{1}{20}(W_{afm} - W)N_d(10 - N_d) + \tfrac{1}{4} Im^2, \tag{164}$$

where from eq. (142)

$$W_{afm} = \left\{1 + 3(\Delta/W)^2\right\}^{1/2} W. \tag{165}$$

Expanding eq. (165) to second order and using eq. (159), the nonmagnetic state is found to be unstable to antiferromagnetism if

$$I/W > \left[\tfrac{3}{10} N_d(10 - N_d)\right]^{-1}. \tag{166}$$

This is the rectangular d-band model criterion equivalent to the exact second-order result, namely

$$I\chi_q(E_F) > 1 \tag{167}$$

where $\chi_q(E_F)$ is the response function corresponding to the afm ordering wave vector $\boldsymbol{q}$ (see, e.g., FEDDERS and MARTIN [1966]). The usefulness of the present model is that eqs.

(164) and (165) include terms beyond second order so that the *equilibrium* value of the magnetic moment and energy may be obtained explicitly. Equation (164) is stationary for

$$m = \left(1/\sqrt{3}\right)\left\{\left[\tfrac{3}{10} N_d\left(10 - N_d\right)\right]^2 - \left(W/I\right)^2\right\}^{1/2} \tag{168}$$

when

$$U_{afm} = \left[\tfrac{1}{20} W N_d\left(10 - N_d\right) - \tfrac{1}{6} W^2/I\right] - \tfrac{1}{4} Im^2. \tag{169}$$

The first term in eq. (169) represents the change in kinetic energy, δT. The value of the moment given by eq. (168) is identical to that obtained by filling the up and down spin bands in fig. 54c and solving eq. (159) self-consistently.

Figure 55 shows the regions of stability of the ferromagnetic and antiferromagnetic phases as a function of the renormalized exchange integral, I/W, and band filling, N_d, for the rectangular d-band model (see also PENN [1966]). The fm and afm phases are stable for values of I/W above the critical curves ABC (fm) and DBE (afm), which are defined by eq. (162) with $n(E_F) = 5/W$ and eq. (166), respectively. In the region where both phases are stable, the fm and afm state have the lower energy in region FBE and ABF respectively.

The magnetic behaviour across the 3d series can be accounted for qualitatively (see also MORIYA [1965]) by assigning the 3d transition-metals values of N_d in fig. 55 which fix Ni with 0.6 holes. Values of I/W are chosen as marked by the crosses in fig. 55, the numbers lying in the range expected from first-principles LSDF calculations where $I \approx$ 1 eV and $W \approx 5$ eV for the 3d series (see, e.g., KÜBLER [1981]). I is approximately constant across the series but W increases from Ni to Cr just as observed in table 1 for the corresponding 4d series from Pd to Mo. Therefore, we expect I/W to decrease in moving from Ni to Cr, as shown in fig. 55. The positions of the crosses in fig. 55 imply that Ni and Co are strong ferromagnets with moments of 0.6 and 1.6 μ_B respectively,

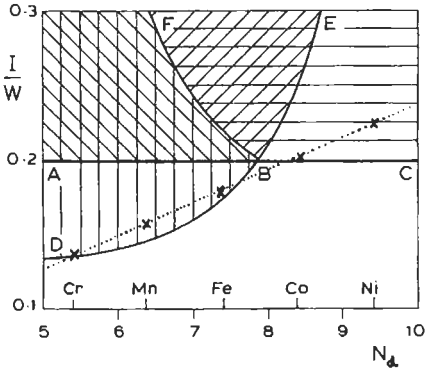

Fig. 55. The regions of stability of the ferromagnetic and antiferromagnetic states as a function of the renormalized exchange integral, I/W, and d band filling, N_d. The crosses mark plausible values of I/W across the 3d series. (After PETTIFOR [1980].)

whereas Fe ($I/W=0.180$), Mn($I/W=0.158$), and Cr ($I/W=0.136$) are anti-ferromagnets with local moments from eq. (168) of 0.9, 1.6 and 0.7 μ_B, respectively.

In practice, the rectangular d band model is not too bad a description of the *close-packed* fcc and hcp metals whose densities of states are fairly constant away from the top of the d band (c.f. fig. 26). This is demonstrated in fig. 56 by the band structure calculations of ASANO and YAMASHITA [1973] who evaluated the fm and afm local moments across the 3d series. Their fcc results are similar to those obtained from fig. 55. In particular, fcc iron is unable to maintain a fm moment, being instead a weak antiferromagnet. However, if I/W were to increase (by volume expansion), then fig. 55 implies that fcc iron eventually stabilizes in the fm state as has been observed experimentally by GRADMANN and ISBERT [1980] and theoretically by the LSDF calculations of KÜBLER [1981].

On the other hand, bcc transition metals have a very non-uniform density of states and are characterized by a very marked antibonding peak for $N \approx 8$ electrons (cf. fig. 26a). $n(E_F)$ is sufficient for the 3d transition metal iron to satisfy the Stoner criterion (162) and the resulting magnetic energy of – 0.3 eV/atom (JANAK and WILLIAMS [1976]) stabilizes the bcc lattice with respect to the nonmagnetic or weakly afm close-packed lattices. Under pressure, however, the d band broadens and the density of states decreases, thereby leading to an increased kinetic-energy contribution in eq. (161). At just over 10 GPA the nonmagnetic structural energy contribution in fig. 35 wins out and ferromagnetic bcc α-iron transforms to the nonmagnetic hcp ε-phase (MADSEN *et al.* [1976]). This is the most stable structure of the isovalent 4d and 5d elements Ru and Os at their equilibrium volume because their wider d bands prevent them from satisfying the Stoner criterion. At atmospheric pressure bcc α-iron transforms to the fcc γ-phase at 1184 K and changes back to the bcc δ-phase at 1665 K just before melting at 1809 K. The occurrence of the α, γ, δ and ε-phases in the temperature–pressure phase diagram of iron can be understood qualitatively (HASEGAWA and PETTIFOR [1983]) within a band theory of magnetism which extends Stoner theory to finite temperatures (CYROT [1970], HASEGAWA [1980] and HUBBARD [1981]).

The simple rectangular d band model of antiferromagnetism presented in fig. 54c does not include any Fermi-surface *nesting* effects which LOMER [1962] argued were

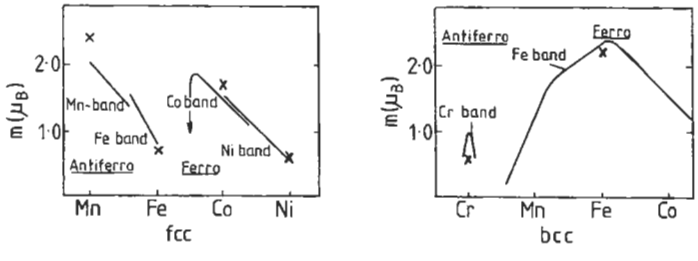

Fig. 56. The magnetic moments of the 3d metals in the ferromagnetic and antiferromagnetic states calculated as a function of band filling by ASANO and YAMASHITA [1973] for the fcc and bcc lattices. The crosses mark the experimental values.

responsible for the observed periodicity of the bcc Cr spin density wave. In practice, even though nesting provides only a small contribution to $\chi_q(E_F)$ in eq. (167), it is sufficient to take *bcc* Cr across the afm stability curve DBE in fig. 55 (WINDSOR [1972] and SKRIVER [1981a]).

The anomalous behaviour of the equilibrium atomic volumes and bulk moduli of the 3d series observed in fig. 1 is due to the *magnetic pressure*, $P_{mag} = -\,dU_{mag}/dV$, which accompanies moment formation (SHIGA and NAKAMURA [1969] and JANAK and WILLIAMS [1976]). Assuming that I is volume-independent (MADSEN *et al.* [1976]) and W varies inversely with volume to the five-thirds power (HEINE [1967]), it follows from eqs. (161), (164) and (169) that

$$3P_{mag}V = 5\delta T, \tag{170}$$

because $\delta U_{mag}/\delta m = 0$ at equilibrium.

In particular, for the *ferromagnetic* state the kinetic-energy change, δT, may be approximated by the first term in eq. (161), so that

$$3P_{fm}V = \tfrac{5}{4}\, m^2/n(E_F). \tag{171}$$

JANAK and WILLIAMS [1976] have shown that this simple expression accounts for the increase in equilibrium volume on going to the ferromagnetic state which the LSDF results display in fig. 57. For example, iron and nickel have moments of 2.2 and 0.6 μ_B, respectively, and LDF nonmagnetic density of states per spin of 1.5 and 2.2 states per eV atom respectively. Substituting into eq. (171) gives a magnetic pressure for iron and nickel of 21.2 and I GPA, respectively, which leads to an increase in the equilibrium volume of 7% and $\frac{1}{2}$%, respectively. The increase in atomic volume reduces the bulk modulus because the valence s electrons are now no longer compressed to the same extent into the core region where they are repelled by orthogonality effects (cf. § 5.2).

Figure 57 shows that the experimental *trend* in the equilibrium atomic volume and bulk modulus across the ferromagnetic metals Fe, Co and Ni is well accounted for by the LSDF results (JANAK and WILLIAMS [1976]). Similarly, SKRIVER *et al.* [1978] have obtained good agreement with experiment across the 5f actinide series, where the LSDF calculations reproduce the sudden 30% volume expansion that is observed in going from Pu to Am, due to the formation of a 5f moment. The 4f rare earths Ce and Pr have also been studied within LSDF theory, by GLOTZEL [1978] and SKRIVER [1981b] respectively, as too has the permanent magnet $Nd_2Fe_{14}B$ (COEHOORN [1992]) and various magnetic mutilayers (EDWARDS [1992]). However, errors remain in figs. 1 and 50 (for the 3d metals in particular) which must be attributed to the *local* approximation to the exchange and correlation energy functional. For example, LDF theory does not position the valence s and d bands in exactly the correct relative position (HARRIS and JONES [1978]) or provide the correct exchange splitting in nickel (WOHLFARTH [1980] and COOKE *et al.* [1981]). Although the correlations can be treated perturbatively within a TB framework (FRIEDEL and SAYERS [1977]), a simple *non-local* extension of the LDF approximation will be required for the next generation of higher-accuracy first-principles calculations (see, e.g., JONES and GUNNARSSON [1989]).

References: p. 129.

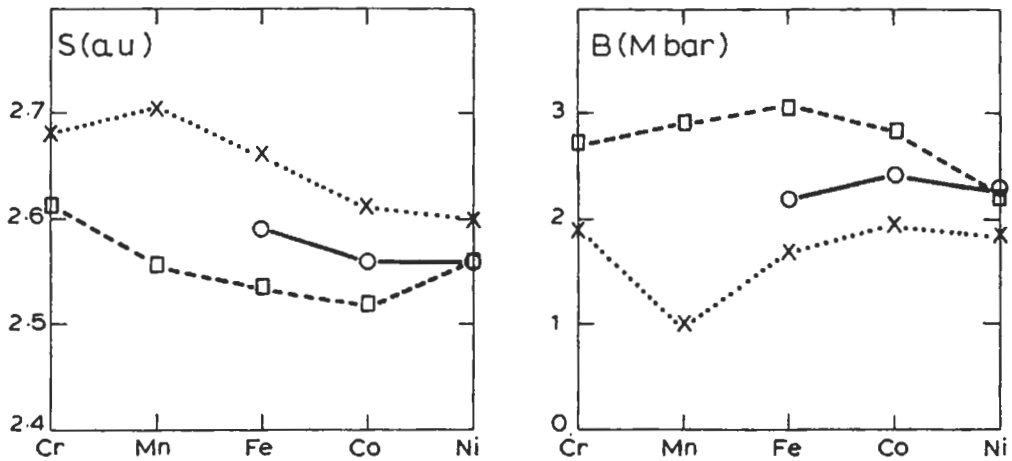

Fig. 57. The equilibrium Wigner-Seitz radius, S, and bulk modulus, B, across the magnetic 3d transition metals. The crosses, circles. and squares are the experimental, spin-polarized LSDF and nonmagnetic LDF results, respectively. (After JANAK and WILLIAMS [1976].)

References

ANDERSEN, O.K., 1973, Solid State Commun. **13**, 133.
ANDERSEN, O.K., 1975, Phys. Rev. **B12**, 3060.
ANDERSEN, O.K., 1980, §5.3 of A.R. MACKINTOSH and O.K. ANDERSEN, in: Electrons at the Fermi Surface, ed. M. Springford (Cambridge Univ. Press).
ANDERSEN, O.K., and O. JEPSEN, 1977, Physica **B91**, 317.
ASANO, S., and J. YAMASHITA, 1973, Prog. Theor. Phys. **49**, 373.
ASHCROFT, N.W., 1966, Phys. Lett. **23**, 48.
ASHCROFT, N.W., and D.C. LANGRETH, 1967, Phys. Rev. **155**, 682.
BACHELET, G.B., D.R. HAMANN and M. SCHLUTER, 1982, Phys. Rev. **B26**, 4199.
BIEBER, A., and F. GAUTIER, 1981, Solid State Commun. **38**, 1219.
BIEBER, A., F. DUCASTELLE, F. GAUTIER, G. TREGLIA and P. TURCHI, 1983, Solid State Commun. **45**, 585.
BLOCH, A.N., and G.C. SCHATTEMAN, 1981, in: Structure and Bonding in Crystals, vol. I, eds. O'Keefe and Navrotsky (Academic, New York).
BRANDOW, B.H., 1977, Adv. Phys. **26**, 651.
BURGERS, W.G., 1934, Physica **1**, 561.
*CALLAWAY, J., 1964, Energy Band Theory (Academic, London).
CHELIKOWSKY, J.R., 1981, Phys. Rev. Lett. **47**, 387.
CHEN, Y., K.M. HO, and B.N. HARMON, 1988, Phys. Rev. **B37**, 283.
*COEHOORN, R., 1992, in: Electron Theory in Alloy Design, eds. D.G. Pettifor and A.H. Cottrell (Institute of Materials, London) ch. 8.
COOKE, J.F., J.W. LYNN and H.L. DAVIS, 1980, Phys. Rev. **B21**, 4118.
COULSON, C.A., L.R. REDEI and D. STOCKER, 1962, Proc. Roy. Soc. **A270**, 357.
CRESSONI, J.C., and D.G. PETTIFOR, 1991, J. Phys.: Condens. Matter **3**, 495.
CYROT, M., 1970, Phys. Rev. Lett. **25**, 871.
CYROT, M., and F. CYROT-LACKMANN, 1976, J. Phys. **F6**, 2257.
DE FONTAINE, 1979, Solid State Physics, vol. 34 (Academic, New York).
DUCASTELLE, F., 1970, J. Physique **31**, 1055.
*DUCASTELLE, F., 1991, Order and Phase Stability in Alloys (North-Holland, Amsterdam).
DUCASTELLE, F., and F. GAUTIER, 1976, J. Phys. **F6**, 2039.
DUTHIE, J.C., and D.G. PETTIFOR, 1977, Phys. Rev. Lett. **38**, 564.
EDWARDS, D.M., 1992, in: Electron Theory in Alloy Design, eds. D.G. Pettifor and A.H. Cottrell (Institute of Materials, London) ch. 9.
FAULKNER, J.S., 1982, Prog. Mater. Sci. **27**, 1.
FEDDERS, P.A., and P.C. MARTIN, 1966, Phys. Rev. **143**, 245.
FINNIS, M.W., 1974, J. Phys. **F4**, 1645.
*FINNIS, M.W., 1992, in: Electron Theory in Alloy Design, eds. D.G. Pettifor and A.H. Cottrell (Institute of Materials, London) ch. 2.
FRIEDEL, J., 1952, Phil. Mag. **43**, 153.
FRIEDEL, J., 1964, TMS AIME **230**, 616.
FRIEDEL, J., 1969, in: The Physics of Metals, ed. J.M. Ziman (Cambridge Univ. Press, New York) p. 494.
FRIEDEL, J., and C.M. SAYERS, 1977, J. Physique **38**, 697.
GELATT, C.D., H. EHRENREICH and R.E. WATSON, 1977, Phys. Rev. **B15**, 1613.
GELATT, C.D., H. EHRENREICH and J.A. WEISS, 1978, Phys. Rev. **B17**, 1940.
GELATT, C.D., A.R. WILLIAMS and V.L. MORUZZI, 1983, Phys. Rev. **B27**, 2005.
GIRIFALCO, L.A., 1976, Acta Metall. **24**, 759.
GLÖTZEL, D., 1978, J. Phys. **F8**, L163.
GRADMANN, U., and H. ISBERT, 1980, J. Magn. Magn. Mater. **15-18**, 1109.
GUNNARSSON, O., 1976, J. Phys. **F6**, 587.
GUNNARSSON, O., and B.I. LUNDQUIST, 1976, Phys. Rev. **B13**, 4274.

GYORFFY, B. L., and G. M. STOCKS, 1983, Phys. Rev. Lett. **50**, 374.
HAFNER, J., 1974, Phys. Rev. **B10**, 4151.
HAFNER, J., 1976, J. Phys. **F6**, 1243.
HAFNER, J., 1977, Phys. Rev. **B15**, 617.
*HAFNER, J., 1987, From Hamiltonians to Phase Diagrams: The Electronic and Statistical Mechanical Theory of sp-bonded Metals and Alloys, Solid State Sciences **70** (Springer, Berlin).
HAFNER, J., 1989, in: The Structures of Binary Compounds, eds. F. R. de Boer and D. G. Pettifor (North-Holland, Amsterdam) p. 147.
HARRIS, J., and R. O. JONES, 1978, J. Chem. Phys. **68**, 3316.
HARRISON, W. A., 1959, Phys. Rev. **116**, 555.
HARRISON, W. A., 1960, Phys. Rev. **118**, 1190.
*HARRISON, W. A., 1966, Pseudopotentials in the Theory of Metals (Benjamin, New York).
*HARRISON, W. A., 1980, Electronic Structure and the Properties of Solids (Freeman, San Francisco).
HASEGAWA, H., 1980, J. Phys. Soc. Japan **49**, 963.
HASEGAWA, H., and D. G. PETTIFOR, 1983, Phys. Rev. Lett. **50**, 130.
HAYES, T. M., H. BROOKS and A. R. BIENENSTOCK, 1968, Phys. Rev. **175**, 699.
HEINE, V., 1967, Phys. Rev. **153**, 673.
HEINE, V., and I. ABARENKOV, 1964, Phil. Mag. **9**, 451.
*HEINE, V., and D. WEAIRE, 1970, Solid State Physics, vol. 24 (Academic, New York).
HERMAN, F., and S. SKILLMAN, 1963, Atomic Structure Calculations (Prentice Hall, Englewood Cliffs, NJ).
HERRING, C., 1940, Phys. Rev. **57**, 1169.
HO, K., and B. N. HARMON, 1990, Mater. Sci. Eng. **A127**, 155.
HODGES, L., H. EHRENREICH and N. D. LANG, 1966, Phys. Rev. **152**, 505.
HOHENBERG, P., and W. KOHN, 1964, Phys. Rev. **136**, B864.
HUBBARD, J., 1967, Proc. Phys. Soc. **92**, 921.
HUBBARD, J., 1981, Phys. Rev. **B23**, 5974.
INGLESFIELD, J. E., 1969, J. Phys. **C2**, 1285.
JACOBS, R. L., 1968, J. Phys. **C1**, 492.
JACOBSEN, K. W., J. K. NØRSKOV, and M. J. PUSKA, 1987, Phys. Rev. **B35**, 7423.
JACUCCI, G., and R. TAYLOR, 1981, J. Phys. **F11**, 787.
JAN, J-P., and A. R. WILLIAMS, 1976, Phys. Rev. **B14**, 4199.
JENA, P., 1981, Treatise Mater. Sci. Tech. **21**, 351.
JEPSEN, O., O. K. ANDERSEN and A. R. MACKINTOSH, 1975, Phys. Rev. **B12**, 3084.
JOHANNES, R. L., R. HAYDOCK and V. HEINE, 1976, Phys. Rev. Lett. **36**, 372.
JONES, H., 1973, Proc. Phys. Soc. (London) **49**, 250.
JONES, R. O., and O. GUNNARSSON, 1989, Rev. Mod. Phys. **61**, 689.
KAUFMAN, L., and H. NESOR, 1973, in: Titanium Science and Technology, vol. 2, eds R. I. Jaffe and H. Burte (Plenum, New York) p. 773.
*KITTEL, C., 1971, Introduction to Solid State Physics (Wiley, New York).
KOHN, W., and N. ROSTOKER, 1954, Phys. Rev. **94**, 1111.
KOHN, W., and L. J. SHAM, 1965, Phys. Rev. **140**, A1133.
KOLLAR, J., and G. SOLT, 1974, J. Phys. Chem. Solids **35**, 1121.
KORRINGA, J., 1946, Physica **13**, 392.
KÜBLER, J., 1981, Phys. Lett. **81A**, 81.
LEE, S., 1991a, J. Am. Chem. Soc. **113**, 101.
LEE, S., 1991b, Acc. Chem. Res. **24**, 249.
LEUNG, C. H., M. J. STOTT and W. H. YOUNG, 1976, J. Phys. **F6**, 1039.
LIBERMAN, D. A., 1971, Phys. Rev. **B3**, 2081.
LIU, C. T., J. A. HORTON, and D. G. PETTIFOR, 1989, Mat. Res. Soc. Symp. Proc. **133**, 37.
LOMER, W. M., 1962, Proc. Phys. Soc. **A80**, 489.

MADSEN, J., O. K. ANDERSEN, U. K. POULSEN and O. JEPSEN, 1976, in: Magnetism and Magnetic Materials, 1975, Philadelphia, eds. J. J. Becker and G. H. Lander (AIP Conf. Proc. 29, New York) p. 327.
MANNINEN, M., J. K. NØRSKOV and C. UMRIGAR, 1982, J. Phys. **F12**, L1.
MATTHEISS, L. F., 1972, Phys. Rev. **B5**, 290.
MCMAHAN, A. K., and R. C. ALBERS, 1982, Phys. Rev. Lett. **49**, 1198.
MCMAHAN, A. K., and J. A. MORIARTY, 1983, Phys. Rev. **B27**, 3235.
MIEDEMA, A. R., P. F. DE CHATEL and F. R. DE BOER, 1980, Physica **B100**, 1.
MORIARTY, J. A., 1982, Phys. Rev. **B26**, 1754.
MORIARTY, J. A., 1983, Int. J. Quantum Chem. **17**, 541.
MORIARTY, J. A., 1988, Phys. Lett. **131**, 41.
MORIARTY, J. A., and A. K. MCMAHAN, 1982, Phys. Rev. Lett. **48**, 809.
MORIYA, T., 1965, Prog. Theor. Phys. **33**, 157.
MORUZZI, V. L., J. F. JANAK and A. R. WILLIAMS, 1978, Calculated Electronic Properties of Metals (Pergamon, New York).
MOTT, N. F., 1949, Proc. Phys. Soc. **A62**, 416.
MOTT, N. F., and H. JONES, 1936, Properties of Metals and Alloys (Dover, New York) ch. 7.
MUELLER, F. M., 1967, Phys. Rev. **153**, 659.
NIEMINEN, R. M., and C. H. HODGES, 1976, J. Phys. **F6**, 573.
NØRSKOV, J. K., 1982, Phys. Rev. **B26**, 2875.
NØRSKOV, J. K., and N. D. LANG, 1980, Phys. Rev. **B21**, 2131.
NØRSKOV, J. K., F. BESENBACHER, J. BOTTIGER, B. B. NIELSEN and A. A. PISAREV, 1982, Phys. Rev. Lett. **49**, 1420.
OHTA, Y., and D. G. PETTIFOR, 1989, J. Phys.: Condens. Matter **2**, 8189.
PAPON, A. M., J. P. SIMON, P. GUYOT and M. C DESJONQUERES 1979, Phil. Mag. **39**, 301.
PAULING, L., 1960, The Nature of the Chemical Bond (Cornell Univ. Press, New York).
PAXTON, A. T., M. METHFESSEL and H. M. POLATOGLOU, 1990, Phys. Rev. **B41**, 8127.
PAXTON, A. T., and D. G. PETTIFOR, 1992, Scripta Metall. **26**, 529.
PENN, D. R., 1966, Phys. Rev. **142**, 350.
PETTIFOR, D. G., 1970a, Phys. Rev. **B2**, 3031.
PETTIFOR, D. G., 1970b, J. Phys. **C3**, 367.
PETTIFOR, D. G., 1972a, J. Phys. **C5**, 97.
PETTIFOR, D. G., 1972b, in: Metallurgical Chemistry, ed. O. Kubaschewski (Her Majesty's Stationery Office, London) p. 191.
PETTIFOR, D. G., 1976, Commun. Phys. **1**, 141.
PETTIFOR, D. G., 1977, J. Phys. **F7**, 613.
PETTIFOR, D. G., 1978a, J. Chem. Phys. **69**, 2930.
PETTIFOR, D. G., 1978b, J. Phys. **F8**, 219.
PETTIFOR, D. G., 1979, Phys. Rev. Lett. **42**, 846.
PETTIFOR, D. G., 1980, J. Magn. Magn. Mater. **15-18**, 847.
PETTIFOR, D. G., 1982, Phys. Scripta **T1**, 26.
PETTIFOR, D. G., 1984, Solid State Commun. **51**, 31.
*PETTIFOR, D. G., 1987, Solid State Physics **40**, 43.
PETTIFOR, D. G., 1988a, Mater. Sci. Technol. **4**, 2480.
PETTIFOR, D. G., 1988b, Physica B **149**, 3.
*PETTIFOR, D. G., 1992, in: Electron Theory in Alloy Design, eds. D. G. Pettifor and A. H. Cottrell (Institute of Materials, London) ch. 4.
PETTIFOR, D. G., and C. D. GELATT, 1983, fig. 8 of Cohesion and Decohesion in the Metallic Bond, in: Atomistics of Fracture, Proc. Nato Adv. Res. Inst., Corsica, 1981, ed. R. Latanision (Plenum, New York).
PETTIFOR, D. G., and R. PODLOUCKY, 1984, Phys. Rev. Lett. **53**, 1080.
PETTIFOR, D. G., and R. PODLOUCKY, 1986, J. Phys. **C19**, 315.
PETTIFOR, D. G., and M. A. WARD, 1984, Solid State Commun. **49**, 291.

PHILLIPS, J. C., 1970, Rev. Mod. Phys. **42**, 317.
PUSKA, M. J., R. M. NIEMINEN and M. MANNINEN, 1981, Phys. Rev. **B24**, 3037.
RATH, J., and J. CALLAWAY, 1973, Phys. Rev. **B8**, 5398.
RUEDENBERG, K., 1962, Rev. Mod. Phys. **34**, 326.
ST. JOHN, J., and A. N. BLOCH, 1974, Phys. Rev. Lett. **33**, 1095.
SATO, H., and R. S. TOTH, 1961, Phys. Rev. **124**, 1833.
SCHIFF, L. I., 1968, Quantum Mechanics, 3rd Ed. (McGraw-Hill, New York).
SHIGA, M., and Y. NAKAMURA, 1969, J. Phys. Soc. Japan **26**, 24.
SKRIVER, H. L., 1981a, J. Phys. **F11**, 97.
SKRIVER, H. L., 1981b, in: Physics of Solids under High Pressure, eds. J. S. Schilling and R. N. Shelton (North-Holland, Amsterdam) p. 279.
SKRIVER, H. L., 1982, Phys. Rev. Lett. **49**, 1768.
SKRIVER, H. L., O. K. ANDERSEN and B. JOHANNSSON, 1978, Phys. Rev. Lett. **41**, 42.
SLATER, J. C., 1951a, Phys. Rev. **82**, 538.
SLATER, J. C., 1951b, Phys. Rev. **81**, 385.
SLATER, J. C., 1963, Quantum Theory of Molecules and Solids, vol. I (McGraw-Hill, Maidenhead).
SLATER, J. C., and G. F. KOSTER, 1954, Phys. Rev. **94**, 1498.
SLUITER, M., D. DE FONTAINE, X. Q. GUO, R. PODLOUCKY and A. J. FREEMAN, 1990, Phys. Rev. **B42**, 10460.
STONER, E. C., 1939, Proc. Roy. Soc. **A169**, 339.
STOTT, M. J., and E. ZAREMBA, 1980, Phys. Rev. **B22**, 1564.
STROUD, D., and N. W. ASHCROFT, 1971, J. Phys. **F1**, 113.
*SUTTON, A. P., 1993, Electronic Structure of Materials (Clarendon Press, Oxford).
TAKEMURA, K., S. MINOMURA and O. SHIMOMURA, 1982, Phys. Rev. Lett. **49**, 1772.
TAYLOR, R., and A. H. MACDONALD, 1980, J. Phys. **F10**, 2387.
TINKHAM, M., 1964, Group Theory and Quantum Mechanics (McGraw-Hill, New York).
VAN SCHILFGAARDE, M., A. T. PAXTON, A. PASTUREL and M. METHFESSEL, 1990, Mat. Res. Soc. Symp. Proc. **186**, 107.
VANDERBILT, D., 1990, Phys. Rev. **B41**, 7892.
VILLARS, P., and L. D. CALVERT, 1985, Pearson's Handbook of Crystallographic Data for Intermetallic Phases, vols. 1, 2, 3 (American Society for Metals, Metals Park, Ohio).
WATSON,. R. E., and L. H. BENNETT, 1981, Calphad **5**, 25.
WATSON, R. E., H. EHRENREICH and L. HODGES, 1970, Phys. Rev. Lett. **24**, 829.
WIGNER, E. P., and F. SEITZ, 1933, Phys. Rev. **43**, 804.
WILLIAMS, A. R., C. D. GELATT and V. L. MORUZZI, 1980a, in: Proc. Metallurg. Soc. AIME, New Orleans 1979, ed. L. H. Bennett (Met. Soc. AIME, Warrendale, PA).
WILLIAMS, A. R., C. D. GELATT and V. L. MORUZZI, 1980b, Phys. Rev. Lett. **44**, 429.
WILLIAMS, A. R., C. D. GELATT and V. L. MORUZZI, 1982, Phys. Rev. **B25**, 6509.
WINDSOR, C. G., 1972, J. Phys. **F2**, 742.
WOHLFARTH, E. P., 1980, in: Ferromagnetic Materials, vol. 1, ed. E. P. Wohlfarth (North-Holland, Amsterdam) ch. 1.
WOOD, J. H., 1962, Phys. Rev. **126**, 517.
YIN, M. T., 1982, Ph. D. thesis, Univ. of California, Berkeley, figs. 5 and 6.
YIN, M. T., and M. L. COHEN, 1980, Phys. Rev. Lett. **45**, 1004.
YIN, M. T., and M. L. COHEN, 1981, Solid State Commun. **38**, 625.
ZUNGER, A., 1980, Phys. Rev. **B22**, 5839.
ZUNGER, A., 1994, in: Statics and Dynamics of Alloy Phase Transformations, eds. P. E. A. Turchi and A. Oonis (Plenum, New York), 361.

Further reading

References marked with an asterisk in the list above can also be used for general reading.

CHAPTER 3

STRUCTURE AND STABILITY OF ALLOYS*

T.B. MASSALSKI

Department of Materials Science
and Engineering
Carnegie–Mellon University
Pittsburgh, PA, USA

* This chapter is dedicated to the memory of my good friend Professor Peter Haasen. Much of the revision which I undertook was done in Göttingen, in the summer of 1993, and many suggestions for changes and improvements came from Peter during our walks in Göttingen woods. I am very grateful to the Alexander von Humboldt Foundation for the award of the Humboldt Prize which made my stay in Göttingen during that summer possible.

R. W. Cahn and P. Haasen†, eds.
Physical Metallurgy; fourth, revised and enhanced edition

1. Solid solubility

A *solid solution* is obtained when atoms of different elements are able to share together, and with changing proportions, various sites of a common crystalline lattice. It is now generally recognized that all metals and compounds show some solubility in the solid state; a question of great interest is, however, the extent of solid solubility in a given case. For example, only 0.2 wt% of phosphorus can be dissolved in γ-iron, but nearly 39 wt% of zinc can be dissolved in copper without changing its structure. On alloying copper with nickel, on the other hand, the same fcc structure is maintained throughout the entire alloy system (fig. 1a), providing an example of *complete solid solubility*. The Au–Cu alloys have complete solid solubility at high temperatures, but show different behavior at low temperatures (see fig. 1b and § 11). In the great multitude of phase diagrams now known, the above cases, and even the case of only a partial but extensive solid solubility (of several atomic percent), are relatively rare. Complete solid solubility can occur only if the structures of the elements involved are basically the same, but it need not always occur when this condition is fulfilled (i.e., the system Cu–Ag which is a simple eutectic). In the case of close-packed hexagonal solid solutions

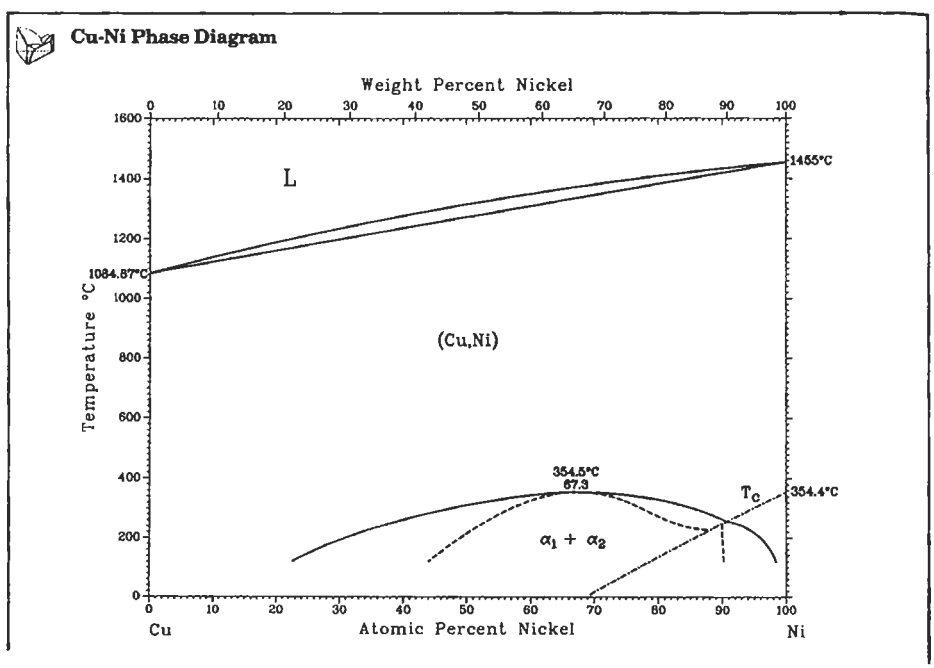

Fig. 1a. Complete solid solubility in the system Cu–Ni which maintains fcc structure throughout the whole composition range (from MASSALSKI [1990].)

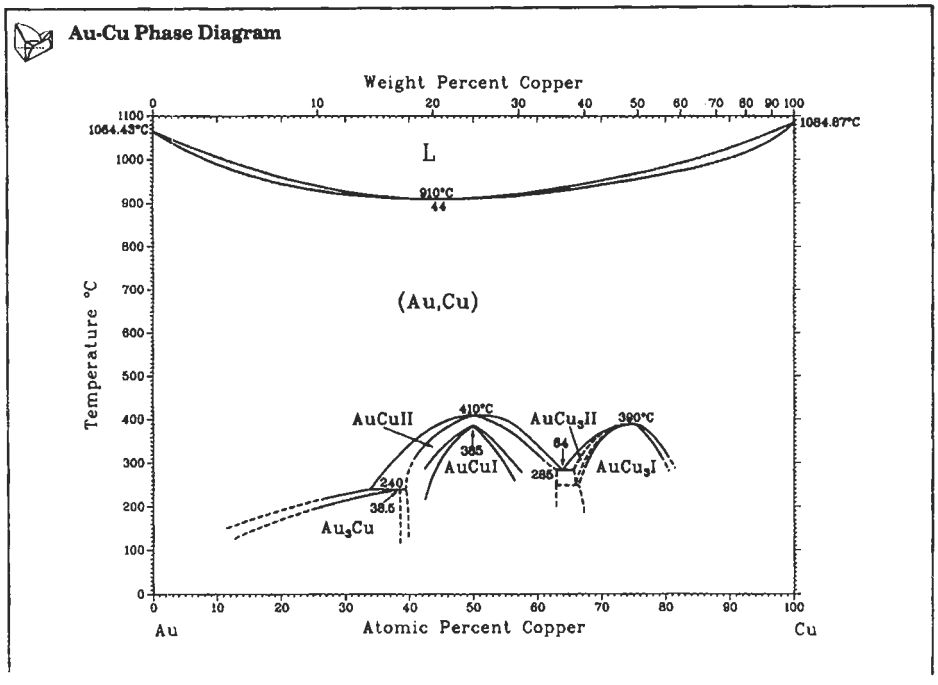

Fig. 1b. The Au–Cu system has complete solid solubility and fcc structure at high temperatures. At low temperatures superlattices form (see § 11). (From MASSALSKI [1990].)

considerable difference between the values of the axial ratio can usually be accommodated on changing from one element to another; for example, the axial ratio, c/a, changes from 1.5873 for Ti to 1.5931 for Zr in the Ti–Zr system, and from 1.6235 for Mg to 1.8856 for Cd in the Mg–Cd system. The phase diagrams of these systems are shown in figs. 1c and 1d. In the case of Ti–Zr the pure elements exist in two allotropic forms (cubic at high temperatures and hexagonal at low temperatures), and complete solid solubility occurs between both modifications on alloying. In the Mg–Cd system, on the other hand, complete solubility occurs only at high temperatures and is interrupted at lower temperatures by the formation of superlattices (see § 11).

From the point of view of solid solubility, chemical compounds can be compared with pure metals and may be said to show alloying behavior if they exhibit wide solid solubility in a phase diagram. Since compounds are usually formed at fixed ratios of the numbers of atoms, the occurrence of solid solubility represents a departure from stoichiometry. If a compound is truly ionic in nature, the extent of such departure may be extremely small, amounting perhaps to a fraction of an at%; and for all practical purposes this is usually ignored and the compound is then drawn as a vertical line in the phase diagram. However, in typical metallic systems a large number of phases have been

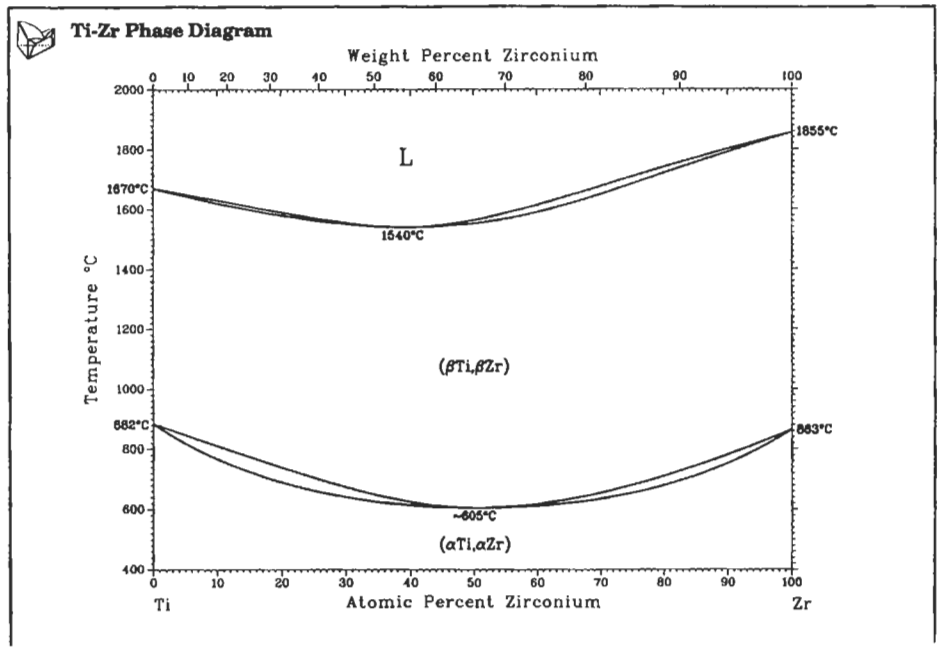

Fig. 1c. The Ti–Zr system has complete solid solubility, with cubic structure at high temperatures and hexagonal structure at low temperatures (from MASSALSKI [1990].)

observed at atomic compositions which bear no apparent relation to the rules of stoichiometry. Such phases frequently possess wide ranges of solid solubility and resemble the solid solutions obtained on initial alloying of pure metals. To an engineer concerned with materials the occurrence of wide solid solubility, both between pure metals and in compounds, is of great practical interest because it is often associated with relatively simple metallic structures which possess desirable mechanical and physical properties.

In this chapter we shall examine some of the factors which determine the limits of solid solubility in metallic systems and then consider some properties of the structure of extended solid solutions, such as lattice spacings, defects, departure from randomness, size effects, etc.

2. *Terminology (types of solid solutions)*

Solid solutions are phases of variable composition, and in principle any number of components can be alloyed together to form a series of solid solutions. However, for simplicity we shall consider mainly the binary alloys. The replacement of copper atoms by nickel on the lattice of pure copper is an example of a *substitutional* solid solution.

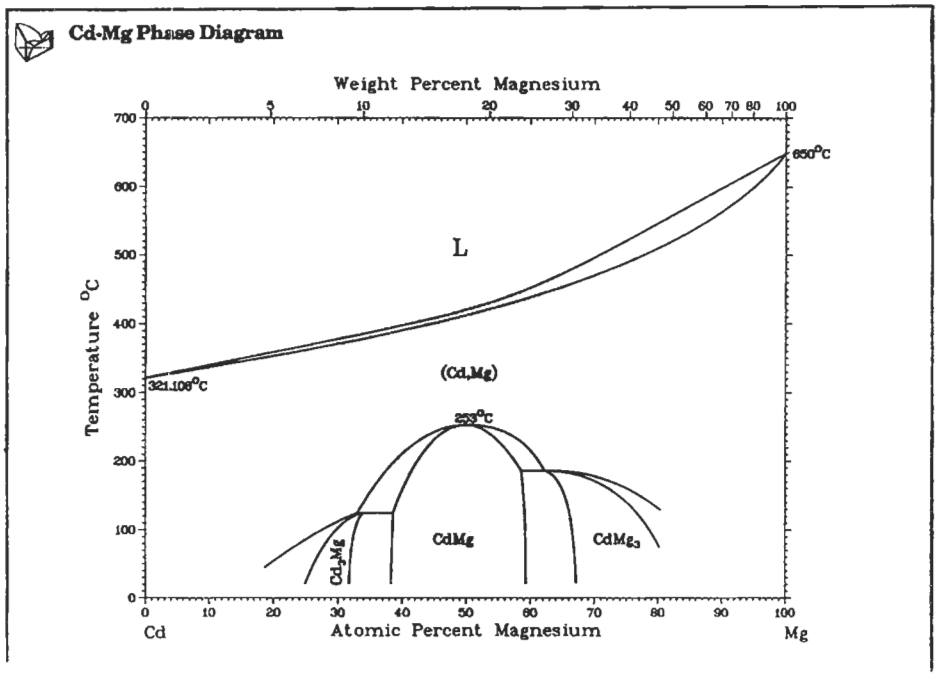

Fig. 1d. In the Mg–Cd system complete solid solubility occurs at high temperatures. Superlattices form at low temperatures (see § 11). (From MASSALSKI [1990].)

Since the two elements can be substituted at all proportions throughout the whole system, they form a *continuous series of solid solutions.* If the solid solubility is limited to only those portions of the phase diagram which are linked to pure elements, the resulting phases are known as *primary (or terminal) solid solutions.* Such solutions have, of course, the same structure as the elements on which they are based. All other phases are usually known as *intermediate phases;* they may be called *intermetallic compounds* or *valence compounds* if their solid solubility is unusually restricted around a stoichiometric composition. Intermediate phases typically possess structures which are different from the structure of either of the component elements.

If the size-difference between the component atoms which participate in forming a solid solution is sufficiently large, it may become possible on alloying for the one kind of atoms to be merely deposited in the holes (or interstices) between the other atoms on their space lattice. An *interstitial* solid solution is then formed. Such solutions can occur for example when nonmetallic elements such as boron, oxygen, nitrogen or carbon are dissolved in a metal lattice.

Both interstitial and substitutional solid solutions can be *random,* with statistical distribution of atoms, or they may be partially or completely *ordered,* in which case the unlike atoms show preference for one another. A fully ordered solid solution is some-

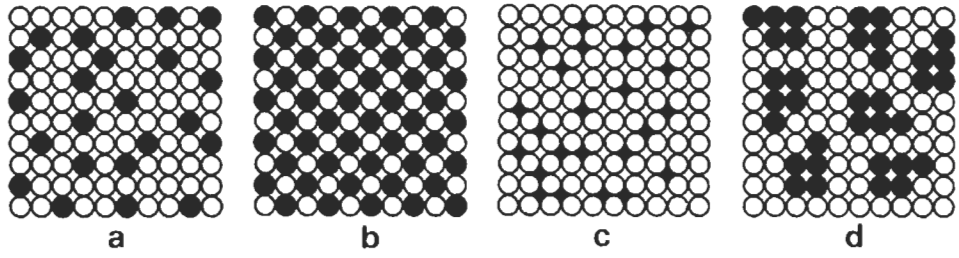

Fig. 2. Schematic models of solid solutions: (a) substitutional random; (b) substitutional ordered; (c) interstitial random; (d) solute clusters in solid solution.

times known as a *superlattice*. Alternatively, the like-atoms may tend to associate together to form clusters within the solid solution. Again, the clusters may be dispersed randomly or they may be ordered or oriented in various ways, producing a variety of complex substructures within the solid solution. A diagrammatical illustration of the various types of solid solution is given in fig. 2.

While it is possible to consider the case of a random solid solution as an idealized example, the mounting experimental evidence, based mainly on diffuse X-ray scattering, suggests that complete randomness (like perfect crystallinity) is probably never found in nature. Hence, solid solutions which are in a thermodynamical equilibrium (ch. 5) may be considered to be truly *homogeneous* on a macroscopic scale, but they need not be homogeneous down to the scale where atoms are considered individually.

3. *Energy of solid solutions and phase stability considerations*

The extent of solid solubility of phases, the stability of phases, the temperature dependence of stability, and the choice of structures that are actually observed in phase diagrams are the result of competition among numerous possible structures that could be stable in a given system. This competition is based on the respective values of the *Gibbs Free Energy* of each competing phase and the variation of this energy with temperature, pressure, composition and possibly other extensive parameters. The details are presented in chapter 5. Here, we shall merely state that the most general form of the Gibbs energy (G) can be expressed as a function of the intensive parameters, enthalpy (H) and entropy (S), and the absolute temperature (T):

$$G = H - TS. \tag{1}$$

As is well known, numerous factors contribute to the H and S parameters. The major contribution to the entropy is from statistical mixing of atoms (ΔS_{mix}), but there can be additional contributions from vibrational effects (ΔS_{vib}), distribution of magnetic moments, clustering of atoms and various long range configurational effects. The main interest in this chapter is in the contributions to the enthalpy resulting from atomic mixing (ΔH_{mix}), which are in turn related to the interaction energies between neighbouring and further distant atoms in a given structure based upon electronic, elastic, magnetic and vibrational effects. Much progress has been made in measuring, calculating and

predicting many such effects, and hence progress continues to be made in the evaluation of the related thermodynamic quantities and ultimately the phase diagrams.
Some recent reviews of these topics are listed in the bibliography for further reading (and in chapter 6).

Typical values of the enthalpy of formation (ΔH) and its relation to the type of bonding are given as an illustration in table 1. As discussed in chapter 6, a change by 10–20 kJ/mole in the interaction parameter that determines the enthalpy of formation can profoundly affect the form of the resulting phase diagram. The estimation of the ΔH values, particularly for systems where the experimental data are meager or lacking, has been therefore of great practical interest to the workers in the area of phase stability. Semi-empirical values of the heats of formation have been predicted for many systems by Miedema and co-workers (MIEDEMA and NIESSEN [1988]) and have found many uses.

Along with the progress achieved in the measurements that established the details of phase diagrams and the associated phases, it is natural that the observed phase stabilities should be tested against basic theory. In this connection, two aspects stand out sharply ([MASSALSKI 1989]):

(1) The need to calculate phase stability from "first principles" in order to understand the basic parameters that control the energy of a phase.

Table 1
Heats of formation at 298K of some typical intermediate phases and compounds.*

Compound or phase	Structure**	Predominant bonding	Heat of formation $-\Delta H$ (kJ/g atom)
MgSe	NaCl (B2)	Ionic	135.9 ± 8.3
MgTe	ZnS (B4)	Ionic	104.3 ± 10.4
ZnTe	ZnS (B3)	Ionic	60.0 ± 2.1
Mg_2Ge	CaF_2 (C1)	Partially ionic	38.4 ± 0.08
Mg_3Bi_2	Ca_2O_3 (D5c)	Partially ionic	30.9 ± 0.8
Mg_2Si	CaF_2 (C1)	Partially ionic	26.3 ± 1.3
InAs	ZnS (B3)	Covalent	30.9 ± 2.5
GaSb	ZnS (B3)	Covalent	20.9 ± 0.8
InSb	ZnS (B3)	Covalent	14.6 ± 0.4
NiTe	NiAs (B8)	Partially metallic	18.8 ± 6.3
CoSn	NiAs (B8)	Partially metallic	15.0 ± 1.3
Co_3Sn_2	NiAs (B8)	Partially metallic	11.3 ± 0.8
$CaMg_2$	$MgZn_2$ (C14)	Metallic	13.3 ± 0.4
Ag_5Zn_8 (0.61 Zn)	γ-brass (D8c)	Metallic	4.6 ± 0.21
AgZn (0.50 Zn)	β-brass (B2)	Metallic	3.1 ± 0.21

*Data taken from ROBINSON and BEVER [1967].

**For meaning of the symbols, see ch. 4.

References: p. 199.

(2) The need to utilize the successful theories of phase stability for predicting phase diagrams in systems where measurements have not yet been done, or are particularly difficult. Here, progress will ultimately permit technologically relevant complex or multicomponent phase diagrams to be predicted.

It was Hume–Rothery and his associates who more than a half century ago laid the foundations for a systematic study of phase diagrams and their interpretation. A suitable testing ground at that time was the stability of alloy phases based on the so-called noble metals, Cu, Ag, and Au (HUME–ROTHERY [1955]; HUME–ROTHERY *et al.* [1969]). From this work has emerged the emphasis on three general metallurgical parameters. Stated very broadly they are:

(1) the difference in atomic sizes of the components,
(2) the electrochemical differences among the components, and
(3) the "electron concentration" change on alloying.

Their importance is often expressed in terms of the so called "Hume–Rothery Rules" (see section 4).

Regarding the basic theory, the understanding and prediction of phase stability of alloys and compounds in terms of the electronic structure calculations is a subject of paramount importance in materials science. There has been much progress in the "first principles" (or the so called "*ab initio*" approach to the band theory of both ordered compounds and, more recently, also of random metallic alloys (STOCKS and WINTER [1984]). At the same time, because of the pressing need of technology, many semi-empirical or partially qualitative schemes of phase stability have been pursued, often very successfully. The results of such attempts are usually the estimated heats of formation (ΔH) (see also ch. 2, § 6.2.).

Basic theoretical guidelines are needed to classify phase diagrams, in order to be able to extrapolate from known binaries to higher order systems. A theoretical derivation of energies of specific structures and phase equilibria between them, eventually will yield reasonably accurate free energy and entropy changes, and a description of states of partial order, relative stability of metastable phases, etc. Clearly, the first step towards true theoretical determination of phase diagrams is to calculate the energies of phases involved in simple binaries and compare them with experimentally determined values, where possible. A number of theoreticians in excellent reviews (LOMER [1967], FAULKNER [1982]; HAFNER [1983]) have outlined the different operations that must be performed to calculate a composition-temperature phase diagram of a binary alloy, starting first with the stability of individual phases. Essentially, these steps are as those enumerated in table 2.

From the point of view of phase stability, the result of such a detailed calculation would be a sufficiently precise set of values of the enthalpies of the various competing alloy phases and their variations with composition. The calculation of the phase diagrams, including temperature and entropy, would be the next step. Clearly, from the point of view of phase stability, even these initial calculations represent a monumental task. Yet, a glance at table 3 quickly shows that theoretical assessments are our only reasonable hope of dealing with higher-order systems in the near future. In table 4, a brief

Table 2
Phase stability calculations.*

(First principles) *General procedure*	
(1)	Calculate self-consistent atomic potentials of components.
(2)	Fix alloy composition.
(3)	Assume a possible crystal structure.
(4)	Choose lattice parameters.
(5)	Introduce the atomic potentials on the lattice, calculate self-consistent band structure and ground state energy, and add interionic energy.
Result: total energy	
(6)	Repeat (4) and (5) for different values of lattice constants.
(7)	Repeat (3) through (6) for other possible crystal structures.
(8)	Repeat (2) through (7) for other compositions.
Result: enthalpy of the possible alloy phases as a function of composition.	

*LOMER [1967], FAULKNER [1982], HAFNER [1983]

summary is given of some of the more recent theoretical calculations that have been developed. This summary is not intended to be comprehensive or complete. (See also ch. 5, § 6.).

Table 3
Possible number of systems.

	$\frac{n!}{(m!(n-m)!}$
binary	$\frac{90!}{2!88!} = 4{,}005$
ternary	$\frac{90!}{3!87!} = 117{,}480$
quaternary	$\frac{90!}{4!86!} = 2{,}555{,}190$

n = number of elements (say 90)
m = number of elements in a system

As emphasized by many authors (MASSALSKI [1989]), the majority of existing models, from the semi-empirical to those providing detailed density maps and electronic parameters of alloys, have the same major drawback as far as phase diagrams are concerned: it is difficult to treat theoretically the temperature dependence of the energy. For example, the calculations that predict enthalpies at 0 K (for first principles calculations), or at some undefined temperature (for the semiempirical models), rarely provide sufficient information about the thermal behavior of such enthalpies or the thermal

entropy contributions. Yet, for the purpose of phase diagrams determination the Gibbs free energies must be calculated by adding to each enthalpy derived from the static models the vibrational energy and the thermal entropy contributions. The latter in turn consist of vibrational and configurational parts. It is clear that the prediction of entropies, particularly for possible metastable phases in phase diagrams, will become the necessary step before the full potential of the theoretically calculated stabilities can be utilized. Only a few interesting examples of phase stability, compound stability and alloying effects are reviewed below.

4. *Factors governing solid solubility (Hume–Rothery rules for primary solid solutions)*

Since all interactions between atoms are a function of electronic forces, they should ultimately be subject to the laws of quantum mechanics. At the present time, however, the available theories of the solid state of the type summarized in table 4 are unable to incorporate or to account for the many factors which have been known to materials scientists as important in determining the structure and various properties of solid solutions. Such factors, for example, as chemical affinity or the size-difference between atoms can be considered only semi-empirically, and even the electronic structure, for which more elaborate theories exist, has been discussed satisfactorily only in a few rather simple cases. Nevertheless, mainly as a result of studies by Hume–Rothery and his associates (HUME–ROTHERY [1961a] and HUME–ROTHERY *et al.* [1969]), extending over more than thirty years, certain general rules have been formulated concerning the limits of primary solid solubility and, to some measure, also the width and stability of certain intermediate phases. As already mentioned above, these rules refer to the difference between the relative atomic radii of the participating elements, their electrochemical differences and their relative valencies. *Hume–Rothery rules* may be summarized as follows:

(i) If the difference between the atomic sizes of the component elements forming an alloy exceeds about 14–15%, solid solubility should become restricted. This is known as the 15% *rule*. The general concept may be illustrated by reference to fig. 3 (HUME–ROTHERY [1961a]) in which the ranges of favorable atomic sizes with respect to copper, silver and γ-iron are shown diagrammatically. If the atomic diameter of a particular solute element lies outside the favorable size zone for the solvent, the *size factor* is said to be unfavourable and the primary solid solubility will be restricted usually in some proportion to the increasing difference between the two atomic diameters. Within the favorable zone the size factor is only of secondary importance and other factors will determine the total extent of solid solubility. In a sense, therefore, the 15% rule is a negative rule stressing the role of size differences only when they *restrict* alloy formation. In this connection, WABER *et al.* [1963] have shown that when the size rule alone was applied to 1423 terminal solid solutions, in 90.3% of the systems where little solid solubility was predicted, little solid solubility was in fact observed, but the prediction of extensive solid solubility on the basis of small size difference was only 50% successful. Theoretical justification for the 15% rule has been obtained from considerations of elastic strain energy in a solid solution (see below).